

# High power ultraviolet LED illumination systems: coherence properties and applications in photolithography

THÈSE N° 8977 (2018)

PRÉSENTÉE LE 26 OCTOBRE 2018

À LA FACULTÉ DES SCIENCES ET TECHNIQUES DE L'INGÉNIEUR  
LABORATOIRE D'OPTIQUE APPLIQUÉE  
PROGRAMME DOCTORAL EN PHOTONIQUE

ÉCOLE POLYTECHNIQUE FÉDÉRALE DE LAUSANNE

POUR L'OBTENTION DU GRADE DE DOCTEUR ÈS SCIENCES

PAR

Johana BERNASCONI

acceptée sur proposition du jury:

Prof. N. Grandjean, président du jury  
Prof. H. P. Herzig, Dr T. Scharf, directeurs de thèse  
Prof. U. D. Zeitner, rapporteur  
Dr W. Noell, rapporteur  
Prof. T. Lasser, rapporteur



ÉCOLE POLYTECHNIQUE  
FÉDÉRALE DE LAUSANNE

Suisse  
2018



Nous ne pouvons pas tous résoudre la question de l'univers,  
pour y parvenir, certains d'entre nous  
doivent réparer des pompes.  
— Jacques Farine



## Remerciements

Si j'ai pu entreprendre cette thèse, c'est grâce à Hans Peter Herzig et Toralf Scharf, qui ont décidé de m'engager pour un projet en collaboration avec une entreprise. Merci donc à eux de m'avoir donné cette possibilité. Dans l'entreprise avec laquelle je collaborais, j'ai particulièrement apprécié les conseils de Uwe Vogler, au début du projet, puis de Raoul Kirner et Wilfried Noell, en deuxième partie.

J'ai par ailleurs eu la chance d'atterrir dans un groupe constitué de personnes remarquables qui ont rendu la durée de ma thèse plus agréable. Je tiens à remercier particulièrement Irène Philipoussis et Marcel Groccia, qui m'ont apporté un soutien technique de qualité et nécessaire à la réussite de ma thèse. La super secrétaire du groupe, Brigitte Khan, était également toujours là pour répondre à mes questions administratives (et pour organiser les cafés OPT en pensant au chocolat noir). Même si je travaillais en générale seule sur mon projet, j'ai pu profiter des conseils éclairés de mes collègues: de Gaël Oslowiecky (qui a toujours une solution, même si ça implique de tout démonter) et de Gregoire Smolik (qui m'a démontré que c'est possible d'être plus nonchalant que moi). Merci également à Raphaël Barbey pour l'humour (suspect) et le dicing de fentes. J'ai également pu apprécier les conseils culinaires de notre italienne préférée, Sara Santi (pour savoir quel type de pâte va avec quelle sauce). J'ai profité de l'enthousiasme sportif de Daniel Infante pour la course à pied et la grimpe. J'ai eu du plaisir à échanger sur des sujets variés et ouvert mes horizons culturels avec mes collègues de bureau, Richa Dubey, Krishnaparvathy Puthankovilakam.

Pour finir, je ne serais pas venue à bout de ce travail sans le soutien de mes amis (des becs) et ma famille. Un grand merci à Nicolas, qui m'a convaincue de finir ma thèse dans les nombreux moments de doute (et que je pourrais toujours aller garder des moutons dans les Alpes après). J'ai la chance d'avoir grandi dans une famille super: mes frères Hugues et Lorain sont toujours là pour me me changer les idées (en m'envoyant des photos d'animaux morts et en venant installer des lampes), ma grand-mère Jeanne-Marie pour me poser des questions d'ingénierie compliquées et mon grand-père André pour m'envoyer des photos de ses voyages. J'ai également été éduquée par des parents qui n'ont jamais doutés de mes capacités à réussir ce que j'entreprends. Merci Anne-Claude et Henri pour votre confiance (même si des fois, ça met un peu la pression).

*Neuchâtel, Octobre 2018*

J. B.



# Abstract

Mask-aligner photolithography is a technology used to replicate patterns from a mask to a photosensitive substrate. It is widely used in the fabrication of MEMS and micro-optical components, and for other applications with critical dimensions in the micrometer range. Traditionally, the light sources used for mask-aligners are high-pressure mercury arc lamps, which emit in the ultraviolet range with peaks at 365 nm, 405 nm and 435 nm, the so-called g-, h- and i- lines, respectively. These lamps suffer from several disadvantages, such as a low efficiency, bulkiness, a short lifetime, and the toxicity of mercury. Finding an alternative to mercury arc lamps would therefore be highly beneficial. In addition, specific techniques in mask-aligner technologies like Talbot lithography, multiple exposures, mask-source optimization or optical proximity correction lithography require high power sources with an increased control over the angular distribution and the spatial coherence. This is currently not easily done with a mercury arc lamp illumination. In this regard, a method to efficiently measure the angular distribution and the spatial coherence in the mask-plane would be of great interest. In recent years, high power ultraviolet LEDs at the same wavelengths have appeared on the market. LEDs possess a smaller Etendue, they can be electronically driven at high frequencies and they have a superior lifetime. This makes them ideal candidates to overcome the limitations of the mercury arc lamp illumination systems.

The work focuses on the development and study of a novel LED-based illumination system for mask aligner lithography. This illumination system consists in an array of 7x7 LEDs, with individual reflectors. They form a modular 250 W source which can advantageously replace a 1 kW mercury arc lamp. The light is collected by the reflectors and brought onto a fly's eye integrator with two subsequent lenses which shape and homogenize the light field. Different patterns can be created by the source, determining the angles and the spatial coherence in the mask plane. The first part of the work presents the design and a complete set of characterizations of the final prototype. The achieved irradiance uniformity in the mask-plane of a MA/BA8 Gen3 SUSS MicroTec mask-aligner is within  $\pm 1.2 - 2\%$ . Prints tests in proximity printing, with a gap of 30  $\mu\text{m}$  demonstrate a resolution of 3.5  $\mu\text{m}$ .

In the second part of the thesis, the development of a method to measure the spatial coherence, which is based on a double slit approach and backed up by simulation, is described. The link between the spatial coherence length and the angular extent of a circular source is made. The measurements show a good agreement with the analytical expression. A compact system is described, which enables the measurement of the spatial coherence in the mask plane, where only little space is available. An original method is put into practice in order to measure the

## Abstract

---

directional spatial coherence in two dimensions in the mask plane of a mask-aligner. This is achieved by using a circular double slits system. Prints are also made which illustrate the importance of the angular distribution and the spatial coherence.

This novel LED-based illumination system is almost readily implementable in current, commercial, mask-aligners. It enables greater efficiency, more functionalities and a longer lifetime compared to standard mercury arc lamp illumination systems. In particular, the spatial coherence properties of the source can be precisely managed and monitored thanks to the directional spatial coherence measurement.

**Keywords:** illumination design, concentrator, nonimaging optics, lithography, mask-aligner, spatial coherence.



## Résumé

La photolithographie par aligneuse de masques est une technique de production utilisée pour reproduire des structures d'un masque à un substrat photosensible. Cette technique est utilisée pour la fabrication de MEMS, de composants optiques et pour d'autres applications avec des structures de taille micrométrique. Traditionnellement, les sources lumineuses utilisées pour ce type d'applications sont des lampes à mercure à haute pression. Elles émettent de la lumière dans les longueurs d'ondes ultraviolettes, avec des pics à 365 nm, 405 nm, and 435 nm, lesquelles sont appelées ligne g, h et i. Ces lampes souffrent de sévères inconvénients tels qu'une faible efficacité, un fort encombrement, une courte durée de vie et la toxicité du mercure. Trouver une alternative aux lampes à mercure serait très bénéfique. D'autre part, des techniques spécifiques effectuées avec les aligneuses, comme la lithographie de Talbot, l'exposition multiple, l'optimisation source-masque ou encore la lithographie de correction de proximité optique, nécessitent des sources lumineuses puissantes qui permettent un contrôle accru sur la distribution angulaire et la cohérence spatiale dans le plan du masque. Ceci est difficile à effectuer avec les systèmes actuels basés sur les lampes à mercure. Ces dernières années, des LEDs avec des longueurs d'ondes dans l'ultraviolet sont apparues sur le marché. Les LEDs possèdent une étendue plus petite, peuvent être contrôlées électroniquement à haute fréquence, et ont une durée de vie supérieure. Ce sont des candidates idéales pour dépasser les limitations actuelles des systèmes d'illumination basés sur les lampes à mercure. Ce travail, se concentre sur le développement d'un nouveau système d'illumination pour aligneuse de masques, basé sur des LEDs. Ce système d'illumination comprend une matrice de 7x7 LEDs sur lesquelles sont montés des réflecteurs individuels. Ces LEDs forment une source modulaire de 250 W, qui peut remplacer une lampe à mercure de 1 kW. La lumière est collectée par les réflecteurs puis est dirigée sur un intégrateur de Koehler et deux lentilles subséquentes, qui homogénéisent le champ lumineux. Différents motifs d'illumination peuvent être créés avec cette source, définissant les angles et la cohérence spatiale dans le plan du masque. La première partie du travail présente le design et la caractérisation du prototype final. Les mesures d'uniformité de l'irradiance dans le plan du masque d'une aligneuse MA/BA8 Gen3 SUSS donnent une uniformité à  $\pm 1.2 - 2 \%$ . Des tests d'impression avec 30  $\mu\text{m}$  d'écart de proximité résultent en une résolution d'impression de 3.5  $\mu\text{m}$ .

La deuxième partie du travail présente une méthode qui permet de mesurer la cohérence spatiale, basée sur une méthode de double fentes et appuyée par de la simulation. La relation entre la longueur de cohérence spatiale et l'extension angulaire d'une source circulaire est établie et confirmées par des mesures. Un système compact est décrit, qui permet de mesurer

## Résumé

---

le degré de cohérence spatiale dans le plan du masque. Une méthode originale est développée pour mesurer la cohérence spatiale en deux dimensions. Ceci est réalisé en utilisant un système à double fentes circulaires. Des tests d'impressions sont également présentés, qui illustrent l'importance de la variation de la distribution angulaire et de la cohérence spatiale dans le plan du masque.

Ce nouveau système d'illumination LED peut presque être implémenté directement dans des aligneuses actuelles. Il permet d'obtenir une meilleure efficacité, plus de fonctionnalités et une durée de vie supérieure, comparé aux systèmes d'illumination à lampe à mercure. En particulier, les propriétés de cohérence spatiale de la source peuvent être gérées et monitorées précisément, grâce à la mesure de cohérence spatiale bidirectionnelle.

**Mots-clés :** illumination, cencentrateur, optique, lithographie, aligneuse de masques, cohérence spatiale.

# Contents

|   |              |
|---|--------------|
| <b>Acknowledgements</b>   | <b>v</b>     |
| <b>Abstract (English/Français/Deutsch)</b>                              | <b>vii</b>   |
| <b>List of figures</b>  | <b>xii</b>   |
| <b>List of tables</b>   | <b>xv</b>    |
| <b>Acronyms</b>   | <b>xviii</b> |
| <b>Introduction</b>   | <b>1</b>     |
| <b>1 Illumination for mask-aligner lithography</b>                      | <b>3</b>     |
| 1.1 Motivation . . . . .  | 3            |
| 1.2 Basics of illumination systems . . . . .                            | 4            |
| 1.2.1 Etendue . . . . .   | 4            |
| 1.2.2 Irradiance and intensity . . . . .                                | 4            |
| 1.2.3 Beam shaping and homogenization . . . . .                         | 5            |
| 1.3 Mask-aligners with MO Exposure Optics® . . . . .                    | 6            |
| 1.3.1 Design of illumination systems . . . . .                          | 6            |
| 1.3.2 Summary of the specifications . . . . .                           | 8            |
| 1.4 Towards solid-state sources for mask-aligner illumination . . . . . | 9            |
| 1.4.1 Choosing between laser and LEDs . . . . .                         | 9            |
| 1.4.2 Mask-aligner illumination system with a stack of LEDs . . . . .   | 10           |
| 1.5 Phase space representation of mask-aligner illumination . . . . .   | 12           |
| <b>2 High power UV LED illumination system</b>                          | <b>17</b>    |
| 2.1 Design . . . . .  | 17           |
| 2.1.1 Optical design . . . . .  | 17           |
| 2.1.2 Mechanical design . . . . .                                       | 19           |
| 2.1.3 Simulation and power budget . . . . .                             | 26           |
| 2.1.4 Fabrication tolerances . . . . .                                  | 29           |
| 2.1.5 Electrical and thermal management design . . . . .                | 34           |
| 2.2 Characterization of the performance of the prototype . . . . .      | 37           |
| 2.2.1 Optical characterization . . . . .                                | 37           |

## Contents

---

|          |  |            |
|----------|--|------------|
| 2.2.2    | Power efficiency and stability . . . . .   | 42         |
| 2.2.3    | Angular spectrum and irradiance uniformity in the mask plane . . . . .           | 44         |
| 2.2.4    | Print tests . . . . .  | 47         |
| 2.3      | Summary . . . . .  | 52         |
| 2.4      | Possible improvements and future developments . . . . .                          | 53         |
| <b>3</b> | <b>Spatial coherence in illumination systems</b>                                 | <b>55</b>  |
| 3.1      | Motivation . . . . .   | 55         |
| 3.2      | Basics of light coherence . . . . .  | 56         |
| 3.3      | Methods for measuring the spatial coherence . . . . .                            | 57         |
| 3.4      | Double and multi slits interference . . . . .                                    | 58         |
| 3.5      | Design of a coherence measurement apparatus . . . . .                            | 60         |
| 3.5.1    | Double slits design . . . . .  | 61         |
| 3.5.2    | Multi slits design . . . . .   | 65         |
| 3.6      | Simulating the spatial coherence . . . . .                                       | 66         |
| 3.6.1    | Plane waves superposition method . . . . .                                       | 66         |
| 3.6.2    | Random phase screens superposition method . . . . .                              | 71         |
| 3.6.3    | Comparison of the two models . . . . .   | 76         |
| <b>4</b> | <b>Measurement of the degree of spatial coherence</b>                            | <b>79</b>  |
| 4.1      | The degree of spatial coherence of different light sources . . . . .             | 79         |
| 4.1.1    | Setup . . . . .  | 79         |
| 4.1.2    | Results . . . . .  | 82         |
| 4.2      | The degree of spatial coherence in a mask-aligner . . . . .                      | 87         |
| 4.2.1    | The degree of spatial coherence for different illumination patterns . . . . .    | 87         |
| 4.2.2    | Uniformity of the degree of spatial coherence across the mask plane . . . . .    | 88         |
| 4.2.3    | Variation of the degree of coherence with the orientation of the slits . . . . . | 89         |
| 4.3      | 2D spatial coherence measurement with circular double slits . . . . .            | 91         |
| 4.4      | Print tests with different spatial coherence lengths . . . . .                   | 94         |
| 4.5      | Summary . . . . .  | 96         |
| 4.6      | Possible improvements and future developments . . . . .                          | 97         |
|          | <b>Conclusion</b>  | <b>98</b>  |
|          | <b>Bibliography</b>  | <b>101</b> |
|          | <b>Curriculum Vitae</b>  | <b>105</b> |

# List of Figures

|      |  |    |
|------|--|----|
| 1.1  | A schematic of the optical Etendue. . . . .  | 5  |
| 1.2  | A schematic of a Koehler illumination. . . . .   | 5  |
| 1.3  | A schematic of a fly's eye integrator. . . . .   | 6  |
| 1.4  | A schematic of the MO Exposure Optics®. . . . .  | 7  |
| 1.5  | The illumination filter plates. . . . .  | 7  |
| 1.6  | The speckles and interference patterns that can appear with lasers. . . . .  | 9  |
| 1.7  | A schematic of the mask-aligner illumination with an array of LEDs. . . . .  | 11 |
| 1.8  | A schematic of the phase space transformation in a mask-aligner equipped with MO Exposure optics. . . . .          | 14 |
| 1.9  | A schematic of the phase space transformation in a mask-aligner equipped with an LED illumination system . . . . . | 15 |
|      |  |    |
| 2.1  | A schematic of the parabolic compound concentrator. . . . .  | 18 |
| 2.2  | A FRED simulation of the parabolic compound concentrator. . . . .  | 19 |
| 2.3  | A picture of the rotational symmetric reflector. . . . .   | 20 |
| 2.4  | A picture of the fan forming the reflectors. . . . .   | 21 |
| 2.5  | The mechanical design of the 2x2 squared reflectors. . . . .   | 22 |
| 2.6  | The Solidworks design of the 7x7 LEDs and reflectors system. . . . .   | 23 |
| 2.7  | A picture of the 7x7 LEDs and reflectors system. . . . .   | 24 |
| 2.8  | A schematic of the setup for the measurement of the reflectivity. . . . .  | 24 |
| 2.9  | The graph of the directivity of the LED. . . . .   | 26 |
| 2.10 | A 3D rendering of the FRED simulation of the 2x2 LEDs system. . . . .  | 27 |
| 2.11 | The power budget for the 7x7 LED illumination system. . . . .  | 28 |
| 2.12 | The simulated irradiance for LED displacements. . . . .  | 31 |
| 2.13 | The simulated intensity distribution for displacements of a LED. . . . .   | 32 |
| 2.14 | The collection efficiency as a function LED displacements in the z direction. . . . .                              | 33 |
| 2.15 | A picture of the irradiance at the output of the reflectors. . . . .   | 33 |
| 2.16 | A detail of the SOLIDWORKS model of the corners of the reflectors. . . . .   | 34 |
| 2.17 | The groups of LEDs. . . . .  | 35 |
| 2.18 | A schematic of the electronics of the 7x7 LED system. . . . .  | 36 |
| 2.19 | A photograph of the 7x7 LEDs system. . . . .   | 36 |
| 2.20 | Schematics of the characterization process. . . . .  | 37 |
| 2.21 | The measurement of the linearity of the photodiode. . . . .  | 38 |

## List of Figures

---

|      |  |    |
|------|--|----|
| 2.22 | A photograph of the X-Y scanner . . . . .  | 39 |
| 2.23 | A photograph of the angular scanner . . . . .  | 39 |
| 2.24 | The measurement of the irradiance and intensity distributions after one reflector. . . . .                           | 40 |
| 2.25 | Measurements of the irradiance and intensity after four reflectors. . . . .  | 41 |
| 2.26 | The measurement of the intensity distribution after the four reflectors and the fly's eye integrator. . . . .        | 41 |
| 2.27 | The irradiance stability in the mask plane. . . . .  | 43 |
| 2.28 | A photograph of the 7x7 LEDs and reflector system mounted in the machine. . . . .                                    | 44 |
| 2.29 | A picture of the 7x7 patterns. . . . .   | 45 |
| 2.30 | Pictures of the angular spectrum in the mask plane of the mercury lamp illumination and the 7x7 LED system . . . . . | 46 |
| 2.31 | The irradiance uniformity measurement in the mask plane for the 7x7 LEDs illumination. . . . .                       | 48 |
| 2.32 | A schematic representation of the irradiance uniformity measurement for the different illumination patterns. . . . . | 48 |
| 2.33 | The print test results with the 2x2 LEDs system. . . . .   | 49 |
| 2.34 | The print test results with the 7x7 LEDs. . . . .  | 50 |
| 2.35 | The print test results with the corners. . . . .   | 50 |
| 2.36 | The print test results with the large ring. . . . .  | 51 |
| 2.37 | The print test results with the small ring. . . . .  | 51 |
| 2.38 | The print test results with the center LED. . . . .  | 51 |
|      |  |    |
| 3.1  | Spatial coherence . . . . .  | 56 |
| 3.2  | A schematic of the double slits. . . . .   | 62 |
| 3.3  | A photograph of the double slits. . . . .  | 64 |
| 3.4  | A photograph of the multi slits. . . . .   | 65 |
| 3.5  | A schematic of the plane waves superposition method. . . . .   | 66 |
| 3.6  | The simulation of the interference pattern for 1 $\mu\text{m}$ double slits. . . . .                                 | 69 |
| 3.7  | The contrast vs the angle . . . . .  | 70 |
| 3.8  | A schematic of the multiple screens method. . . . .  | 71 |
| 3.9  | The contrast vs the spatial coherence length . . . . .   | 74 |
| 3.10 | The simulation of the interference pattern for 1 $\mu\text{m}$ multislits. . . . .                                   | 75 |
| 3.11 | The spatial coherence length as a function of the angle. . . . .   | 77 |
|      |  |    |
| 4.1  | The coherence measurement setup . . . . .  | 80 |
| 4.2  | The coherence measurement setup . . . . .  | 80 |
| 4.3  | The camera and the slits for the measurement of the coherence in the mask-aligner. . . . .                           | 81 |
| 4.4  | The camera used for the angular extent measurement. . . . .  | 81 |
| 4.5  | The measurement of the interference patterns for 1 $\mu\text{m}$ slits . . . . .                                     | 83 |
| 4.6  | The contrast as a function of the spatial coherence length . . . . .   | 84 |
| 4.7  | Measurements of the interference pattern for multiple slits of 1 $\mu\text{m}$ . . . . .                             | 85 |
| 4.8  | The spatial coherence length as a function of the angle. . . . .   | 86 |
| 4.9  | A Schematics of the angles in the mask-aligner plane. . . . .  | 87 |

|  |    |
|--|----|
| 4.10 The uniformity of the spatial degree of coherence. . . . .  | 89 |
| 4.11 Measurements of the interference pattern after double slits for the corners illumination. . . . . | 90 |
| 4.12 A schematic of the 2D spatial coherence measurement principle. . . . .                            | 91 |
| 4.13 The visualization of the circular double slits for different illumination patterns. . . . .       | 93 |
| 4.14 The design of the square grating. . . . .   | 94 |
| 4.15 Microscopic measurements of a printed grating with different illumination patterns. . . . .       | 95 |





# List of Tables

|     |   |    |
|-----|---|----|
| 1.1 | Summary of the specifications. . . . .  | 8  |
| 1.2 | Laser vs LED . . . . .  | 10 |
| 2.1 | The measured specular reflectance for different polishing process at $\lambda = 405 \text{ nm}$ | 25 |
| 2.2 | Power efficiency with a specular reflectance of 66 % and 78 % . . . . .                         | 28 |
| 2.3 | The expected irradiance for LEDs module of different sizes . . . . .                            | 29 |
| 2.4 | Summary of the irradiance level measurements . . . . .  | 42 |
| 2.5 | Summary of the uniformity measurements . . . . .  | 47 |
| 2.6 | Exposure time used for the prints with the different illumination patterns . . . .              | 50 |
| 3.1 | Design constrains of the coherence measurement tool . . . . .                                   | 61 |
| 3.2 | Pairs of slits . . . . .  | 65 |
| 4.1 | Contrast measurement in the mask-aligner . . . . .  | 88 |



# Acronyms

**CNC** Computer numerical control  
**CPC** Compound parabolic concentrator  
**FWHM** Full width at half maximum  
**IFP** Illumination filter plate  
**LED** Light emitting diode  
**MEMs** Microelectromechanical systems  
**OPC** Optical proximity correction  
**PCB** Printed circuit board  
**PWM** Pulse width modulation  
**UV** Ultraviolet



# Introduction

The development of the new, ground-breaking technologies is an amazing opportunity for any scientific researcher. Such technologies are aiming at making life easier, by helping the progress of various fields such as the agriculture, the medical domain, transportation, communication, energy management. Unfortunately, challenges have come with the development of such technologies. The industrialization has been life-saving for the societies, but it also brought unforeseen problems with regards to pollution, environmental damages, security or social inequalities. These problems will most probably find their solutions in the technologies as well. In the last decades, it became very clear that sciences should not only focus on the research and “how to make new, ground-breaking technologies?” but also on the development and “how to improve what we already do to make it more efficient, less damaging and more sustainable?”.

The work presented in this thesis touches both categories of research and development. It is part of a CTI (now InnoSuisse) project with the industrial partner SUSS MicroOptics SA <sup>1</sup>. The first part of the thesis is focused on the development of a novel illumination system for mask-aligner lithography. Mask-aligner lithography is a technology used to replicate patterns from a mask to a photosensitive substrate. It is used for the fabrication of patterns with critical dimensions in the micrometer range. Common applications for which this technology is used are the fabrication of MEMS and micro-optical components, for example. Traditionally, the light sources used for mask-aligners are high-pressure mercury arc lamps, which emit in the UV range, with peaks at 365nm, 405nm and 435nm, the so-called g-, h- and i- lines. These lamps suffer from several disadvantages, such as a low efficiency, bulkiness, and the toxicity of mercury. Finding an alternative to mercury arc lamps would therefore contribute to improving the current technologies towards more sustainable options, while offering new possibilities. For example, specific techniques in mask-aligner technologies like Talbot lithography, multiple exposures, mask-source optimization or optical proximity correction lithography require high power sources with an increased control over the angular distribution and the spatial coherence of the source. These kind of techniques require more fundamental research over the spatial coherence of the illumination, how to control it and how to make use of it to improve the structures printed, enhance their resolution, and achieve results that would otherwise be unattainable.

---

<sup>1</sup>MURMELI, 18188

## Introduction

---

In recent years, high power ultraviolet LEDs at the same wavelengths as a mercury arc lamp have appeared on the market. The advantages of the LEDs are numerous. They have a smaller Etendue, can be electronically driven at high frequencies and they have a superior lifetime. This thesis focuses on the development and study of a novel LED-based illumination system for mask aligner lithography. This illumination system consists in an array of 7x7 LEDs. Individual reflectors are used to collect the light from the LEDs. The light is then brought onto a fly's eye integrator with two subsequent lenses which shape and homogenize the light field. The source can create different illumination patterns on the fly's eye integrator, determining the angles and the spatial coherence in the mask plane. This kind of control over the coherence of the light source can later on enable new printing techniques. This is the kind of research which achieve a little step toward the development of ground-breaking technologies.

The first chapter of the thesis presents the design of existing illumination systems for mask-aligners and the specifications and principles used for the illumination scheme. The second chapter details a complete set of characterizations of the final prototype including: the irradiance and intensity measurements at the output of the reflectors and the fly's eye integrator; the irradiance uniformity in the mask-plane of a MA/BA8 Gen3 SUSS mask-aligner; a set of print tests for different illumination patterns. The third chapter of the thesis is focused on the description of a method to measure the spatial coherence. It is based on a double slit and multi slits approach and is validated by simulations. Finally, a compact system is described, which enables the measurement of the spatial coherence in the mask plane, where only little space is available. An original method is also developed to measure the directional spatial coherence in two dimensions in the mask plane of the mask-aligner.

# 1 Illumination for mask-aligner lithography

## 1.1 Motivation

In microlithography, three main techniques exist to transfer patterns from a mask to a photo-sensitive substrate: mask-aligner lithography in contact printing or proximity printing and projection lithography, where projection optics is added between the mask and the wafer. Usually projection and proximity printing are preferred, as the mask is not in contact with the resist and is therefore preserved from an early wear-out [1]. Mask-aligner lithography is widely used for the fabrication of structures in the micrometer range, because of its robustness and its cost-effectiveness. This process is typically used in fabrication technologies for MEMS, back-end semiconductor, micro-optics, photovoltaic, LED packaging, and other similar applications. A light source is used to illuminate the mask. The light passes through the mask and reaches a photosensitive resist which will polymerize under exposure to the light. In mask-aligner lithography, the illumination properties are very critical to make high-quality prints. The illumination in the mask plane needs to be as homogeneous as possible, with values below 3 % uniformity over areas as large as 200 x 200 mm [2]. The angular distribution of the radiation in the mask plane also has a big impact on the print quality and the intensity level determines the exposure time and thus the achievable throughput. Mask-aligner lithography, in the spectral range of 350 to 450 nm, traditionally uses mercury arc lamp illumination. Those light sources present several disadvantages, which make them outdated: they are bulky; they are potentially dangerous because they contain mercury; they have a low electrical to optical power conversion efficiency with only about 1.5 to 5 % of the electrical power reaching the mask plane; they need a warm-up time of about 30 minutes and therefore cannot be switched on and off for each exposure; they have a short life-time, as the lamp light bulb has a lifetime of 100 days which is easily reached, because the lamp remains continuously on.

Emerging specific lithography techniques in mask-aligner technologies like Talbot lithography, multiple exposures, mask-source optimization or optical proximity correction lithography also require high power sources. Those techniques demand an increased control over the angular distribution and the spatial coherence of the source, which is not easily done with

mercury arc lamps.

It appears evident that new solutions are needed to replace the limited mercury arc lamps and to find a source that is more sustainable and versatile. In the recent years, a lot of progress has been made with solid-state light sources that operate between 350 and 450 nm. These sources now have a power density which is interesting for the requirements of mask-aligner illumination, and more generally for high-power UV illumination. Both laser sources and LEDs are candidates in this work. LEDs are chosen after a first preliminary study. The reasons will be explained in the following sections.

## 1.2 Basics of illumination systems

### 1.2.1 Etendue

The main challenge, when designing an illumination system, is to transform the size and angular distribution of a given light source into an illuminated area and angular extent which correspond to the requirements. In general, this conversion is ruled by the law of Etendue [3]. Considering a beam of radiation of cross section  $S$  and solid angle  $\Omega$ , as shown in Fig. 1.1, the Etendue is the integral over the surface  $S$  and the solid angle  $\Omega$ , of the product of an element of surface  $S$  with an element of direction cosine solid angle  $\Omega$ . This can be written as shown in Eq. (1.1) [3]. In an optical system, the Etendue is globally conserved. The Etendue is expressed as:

$$E = n^2 \int_S \int_{\Omega} dx dy dL dM, \quad (1.1)$$

where  $dx$ ,  $dy$  are small increments in position,  $dL$ ,  $dM$  are small increments of the direction cosine solid angle with respect to  $x$ ,  $y$ .

### 1.2.2 Irradiance and intensity

Both the irradiance and the intensity are used according to the description found in the specialized literature about illumination, for further details, the reader can refer to [4] and [5]. Throughout the following chapters, the irradiance is defined as the flux per unit area received by a surface and is expressed in  $W/cm^2$ . The radiant intensity is the flux per unit angle and is expressed in  $W/sr$ . It is called simply “intensity” throughout the manuscript.



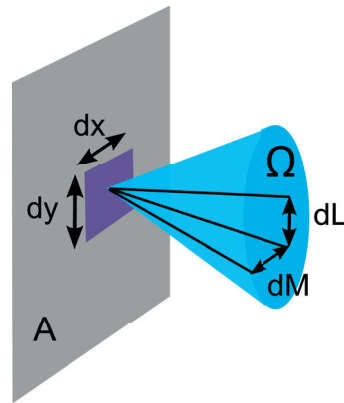


**Figure 1.1** – A schematic of the optical Etendue of a light emitting object.

### 1.2.3 Beam shaping and homogenization

In general, in mask-aligner lithography, the illumination consists of a lamp placed in a reflector to collect and collimate the light. The collection is followed by different optical elements which shape the beam and transform the angular distribution of the light source and its area into those required for the illumination. It is also at this stage that the homogenization of the light field is done. A standard way to create a homogeneous illumination is by using a so-called “Koehler illumination”, as shown in Fig. 1.2. It is a very well known illumination scheme which has the advantage of creating a homogenized irradiance in the illumination plane. It also enables a good control of the spatial coherence by determining the angular distribution by varying the size of the aperture before the condenser lens. Each point of the source participates in the illumination of the whole plane. This makes the irradiance in the illumination plane insensitive to variations of irradiance over the source. Non-uniformities appear if the intensity of the source is not uniform. In the case of lithography, the mask with the features to be replicated, is placed in the illumination plane. This is called the “mask plane”.

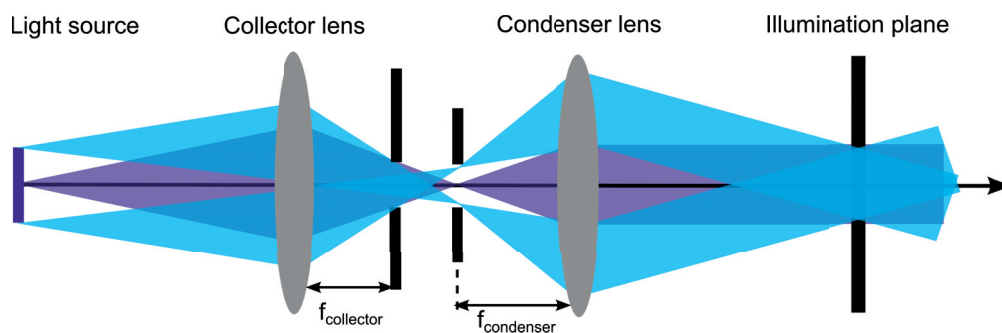


**Figure 1.2** – A schematic of a Koehler illumination. Each point of the source participates in the whole field of the illumination plane, making the illumination insensitive to the irradiance variations of the source.

In order to go one step further, a multichannel version of the Koehler illumination system can be built by using microlens arrays, as shown in Fig. 1.3. It is called a Koehler

integrator, or fly's eye integrator. Arrays of microlenses are widely used to homogenize the light field in illumination optics as presented by Dross et al. [6] and Schreiber et al. [7]. As shown in Fig. 1.3, a fly's eye integrator consists in a tandem of identical microlens arrays with focal length  $f$  and pitch  $p$ . The second array is placed in the focal plane of the first one, with the lenses facing each other. They divide the light into a multitude of channels, each one forming a secondary source. The light coming into each channel is transformed into a constant intensity within the acceptance angle of the lenslets, provided that the irradiance is constant over one channel. This can be achieved by taking small microlenses. The light coming out of each channel is then superimposed in the illumination plane thanks to the condenser lens. The condenser lens is sometimes referred to as the "Fourier lens" as it performs the Fourier transform by converting the position of the point sources into angles. This transforms the flat-top angular distribution after the integrator into a flat-top in the irradiance distribution in the illumination plane. The homogenization of the irradiance is achieved as each channel is projected onto the whole illumination plane. When the angles arriving on the microlens array match the acceptance angle of the lenses, the Etendue is conserved. If the angles arriving on the microlenses are bigger than its acceptance angle, the light will not focus on the facing lens and will therefore arrive on a neighboring channel. This phenomenon is called cross talk and should be avoided, as the light is then not superimposed in the illumination plane and Etendue conservation is not achieved. The Koehler integrator approach has the advantage of mixing both the irradiance and the intensity of the source. In the case of mask-aligner illumination, the mask is put in the illumination plane, and this plane is called the "mask plane".

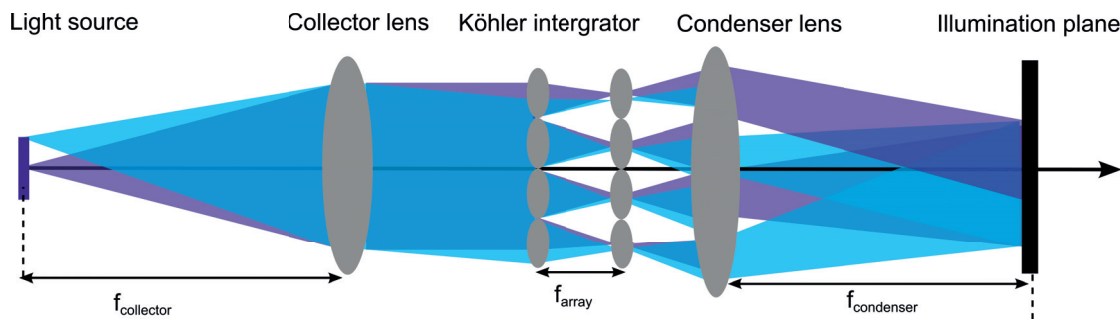


**Figure 1.3** – A schematic of a fly's eye integrator. The microlens arrays create secondary sources which are superimposed in the illumination plane using a condenser lens (or Fourier lens). This setup homogenizes both the irradiance and the intensity.

### 1.3 Mask-aligners with MO Exposure Optics®

#### 1.3.1 Design of illumination systems

The illumination design of a mask-aligner with a specific beam shaping optics is shown in Fig. 1.4. The beam shaping optics is named MO Exposure Optics® and it is used to obtain very good homogeneity levels of less than  $\pm 2.5\%$ . The homogeneity is measured as a contrast

### 1.3. Mask-aligners with MO Exposure Optics®

between the point in the mask plane with the highest irradiance and the point with the lowest one. The equation is described by Eq. (2.4) in Chap. 2. The mercury arc lamp is placed in the focal point of an ellipsoidal reflector, which collects the light from the different angles. The light is directed onto a first fly's eye integrator. The fly's eye integrator divides the light into a multitude of channels, each one forming a secondary source. The space distribution of those secondary light sources is then turned into a flat-top angular distribution thanks to the "Fourier lens". The second field lens is placed to ensure collimation. The light then goes through another round of homogenization managed by the second fly's eye integrator, which usually consists of cross-cylindrical lenses. It is followed by its corresponding Fourier lens, which converts the angular distribution to a flat-top pattern and the front lens ensuring the telecentricity. The Illumination Filter Plate (IFP) is a shaped anodized aluminum plate, as shown in the Fig.1.5, which acts as an amplitude filter. This filter is placed before the second integrator and makes it possible to shape the angular distribution in the mask plane. The angular distribution in the mask plane has an important impact when printing in proximity lithography, as it modifies the coherence properties in the mask plane and the diffraction and interference effects. The size of the light beam in this plane determines the angular extent of the light in the mask plane, which is usually  $1^\circ$  to  $7^\circ$ . The working principle and advantages of such an illumination system are extensively detailed in the work of Voelkel et al. [8]. The part that should be replaced by a new system is delimited with the dashed line.

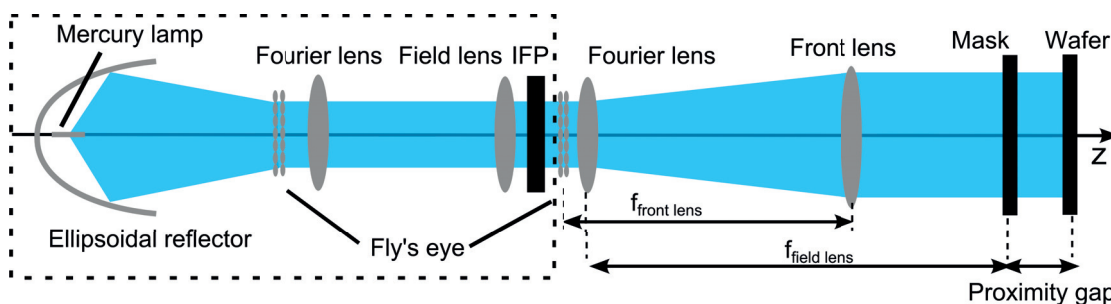


**Figure 1.4** – A schematic of the illumination optics of a mask-aligner with MO Exposure Optics®. The part to be replaced is delimited with the dashed line.

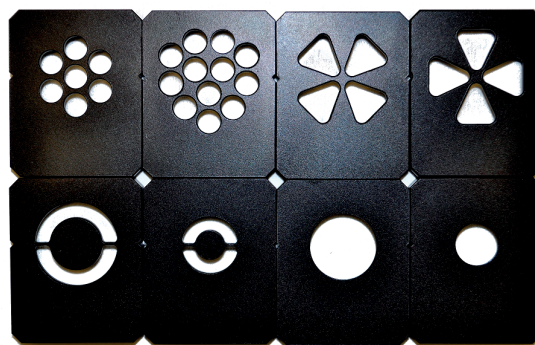


**Figure 1.5** – The illumination filter plates found in the MO Exposure Optics®

### 1.3.2 Summary of the specifications

In order to determine if it is possible to replace a mercury arc lamp for illumination system in mask-aligners, it is important to define the specifications needed for such a source. The requirements to replace a 1 kW mercury arc lamp are an irradiance of 100 mW/cm<sup>2</sup> in broadband over a minimal area of 200 x 200 mm<sup>2</sup> with angles within < 1 ° to 7 °. A second specification which has to be met is the homogeneity of the field, that should match or surpass the capability of standard mask-aligners. Typical mask-aligners present a mask-level field homogeneity of ±3 % for standard illumination optics and ±2.5 % with the MO Exposure Optics®. A last point to consider is the angular distribution at the mask level, which has a high impact on the quality of the print. The angular distribution should still allow to print with the same quality as with a standard mask-aligner illumination. The mask-level angular distribution should be adaptable as what is currently done with the illumination filter plates. A summary of the specifications is given in the table 1.1.

*Table 1.1 – Summary of the specifications.*

| Specification                            | Value                   |
|--|-------------------------|
| Irradiance in broadband, 1kW lamp        | 100 mW/cm <sup>2</sup>  |
| Irradiance in broadband, 350W lamp       | 30 mW/cm <sup>2</sup>   |
| Irradiance in i-line, 1kW lamp           | 35 mW/cm <sup>2</sup>   |
| Irradiance in i-line, 350W lamp          | 7 mW/cm <sup>2</sup>    |
| Mask plane area                          | 200x200 mm <sup>2</sup> |
| Angular extent                           | <1 ° to 7 °             |
| Irradiance homogeneity in the mask plane | ±2.5 %                  |
| Adaptable angular distribution           | IFP or better           |

In term of application, the source should be easily installed in existing mask-aligner as well as easily integrated to new design. This means that the compactness should be at least equivalent to the existing mercury lamps, and ideally better in order to save expensive clean room space. Other specifications are improvements that can be made to the current system. Having an easily scalable illumination would be great, as well as have new functionalities. An easily modifiable angular distribution in the mask plane, which results in a better control over the spatial coherence is also interesting.

### 1.4 Towards solid-state sources for mask-aligner illumination

#### 1.4.1 Choosing between laser and LEDs

In recent years, high-power solid-state light sources at 350 to 450 nm appeared on the market, opening new doors for better illumination performance for mask-aligners. The advantages of solid-state sources for such an application are numerous. Firstly, they have a lifetime which is much superior to the mercury arc lamp; secondly, they are easily switchable so can be turned on only when necessary. Other advantages are that they are safe, more compact and do not require any maintenance. The main challenge is to be able to reach the power requirements. In considering solid-state sources for mask-aligners, they are two main options to choose from: laser or LEDs.

Lasers present the advantages of being easily collimated as they are very close to a point source and therefore have a very small Etendue. The main challenge consists in homogenizing the beam, as the coherence properties result in interference effects, such as speckles or dots, when trying to shape and homogenize the field with diffractive optical elements or microlenses. Example of such effects are presented in Fig. 1.6.

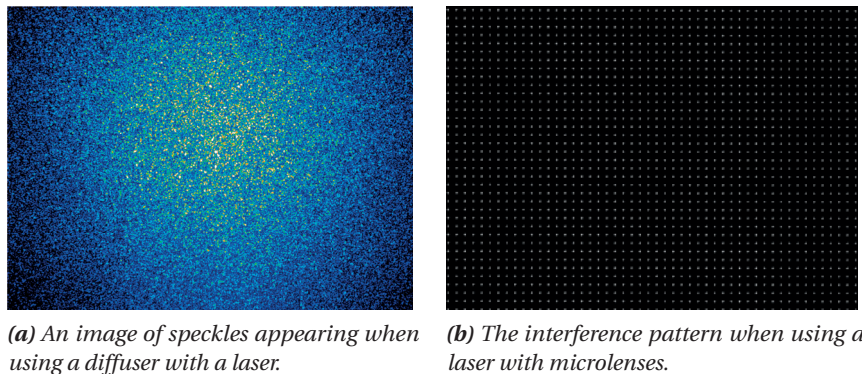


**Figure 1.6** – Examples of interference patterns which occur when trying to shape and homogenize a laser diode with (a) a diffusing element and (b) a set of microlenses.

In order to remove such undesirable interference effects, only few solutions exist such as moving diffusers, adaptive mirrors, etc. This was done with a combination of diffuser and microlenses by Voelkel et al. in [9] and with the help of a step mirror by Erdmann et al. [10]. The homogeneity obtained when averaging over the exposure time would be sufficient to make prints, but at the cost of a loss of optical power. An example of a successful application of laser illumination for mask-aligner lithography has been presented recently at 355 nm by Weichelt et al. [11] who achieved an optical power of 3 W and at 193 nm by Kirner et al. [12], but for which the optical power at the output of one laser in CW is only of 10 mW. In order to decide which kind of source to focus on, the power exchange is calculated. The calculation is based on the sources available at the beginning of the project, in 2014. The power from a Toptica laser diode at 405 nm is given to be about 210 mW for a collimated beam

## Chapter 1. Illumination for mask-aligner lithography

diameter of 0.35 mm. This gives an irradiance of 17 W/cm<sup>2</sup>. In comparison, a Nichia LED at 405 nm has 1.4 W for an emitting die surface of 1.2 mm x 1.2 mm, which gives an irradiance of 97 W/cm<sup>2</sup>. In that regard, the LED seem more interesting, but the LEDs are more complicated to collimate as they have a larger emitting area, which means that some light might be lost in the process of light shaping. The determining factor is that, in order to form a high power source, both solutions need a stacking of individual sources. The housing dimension of the laser makes it, in practice, very complicated to reach the required power. A standard 350 W lamp (which is the smallest lamp for a mask-aligner) provides 30 mW/cm<sup>2</sup> over an area of 20 x 20 cm<sup>2</sup>. This means about 12 W of optical power in the mask plane. To have 12 W with laser diodes, about 60 lasers would be needed, without taking into account any losses. The housing being about 10 x 4 x 4 cm<sup>3</sup>, this results in a source far too big. On the contrary, the LEDs mentioned above with a die of 1.2 mm have a packaging size of 3.5 x 3.5 x 1.23 mm<sup>3</sup> for about 1 W of optical power. The characteristics of the two types of sources are described in the table 1.2. This makes it feasible to mount enough LEDs on a PCB to reach the needed power, while compensating for the losses. The LEDs can be wired in such a way that the largest part of the electronics is on the side. A first approximation shows that, with a system based on an 7x7 array of 1 W LEDs and 60 ° illumination angle, it is possible to reach an irradiance level that is comparable to existing systems with mercury lamps. This is why LEDs are chosen in the scope of this project. Depending on the application, lasers can still be a better choice, especially for applications where a high level of collimation is needed.

*Table 1.2 – Laser vs LED*

| Source | Angular extent | Power per unit | Units needed | Housing size                     |
|--------|----------------|----------------|--------------|----------------------------------|
| LED    | ±60 °          | 1 W            | 49           | 3.5 x 3.5 x 1.23 mm <sup>3</sup> |
| Laser  | <1°            | 10 mW          | 60           | 10 x 4 x 4 cm <sup>3</sup>       |

### 1.4.2 Mask-aligner illumination system with a stack of LEDs

In order to meet the requirements in terms of optical power and irradiance, a solution for arranging multiple LEDs together needs to be found. Various examples of modeling and realizations of illumination systems based on LEDs are described in the literature, for lighting applications[13], projectors[14, 15] or lithographic applications[16, 17]. We can see that different strategies can be applied to collect the light from an LED. The main ways to do it are by refraction with a lens, or by reflection with a reflector or by a combination of both, using total internal reflection, with freeform optics [18, 17] and dielectric multilayers [19]. Collecting the light from an array of LEDs using a lens or a set of lenses is intuitively the cheapest and easiest solution. It presents several disadvantages which appear when collecting the light from an extended source with angles of ±60 ° and collimating the light to less than ±10 °. Indeed, the lens required to do so would have to have simultaneously a large diameter and short focal length, which means a high curvature and a system that is not very compact. Fresnel lenses can be used as presented by Erickstad et al. in [16], but the system still has quite large

#### 1.4. Towards solid-state sources for mask-aligner illumination

dimensions. Furthermore, custom lenses or freeform optics are usually made of polymers. This poses the question of the durability over the long term, as polymers are known to wear out quickly when exposed to high intensities in the UV range. The reflector approach has an advantage in this regard, as it can be fabricated with materials that are very durable. But this approach presents other disadvantages, mainly due to the fact that the reflectors become quickly very long for small angles and that it is therefore also complicated to fabricate.

A way around this problem is found with the development of a modular LED-based optical system. The concept is similar to what is theoretically presented by Van Giel et al. [15], but multiple functional prototypes of the system are built. High power UV LEDs are used with optical reflectors in order to collect the light and homogenize the intensity. A high-power source can be formed by putting together multiple LED channels inside of individual hollow reflectors made of aluminum. There are two main advantages of using individual reflectors instead of a large one with multiple LEDs in the entrance aperture. The first advantage is that, by using individual reflectors, the system is more compact as the space lost to the packaging of the LED is used for the mechanics. The second advantage is that it forms a modular source which can easily be adapted to custom requirements, as the reflector does not need to be resized when putting together a module of different power. The compactness and versatility of the system ensure that the source can directly be mounted into standard mask-aligners. As shown in the schematic of Fig. 1.7, the light emitted with large angles can be brought within the acceptance angle of the fly's eye integrator. The angular distribution coming out of the reflectors is already homogenized going through the reflectors. This has the advantage of allowing the removal of the first set of integrators and its two lenses, if correctly designed. The last part of the setup of Fig. 1.7 is the same as in Fig. 1.4.

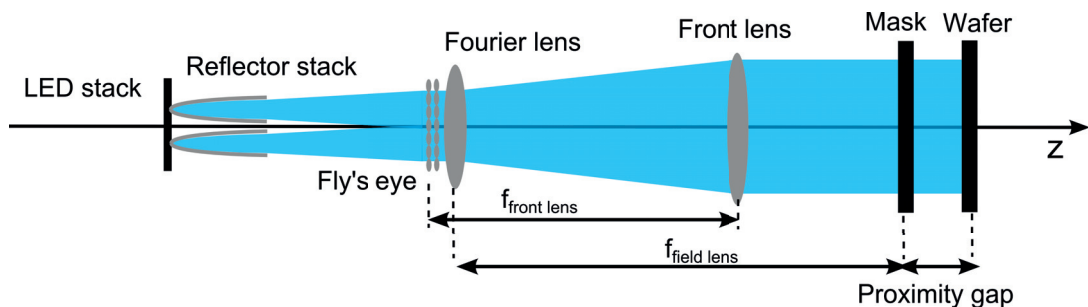


**Figure 1.7** – A schematic of the illumination optics of a mask-aligner when replacing the mercury arc lamp with an array of LEDs and reflectors.

The light field on the fly's eye integrator in Fig. 1.7 determines the angular distribution in the mask plane. The reflector array must therefore have the same size as the beam in the standard system, which matches the size of the fly's eye integrator. By choosing which LED to switch on, the angular distribution in the mask plane can be modified. The IFP can thus be removed and customized angular distributions can still be created. The resulting angular distribution in the mask-plane is slightly different from the one obtained with a standard system. The angular distribution with the array of reflectors shows variations due to the different channels,

where as the arc lamp and its optics give a continuous, flat-top like spectrum. The measured spectrum are presented in the section 2.2.

In the end, the stack of LEDs and their reflectors can replace the mercury arc lamp and its ellipsoidal reflector, the first integrator, the two subsequent lenses and the IFP.

### 1.5 Phase space representation of mask-aligner illumination

The illumination systems presented above essentially transform the angular and spatial distribution. Their transformation is ruled by the conservation of Etendue. A good way of visualizing the transformation of the angular distribution and the spatial distribution of the light is by representing the different steps in a phase-space diagram. The phase-space representation has on one axis the projected solid angle distribution along one direction, and on the other the spatial distribution. The rigorous analysis of the phase space is made by using Wigner functions [20]. As explained by Zhong and Gross [21], this method has three main advantages: it allows to describe an optical signal both in phase and space; it gives information about the wave optics such as diffraction and interference effects; it directly represents the degree of spatial coherence by the angular extent. A very elegant example of an experimental measurement of the phase space distribution in two dimensions is presented by Waller, Situ and Fleischer in their work [22]. With their method, they are able to determine the local coherence properties of the source.

In this section, the analysis is made schematically. It is not going through the complete simulation with the Wigner function. This simplified approach still allows to represent the angular extent and the spatial extent at different positions of an illumination system. This allows the visualization of the requirements on the design of the illumination system. This kind of representation is done for optical systems and more specifically for integrating rods and microlenses in the works from Rausch and Herkommer [23, 24]. This kind of representation can be done for both the mercury arc lamp and the LED illumination systems. The limitation of this approach is the 2D representation. It is very appropriate for rotational symmetric system, but less so for systems with other symmetries. In the present case, one of the principal axis of the system is chosen to serve as example, knowing that other directions would give similar diagrams.

A schematic representation of the angle-space for the mercury arc lamp illumination is shown in Fig. 1.8. The scales vary from one picture to the other, as the changes of dimension are large. The first picture represents the angle-space of the lamp. It is taken around the axis which contains most of the power, which is around the middle of the lamp. The diameter of the lamp is typically around 20 mm, and its length about 100 mm or larger. The emission is quite isotropic around the middle of the lamp and is over 360°. It is the axis with the most emission. A reflector then collects the light from the lamp and direct it onto the first integrator. The second image shows the angle-space just behind the integrator. The irradiance of the light is not homogeneous at all, with peaks towards the edges and a low point in the center. The



## 1.5. Phase space representation of mask-aligner illumination

---

following image represents the angle-space right behind the second integrator. The irradiance is more homogeneous, even though it is not perfect. The angle is homogeneous because of the first fly's eye integrator. If a very close zoom is taken, the different channels of the microlens array can be seen. The pitch of the array is around 200 to 400  $\mu\text{m}$  and the diameter of the lenses is usually a few microns smaller. This means that there are small interstices within which the light is either blocked (pictured), or goes through without being refracted by the lens. The light from the different lenses is then superposed on the mask plane by going through a Fourier transformation. The irradiance in the mask plane is therefore homogeneous. The angular extent depends on the size of the light field on the second integrator, but is typically between 1 and 7 degrees of full angle. The angles are homogeneous, apart from the edges.

As a comparison, the schematic representation of the angle-space for the LED illumination is shown in Fig. 1.9. The light source is taken an array of 3 LEDs placed at 10 mm from each others. Each LED has a emission area of a few millimeters, over an angular range of  $\pm 60^\circ$ . This means that, individually, they have a much smaller Etendue than the mercury arc lamp. The light is collected by the reflectors. The angle-space representation of the light after the reflectors is shown in Fig. 1.9b. For a given position, the intensity is homogeneous. The irradiance is not homogeneous. The corners of the reflectors have more light and the mechanics between the channel leaves a space without light. The light propagates to the fly's eye integrator. This has the effect of smoothing already some of the non-uniformities of the irradiance. The space between the channel disappears. Right after the fly's eye integrator, the light is once again separated into each microlens. It is then Fourier transformed onto the mask plane. In the mask-plane, the irradiance is homogeneous. The angular distribution is the same as the irradiance on the fly's eye integrator. Some angles have less intensity than others but the distribution is very different than for the mercury arc lamp. The impact of the difference of the angular spectrum can only be evaluated with print tests or aerial images simulations.

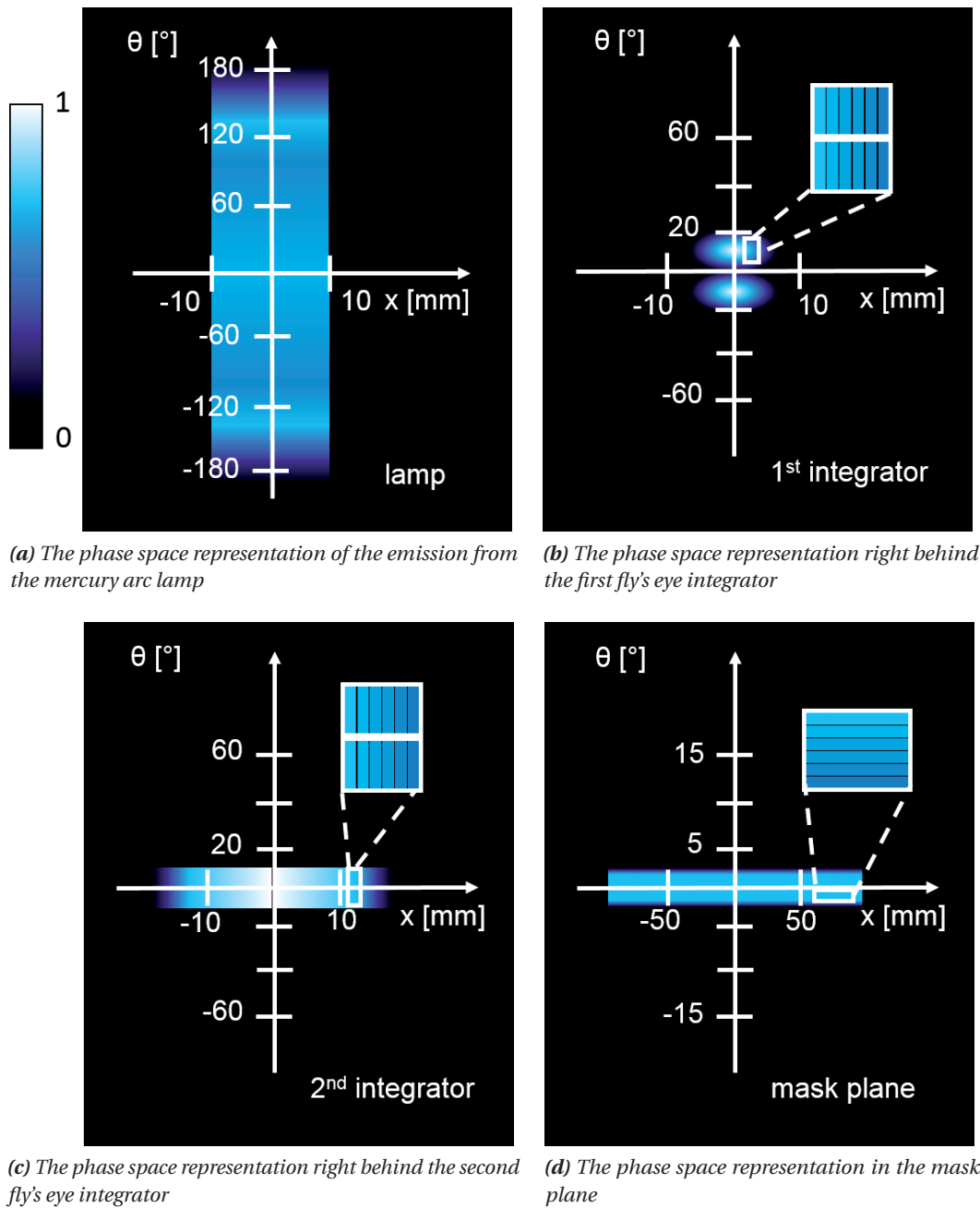
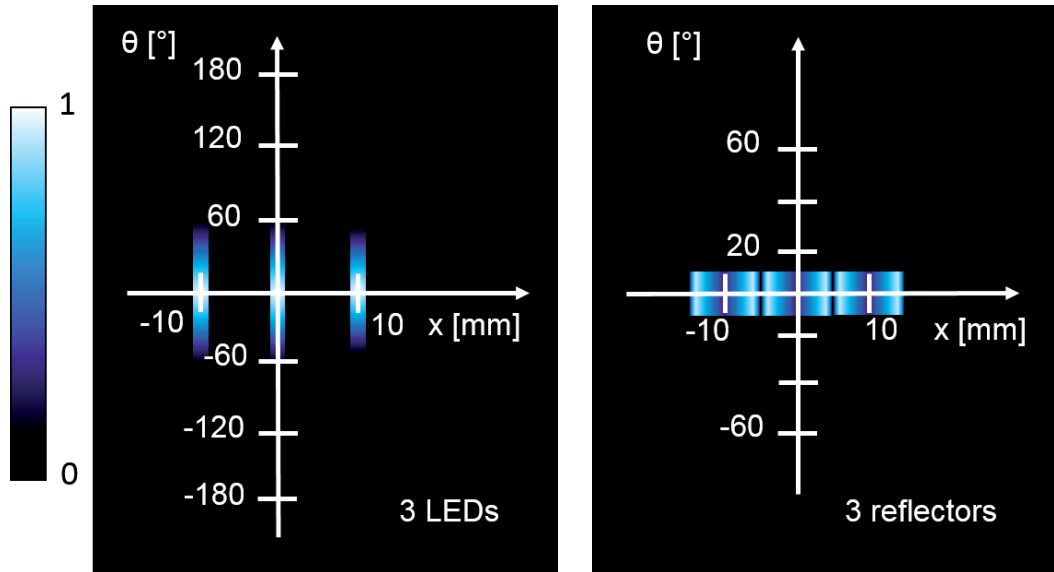


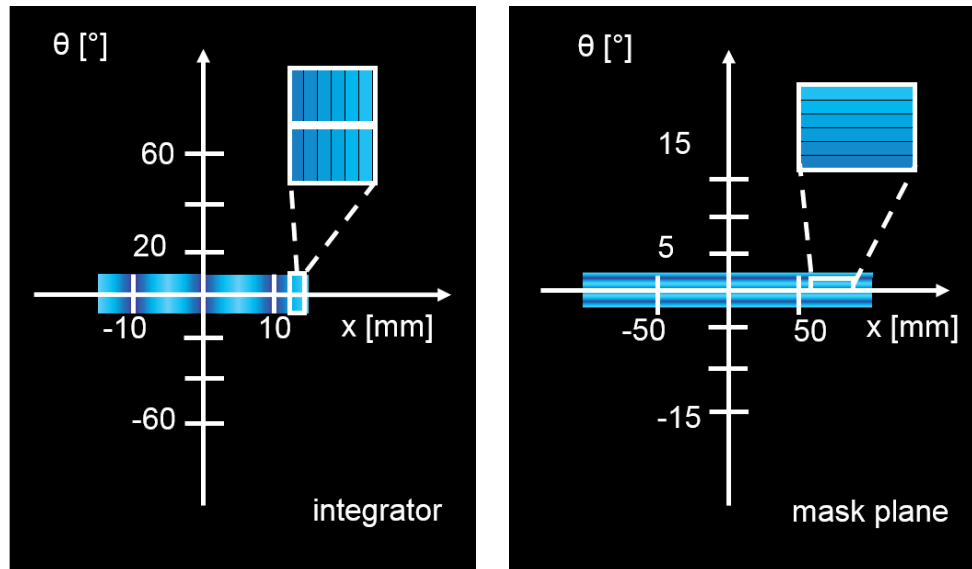
**Figure 1.8** – A schematic of the phase space transformation in a mask-aligner equipped with MO Exposure optics.

## 1.5. Phase space representation of mask-aligner illumination



(a) The phase space representation of the emission from the mercury arc lamp

(b) The phase space representation right behind the reflectors



(c) The phase space representation right behind the fly's eye integrator

(d) The phase space representation in the mask plane

**Figure 1.9** – A schematic of the phase space transformation in a mask-aligner equipped with an LED illumination system.



## 2 High power UV LED illumination system

This chapter describes the design of the LED-based illumination system, which is developed to replace the mercury arc lamps for mask-aligner lithography. The chapter is separated into two main sections: the design and the characterization. The design part comports the optical design, the mechanical design and the electrical design. The characterization is made to confirm that the requirements presented in section 1.4.2 are met.

### 2.1 Design

In this design section, the optical design of the LED-based illumination system is first described, followed by the mechanical design, the simulation, the fabrication considerations and the electrical and thermal management design.

#### 2.1.1 Optical design

As described in section 1.4.2, the novel illumination system is based on an array of LEDs mounted with individual reflectors. The shape of the reflectors determines how the light is collected and collimated. The bulkiness of the illumination system also very much depends on the size of the individual reflectors. The reflectors should be able to collimate the light within  $\pm 10^\circ$ . This angle corresponds to the numerical aperture of the microlens array forming the fly's eye integrator and which comes directly after the output of the reflectors, in the optical system of a mask-aligner.

The reflector shape is based on a parabolic compound concentrator (CPC). This design of concentrators is commonly used for solar applications [3, 25]. Instead of being used as a collector, it is here thought as an illuminator. This has already been suggested by Gordon et al. in [26]. As shown in Fig. 2.1 and 2.2, the source is placed in the entrance aperture of size  $2a$ , and the output is a light distribution within the angular extent  $\theta_{max}$  and over the output aperture  $2a'$ . The conservation of the Etendue determines the relation between them, as explained in Chap. 1.

## Chapter 2. High power UV LED illumination system

The surface reflecting the rays is a fraction of a parabola. The axis of the parabola is tilted accordingly to the angular extent needed at the output. The center of one of the parabola is placed at the starting point of the other, and reciprocally. It can be described by a parametric equation, given by Eq. (2.1) [3], with the use of the cylindrical coordinates. The geometry is shown in Fig. 2.1. The radius of the input aperture is given by  $a$  and the radius of the output aperture by  $a'$ .  $\theta_{max}$  is the angular extent at the output of the reflector. The radius varies from 0 to  $a'$  and  $\phi$  from  $2\theta_{max}$  to  $\pi/2 + \theta_{max}$ :

$$\begin{cases} r = \frac{2f \sin(\phi - \theta_{max})}{1 - \cos \phi} - a, \\ z = \frac{2f \cos(\phi - \theta_{max})}{1 - \cos \phi}, \\ f = a(1 + \sin \theta_{max}) \end{cases} \quad (2.1)$$

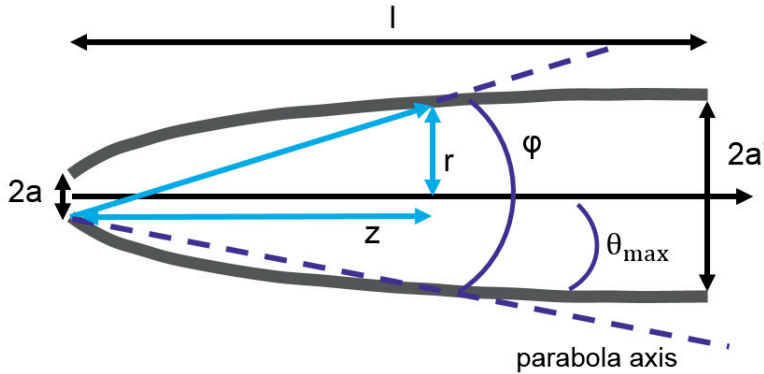


**Figure 2.1** – A schematic of the parabolic compound concentrator. The entrance aperture is  $a$ , the output aperture is  $a'$ , the angular extent is  $\theta_{max}$ .

The rays in black in Fig. 2.2 are emitted with an angle of  $\theta_{max}$ . The rays in purple are emitted with an angle close to  $90^\circ$ , which is the limit for the light to be collected by the reflector. The rays in blue have an emission angle of  $45^\circ$ . Depending on the starting position in the input plane and their angle, the rays will be reflected a different number of times. One of the ray in blue is reflected 3 times and one is reflected one time. The output aperture size and length of the reflector are both determined by the entrance aperture  $a$  and the angular extent  $\theta_{max}$  wanted at the output of the reflector. The conservation of the Etendue determines the relation

between the different parameters. They are linked by the following relations:

$$\begin{cases} l = \frac{a(1 + \sin\theta_{max}) \cos\theta_{max}}{\sin^2\theta_{max}}, \\ a' = \frac{a}{\sin\theta_{max}} \end{cases} \quad (2.2)$$

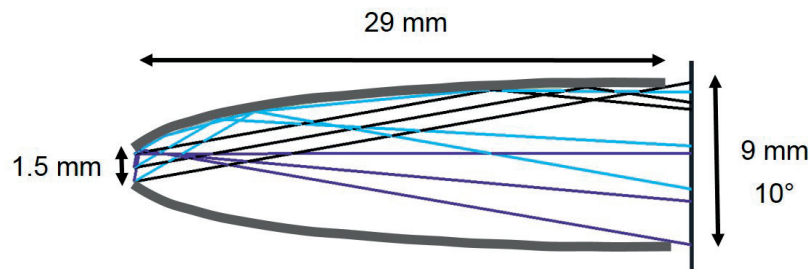


**Figure 2.2** – A FRED simulation of the parabolic compound concentrator. The black rays have a maximum emission angle of  $\theta_{max}$ , the purple rays have an emission angle close to  $90^\circ$  and the rays in blue have an emission angle in-between.

In our case, the entrance aperture is given by the size of the emitting area of the LED, which is of  $1.5 \times 1.5 \text{ mm}^2$ ; the exit angle  $\theta_{max}$  is given by the acceptance angle of the fly's eye integrator, which is  $\pm 10^\circ$ . These two constraints, introduced in Eq. (2.2), result in an output aperture of 8.6 mm and a length of 28.7 mm. Looking at the equations, there are an important thing that can be concluded. If one wants to make the collimation angle much smaller, the length of the system increases very rapidly. This is because (for small angles):

$$\lim_{\theta_{max} \rightarrow 0} l \approx \frac{a}{\theta_{max}^2}.$$

As an example, trying to collimate the angles to  $\pm 5^\circ$  with the same input aperture of 1.5 mm results in a length  $l = 41 \text{ cm}$ , and an output aperture of  $a' = 17 \text{ mm}$ . This would make the stacking of multiple LEDs a lot less compact.

### 2.1.2 Mechanical design

The mechanical design plays an important role in the overall efficiency of the illumination device. The challenge is to have the highest power density possible while taking into account the overall size of the LED. The emitting area of an LED has a finite size, which is smaller than the overall packaging size of the LED. This means that the active size of the LED is much smaller than the passive size of the LED. The compactness of the array of LEDs is therefore limited by the packaging size of the LEDs. Furthermore, each LED has to be wired electronically, which also adds up to the space required. From a mechanical point of view, there is also the challenge

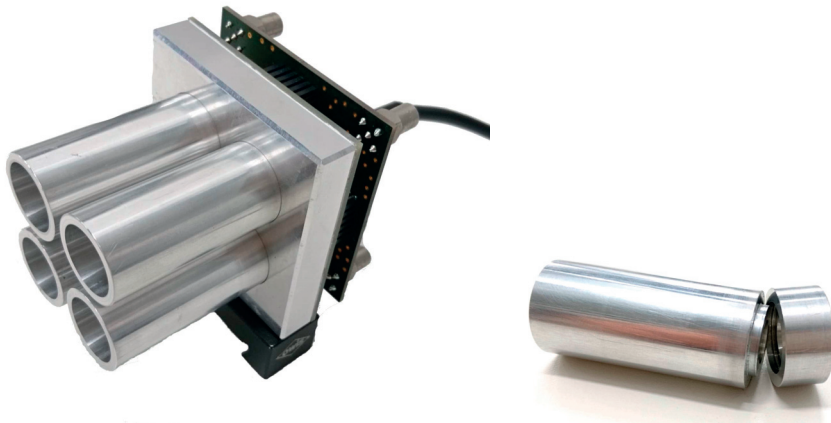
## Chapter 2. High power UV LED illumination system

---

that the reflector should be easy to manufacture. There are two reasonably cheap solutions, which will be presented: the first one is to have a rotational symmetric reflector, which can be machined using a turning machine. The second solution is to have square reflectors. The second solution presents more challenges for the manufacturing, because of the angles in the corners of the square reflectors. It is, in any, case difficult to machine the reflectors, as they are long for a small aperture. The machining tool should therefore be very small, but should still allow to machine deep.

### Preliminary rotational symmetric prototype

The first prototype, which is developed, is based on a rotational symmetric reflector, as presented in Fig. 2.3. Four LEDs are mounted in a square. This solution is chosen for its ease of manufacturing. The pieces can be turned on a standard turning machine. For this prototype, the dimensions are not optimized to the size of the emitting area of the LEDs. The entrance diameter is 3 mm to fit the 2.12 mm of the diagonal of the emitting square and leave some margin for misalignment errors. This results in a length of 57 mm. The reflectors still have to be separated into two sections for the machining, because the tool cannot reach so deep.



(a) The first prototype of rotational symmetric reflectors.

(b) The two pieces of the rotational symmetric reflector.

**Figure 2.3** – A picture of the 2 x 2 system with rotational symmetric reflectors. The rotational symmetric reflector is made of two parts mounted together, as the tool of the tour machine is not long enough to machine down to the entrance aperture.

This first prototype proves that the system can work, but that a more compact solution has to be found. The fill factor for circles arranged in a square is quite low. The best fill factor of circles arranged in a square, without considering the mechanics, is 0.785. Going to a hexagonal (or honeycomb) arrangement of the circles improves the fill factor to a maximum of 0.907 [27]. This is without considering the size of the mechanics, as the reflectors need to have walls of a certain thickness.



One important aspect to consider is the fact that the die of the LED is rectangular. It turns out that the acceptance angle of the fly's eye integrator is also rectangular, because of the crossed cylindrical lenses it is composed of. With this in mind, it is clear that going to rectangular reflectors is a better solution. It also allows for a better fill factor (with a theoretical maximum, without the mechanics, at 1) and therefore a higher compactness. A solution for the manufacturing of rectangular reflectors is thus investigated.

### Square 2x2 prototype

The chosen solution consists in keeping one square reflector per LED, while making sure that the entrance of the reflectors fits to the emitting area of the LEDs. By putting an identical reflector for each LED, the space between each emitting area is used in an efficient way. The main challenge to build a prototype of a square reflector, is the machining. Depending on the required angular distribution and entrance area, the reflector can become very long.

In order to make them easy to manufacture and scalable, the reflectors consist of one unitary piece. This part is here called “fan” because of the slight resemblance of its shape with a hand fan. This piece is repeatedly assembled together. Four fans form a whole reflector, but each fan can be used for two reflectors, as both sides are functional. This makes it very easy to build modules of different overall power by adding more channels. From a fabrication point of view, it is also of interest to have only one piece to replicate. A photography of a fan is shown in Fig. 2.4. The piece is symmetrical and both curved faces are the active surfaces. They are polished to increase the specular reflectance.

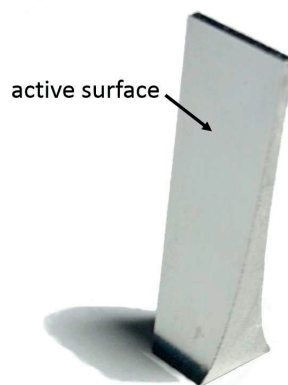


**Figure 2.4** – A picture of the fan used to form the reflectors. The two symmetrical active surfaces are polished.

A first module of 2x2 LEDs and reflectors at 405 nm is built in order to use it for optical characterization and to validate the working principle of the design. In Fig. 2.5, the assembly of four reflectors is shown. The reflectors are machined to the optimum size mentioned in the optical design section. The reflector entrance aperture is therefore set to 1.5 mm, fitting the

## Chapter 2. High power UV LED illumination system

---

size of the emitting area of the LED. The output aperture is 8.6 mm and the length is 28.7 mm for an angular range of  $\pm 10^\circ$ . The LEDs are mounted on an aluminum PCB and a plastic spacer is inserted between the reflector base and the PCB. This spacer allows to have space to place the LEDs and insulate the PCB from the reflectors to prevent any electrical contact between them. The result is a very compact, modular design, which has the advantage of being easily scalable. This system cannot function at full power as the LEDs are not cooled and would overheat. Due to the size of this prototype, it is very practical to use it for the optical characterization.

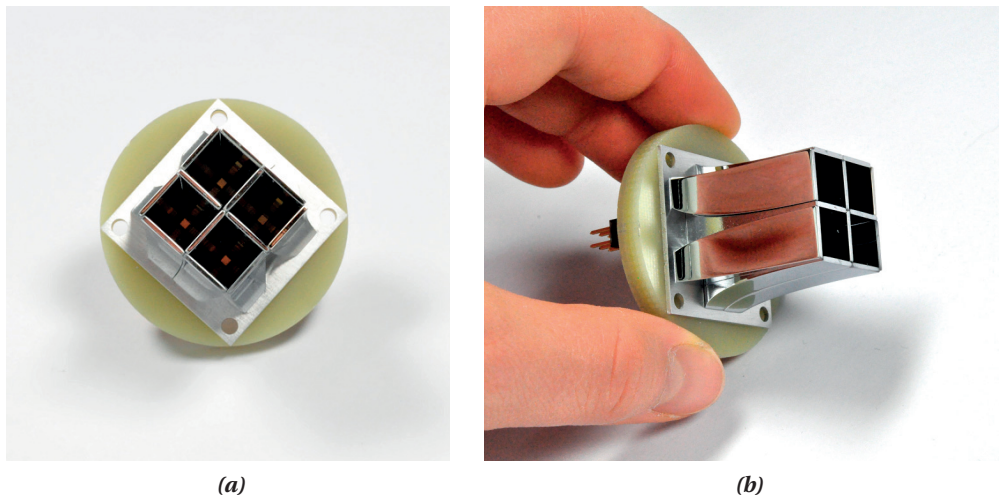


**Figure 2.5** – The mechanical design of the 2x2 squared reflector. It is interesting to notice the unique fan which is repeatedly mounted together to form the reflectors.

### Square 7x7 prototype

The last prototype has the same design as the 2x2 system, but is, this time, built to function at full power. It is a 7x7 LEDs module at 365 nm, which represents an optical power of 50 W. For this module, a cooling system has to be implemented to dissipate about 200 W. The solution adopted is a slightly over dimensioned water cooling system, which is described in the section 2.1.5. It is based on a commercially available system, which comprises water pipes and a cooling unit with a fan is used to cool the circulating water. Figure 2.6 shows the mechanical design of the 7x7 system made in SOLIDWORKS. In Fig. 2.6(a), only half of the reflectors are mounted and the LEDs can be seen in the back. The three holes are used to screw the fans. They allow the passage of two pins and one screw, which ensure a good positioning of the fans. In Fig. 2.6(b) and 2.6(c), the two parts with red holes are parts of the cooling system. The pipes with the water are attached in the red holes. The water circulates from one piece to the other and then goes into the main control box, where it is cooled with a heatsink and a fan.

A picture of the system being assembled is shown in Fig. 2.7. The PCB is coated with a black

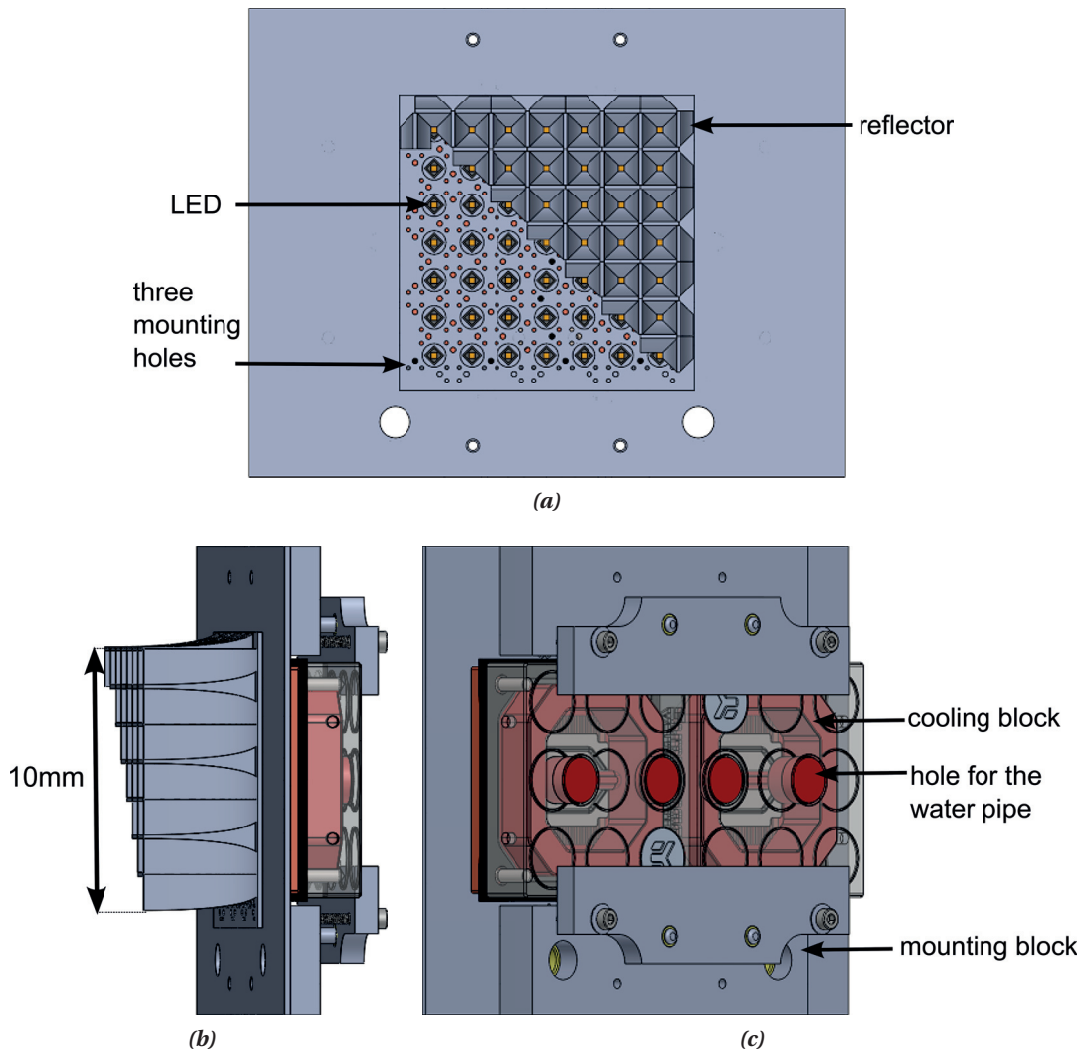


**Figure 2.6** – The Solidworks mechanical design of the 7x7 LEDs and reflectors system. In (a) the LEDs can be seen at the back of the reflectors. In (b) one can see that the system is compact. In (c) the red parts are the cooling blocks.

polymer to ensure electrical insulation. The yellow board is the spacer, which is used to compensate for the height of the LEDs. The LEDs can be seen in the holes. The reflectors stand directly on the spacer. They are screwed to the other side of the PCB. On the left is the connector through which the different electrical signals are conveyed.

In order to have an estimation of the efficiency of the reflectors, the reflectance of the polished surface for both prototypes is measured. This measurement is also used to find a way to improve the reflectivity of the reflectors, going from the 2x2 prototype to the 7x7 prototype. In order to do so, the setup shown schematically in Fig. 2.8 is used. The output of a collimated laser at 405 nm is first measured with a power meter as a reference value. The laser is then pointed on the reflective surface of the samples and the power is measured once again. The

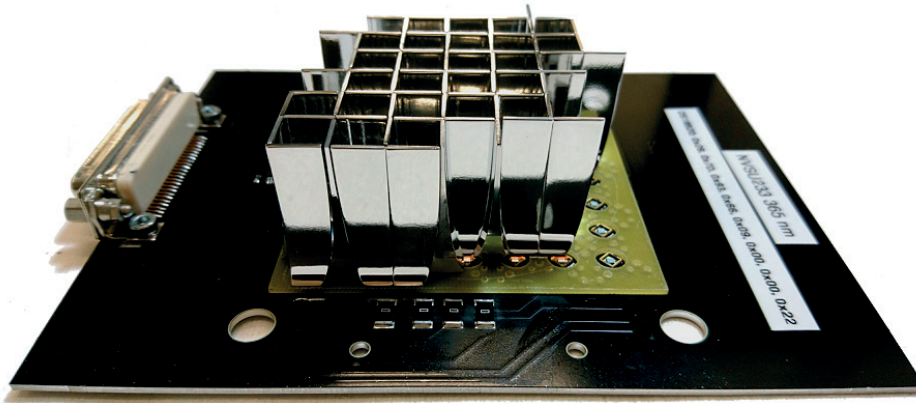


**Figure 2.7** – A picture of the 7x7 LEDs and reflectors system being assembled. The spacer is in yellow, with the LEDs inside of the holes. The wires on the PCB can be observed.

result is an estimation, as the reflectivity varies with the incident angle. Another source of error is that the surface of the sensor is slightly larger than the reflected spot. This means that not only the exact specular reflection is measured, but also a part of the scattered light within  $\pm 1.7^\circ$ , as the distance from the sample to the power meter head is  $l=150$  mm and the sensor diameter is 9 mm. The measured beam is always taken with an angle of  $30^\circ$  with the surface of the reflector and of  $90^\circ$  with the surface of the power meter head. The reflectance is calculated as the ratio between the power,  $P_{refl}$  after reflection and the power without reflection  $P_{laser}$ :

$$\eta = \frac{P_{refl}}{P_{laser}} \quad (2.3)$$

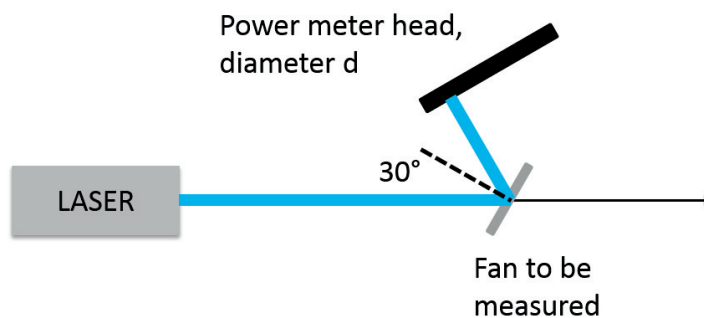


**Figure 2.8** – A schematic of the setup used to measure the reflectivity of the polished fans. The laser has a wavelength of 405 nm.

The measured value for the fans used in the 2x2 prototype is  $66 \pm 5$  % at 405 nm. In order to find a way of improving the reflectivity, two different types of aluminum, Al 6061 and Al 6082, are tested to determine what procedure gives the best specular reflectance. Different

measurements are done on the sample. The mechanical shop machining the fans provided the measurements of the surface roughness, Ra and Rz done with a profilometer. Ra gives the surface roughness vertically, with respect to the surface. The mean line of the surface is taken as reference and the arithmetic mean of the deviations from this mean gives Ra. The best achievable class of rugosity for standard fabrication is Ra= 0.025  $\mu\text{m}$  and is achievable by polishing [28]. Rz is computed as the mean, over 5 sampled measurements, of the maximum difference between the highest peak and the lowest depth of the surface. As for the 2x2 prototype, the specular reflectance is then measured with a laser at 405 nm.

The results are presented in Table 2.1 with the best results for both type of aluminum in black font. The aluminum type is given in the first column. The different levels of polishing are indicated by the numbers from 1 to 3, 3 being the best polishing achieved. Some samples are chromed, to improve the mechanical resistance of the reflectors. Some samples are first passed through a stage of “trovalisation” which consists in putting the pieces in a machine with abrasive cones and putting them in a vibrational movement. The result is a polishing of all the surfaces. The fans are then again polished by hand on the reflective surface. From the table, it can be seen that the chromed pieces have a lower specular reflectance than the pieces without chrome. Looking at the rugosity measurements of Table 2.1, the chroming process increases the rugosity, it is thus expected that their specular reflectance is lower compared to the other samples. The sample that gives the best specular reflectance is the Al 6082, passed first through the trovalisation and then hand polished with the highest degree of polishing. It results in a reflectance of  $78 \pm 5$  %. This results in a consequent improvement in the efficiency of the system, as explained in the following section.

**Table 2.1** – The measured specular reflectance for different polishing process at  $\lambda = 405 \text{ nm}$

| Alu type | Finish type | Ra [ $\mu\text{m}$ ] | Rz [ $\mu\text{m}$ ] | R $\pm$ 5 [%] |
|----------|-------------|----------------------|----------------------|---------------|
| Al 6061  | 1           | 0.052                | 0.365                | 39            |
| Al 6061  | 2           | 0.04                 | 0.32                 | 59            |
| Al 6061  | 3           | 0.052                | 0.365                | <b>74</b>     |
| Al 6061  | 3, chromed  | 0.127                | 0.735                | 55            |
| Al 6061  | troval, 3   | 0.06                 | 0.393                | 71            |
| Al 6082  | 1           | 0.045                | 0.338                | 23            |
| Al 6082  | 2           | 0.036                | 0.321                | 62            |
| Al 6082  | 3           | 0.04                 | 0.271                | 64            |
| Al 6082  | 3, chromed  | 0.092                | 0.546                | 46            |
| Al 6082  | troval, 3   | 0.03                 | 0.221                | <b>78</b>     |

### 2.1.3 Simulation and power budget

An optical simulation of the system is made in FRED [29] to evaluate the possible performance of the prototype. A 3D rendering of the system is shown in Fig. 2.10. The LEDs are simulated accordingly to the specifications given in the datasheet. The sources are set as squared sources with an isotropic emission. An apodization of the power is set on the emission, following the graph of the directivity of the source. The combination of the isotropic emission and the power apodization results in a weighted emission, which reproduces the one given by the graph of the datasheet of Fig. 2.9. The wavelength can also be modeled according to the spectrum of the LED. As the FWHM (full width at half maximum) of the bandwidth of the spectrum is of 10 nm, this does not influence much the results, and a single wavelength is used. The bandwidth of the LED corresponds well to the bandwidth of the i-line filters, which can be found commercially.

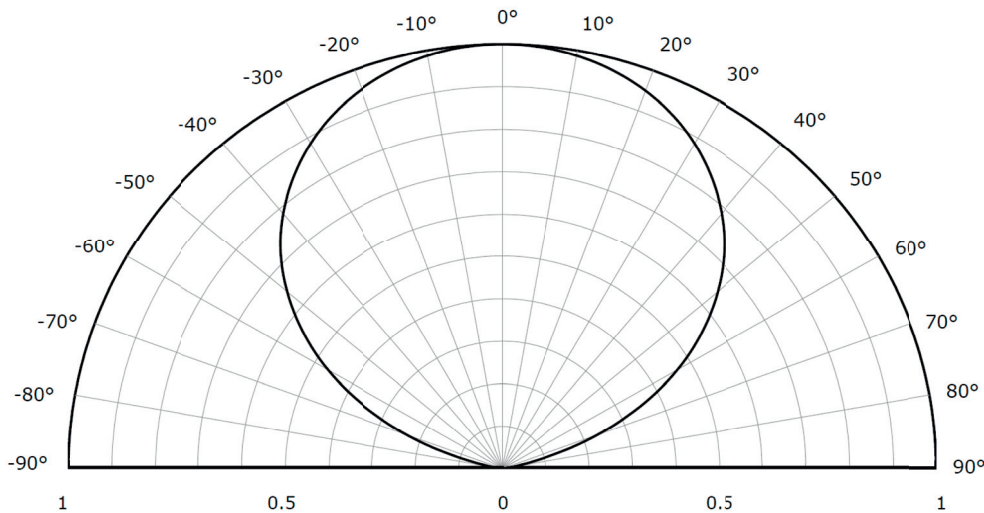


**Figure 2.9** – The graph of the directivity of the LED, from [30]. This gives the power apodization used in the simulation.

The reflectors are built by entering the equations of the parabolic compound concentrator given in Eq. (2.1) to describe the surface. The measured specular reflectance of the polished aluminum samples is used to determine the coating of the reflectors in the simulation. This simulation is used to make sure that the design is correct and that the output angle after the reflectors matches the angular acceptance of the microlens array.

A first estimation of the power efficiency of the reflectors can be done according to the number of reflections that the rays encounter. As the surface of the reflectors have a determined specular reflectance, it limits the best achievable power efficiency for those reflectors. According to the simulation, the source can be separated into rays undergoing 0, 1, 2, 3 and “4 an more” reflections. Examples of different rays are shown in Fig. 2.2, where only 2 dimensions are taken into account. In 3D, the rays can be reflected on multiple surfaces.

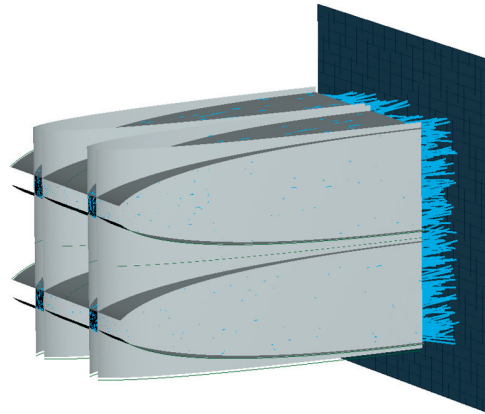


**Figure 2.10** – A 3D rendering of the FRED simulation of the 2x2 LEDs system. The LEDs were simulated thanks to the datasheet provided by the furnisher. The specular reflectance of the aluminum was measured with a laser and set into the simulation.

In Table 2.2, the first column indicates the number of reflections which the rays undergo. The second column is the percentage of the source power it represents. In the case of the LEDs, 3 % of the source power undergo 0 reflections, which corresponds to direct light from the LED, 27 % undergo 1 reflections, etc. Most of the light is reflected 2 times and less. In the case of the 2x2 LEDs system, the measured specular reflectance of a simple polished aluminum sample without coating is about  $66 \pm 5 \%$  at 405 nm. The error is found by repeating the measurement over different polished samples. The third column of the table represents the percentage of the initial source power which makes it to the output of the reflector with a specular reflectance of  $66 \pm 5 \%$ . In total,  $46 \pm 6 \%$  of the initial power reaches the output of the reflector, with most of the power coming from rays undergoing 1 or 2 reflections. The polishing of the surfaces has an important impact. An improvement of the specular reflectance from 66 % to 78 %, increases the maximum theoretical efficiency of the reflectors to 64 %. This is achieved for the 7x7 prototype, for which the best measured specular reflectance of the samples is about 78 % at 405 nm. This measure is subject to important variations, as the samples are hand polished, making it difficult to ensure the exact same quality of polishing over the complete surface of a fan. The reflectance is also be slightly lower with the LEDs at 365 nm as the light is be a bit more absorbed in the metal at this lower wavelength.

This evaluation allows the computation of an estimation of the maximum efficiency achievable with such a system. As presented in Fig. 2.11, the collection efficiency from one LED to the reflector is estimated to be 90 %, without taking into account the losses at the junctions of the fans. The reflectors themselves have an efficiency of maximum 64 % for the best polishing case. With the variations of the polishing quality over the different fans and the losses at the junction of the fans as well as the vignetting occurring in the optical system, the efficiency of the reflectors can be considered to be about 40 %. The rest of the optics, which has anti-reflective coatings, is taken to have a total efficiency of 90 %, taking into account reflection and absorption losses for example. This adds up to an overall optical efficiency of 33 %.

**Chapter 2. High power UV LED illumination system**

*Table 2.2 – Power efficiency with a specular reflectance of 66 % and 78 %*

| Number of reflections | Source power [%] | Source power after 66% refl. [%] | Source power after 78% refl. [%] |
|-----------------------|------------------|----------------------------------|----------------------------------|
| 0                     | 3                | 3                                | 3                                |
| 1                     | 27               | 18                               | 21                               |
| 2                     | 46               | 20                               | 28                               |
| 3                     | 15               | 5                                | 7                                |
| ≥4                    | 9                | 2                                | 5                                |
| <b>total</b>          | <b>100</b>       | <b>46</b>                        | <b>64</b>                        |

For the total system, the electrical to optical power efficiency of the LEDs are given, by the manufacturer, to be about 25 % for the 365 nm LEDs and 40 % at 405 nm. It means that the overall electrical to optical power efficiency of the system is estimated to be respectively 8 % and 13 %, with the current parameters. This is 2-5 times better than the existing optical system with a mercury arc lamp in mask-aligners, which is a significant improvement.

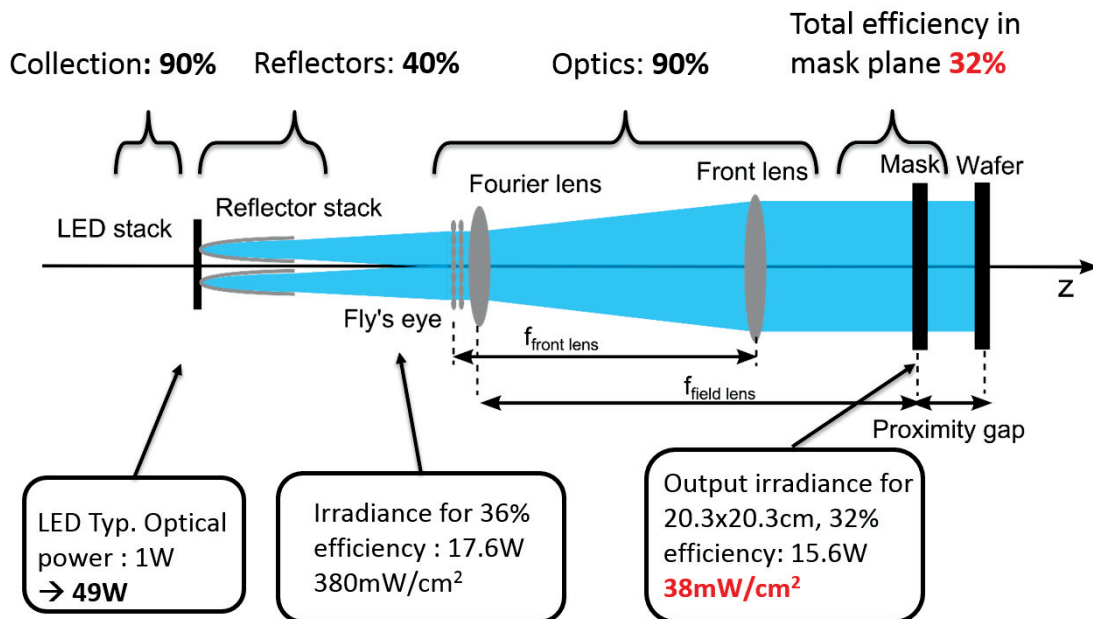


**Figure 2.11** – The power budget for the 7x7 LED illumination system. Overall the optical system has an efficiency of about 30 %.

Table 2.3 illustrates the scalability of an LED module and the obtainable power, based on the precedent calculations. The optical power corresponds to what is given by the datasheet of the LED. The model used has 1.4 W at 405 nm and 1.03 at 365 nm, but for the sake of simplification, 1 W is considered. The power in the mask plane is given by the number of LEDs multiplied



by the power per LED and by 0.3, the overall efficiency of the system. The last column gives the resulting irradiance in the mask plane for an 8 inches by 8 inches ( $20.32 \times 20.32 \text{ cm}^2$ ) illuminated area. For the comparison, a MA-BA8 Gen.3 SUSS mask-aligner which we have in our laboratory gives, with a mercury arc lamp of 350 W electrical power, an irradiance of  $7 \text{ mW/cm}^2$  at 365 nm (with the i-line filter), and  $30 \text{ mW/cm}^2$  in broadband . This means that, in order to compare with such a lamp, a 4x4 module is necessary for 365 nm and a 7x7 module for broadband illumination. For broadband, modules at a different wavelength can also be combined with a dichroic mirror. The advantage of a 7x7 module is that its size corresponds to the size of the fly's eye integrator in the mentioned mask-aligner model. The main challenge when realizing a module of this size is the cooling and the driving of the LEDs. Of course, larger modules could be built to replace higher power mercury arc lamp sources. A 16x16 LEDs module would be enough to produce as much power as a 5 kW mercury lamp at 365 nm. One difficulty for such a large module is also the cooling, which should be carefully designed. Another aspect is that the size of the 16x16 system would be around  $160 \times 160 \text{ mm}^2$ . In a mask-aligner with a 5 kW mercury arc lamp, the size of the microlens array is  $100 \times 100 \text{ mm}^2$ . This means that additional optics should be added to project the irradiance at the output of the reflectors onto the microlens array, at the correct size. This means that the overall system would be less compact. As already mentioned, combining different modules could also be a solution, but it would also result in larger optical systems.

*Table 2.3 – The expected irradiance for LEDs module of different sizes*

| Module size       | Optical power [W] | Power in the mask plane [W] | Irradiance in the mask plane [ $\text{mW/cm}^2$ ] | Lateral dimensions [ $\text{mm}^2$ ] |
|-------------------|-------------------|-----------------------------|---|--------------------------------------|
| <b>1 LED</b>      | 1                 | 0.3                         | 0.7   | 10x10                                |
| <b>2x2 LEDs</b>   | 4                 | 1.2                         | 2.9   | 20x20                                |
| <b>4x4 LEDs</b>   | 16                | 4.8                         | 11.6  | 40x40                                |
| <b>7x7 LEDs</b>   | 49                | 14.7                        | 35.6  | 70x70                                |
| <b>16x16 LEDs</b> | 256               | 76.8                        | 186   | 160x160                              |

#### 2.1.4 Fabrication tolerances

A very important aspect of the design is evaluating the possible different misalignments of the system and providing tolerances which are realistic and still allow to reach the desired performance. In the assembly, the part which is the most subject to misalignments is the LED positioning on the PCB. The LEDs can be shifted in both x-y plane, i.e. in a parallel direction to the PCB and in the propagation direction z, because of the soldering and because of the position of the LED surface with respect to the entrance plane of the reflector. The LEDs are soldered by re-flow by the company making the PCB. The tolerances are given as 0.1 mm in x, y direction and are measured to have a maximum of 0.1 mm in z direction. Based on the simulation, the effects of the different misalignments can be easily represented and quantified.

## Chapter 2. High power UV LED illumination system

---

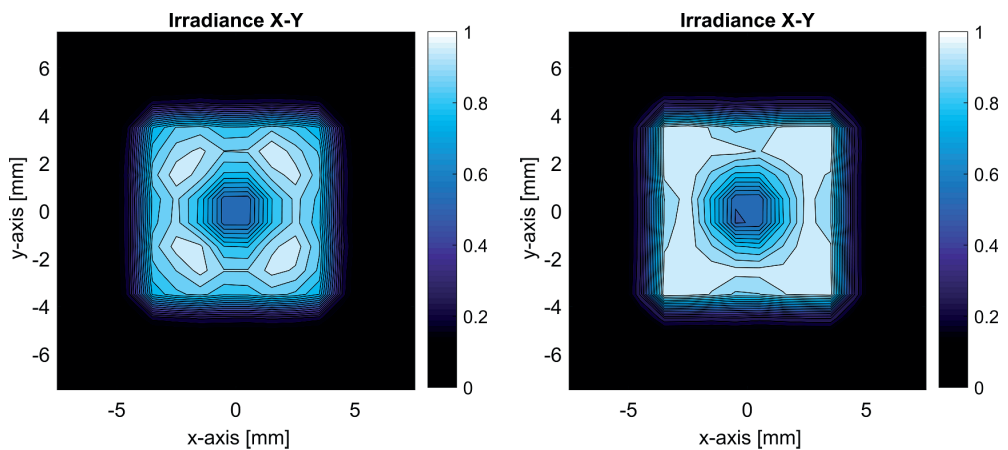
The misalignments mainly affect the irradiance and intensity at the output of the reflectors, as well as the collection efficiency of the reflectors.

In Fig. 2.12 the effect of the displacements are shown on the irradiance for both longitudinal and lateral displacements. The irradiance is affected, because as the LED die moves to one side, more light is brought to one side of the output of the reflector, but as long as the die stays within the entrance of the reflector, there is no loss of light. The irradiance distribution varies as well when the source is displaced along the propagation axis. In this case, this change of irradiance pattern is not very critical for the uniformity in the mask plane, as the fly's eye integrator has lenses of about 300  $\mu\text{m}$ . This means that each reflector, with an output size of 10 mm, illuminates more than 1000 microlenses. The variations over the irradiance at the output of the reflectors is therefore well compensated for by the mixing of the fly's eye integrator and does not impact the uniformity in the mask plane of the mask-aligner. The angular distribution in the mask plane, on the other hand, will be affected. One reflector, in the center, corresponds to an angular extent of 0.8  $^\circ$  in the mask plane. This means that variations in the irradiance of a the output of the reflector influences the angular distribution in the mask plane over a similar angular range. Once again, the impact on the quality of the prints requires simulations and print tests.

In Fig. 2.13, the effect of the displacements along the propagation direction  $z$  and in the  $x$ - $y$  plane on the intensity is shown. In both case, the angular extent is smaller than 10 $^\circ$ , which is the acceptance angle of the microlenses which follow the reflectors. The lateral displacement does not have a noticeable effect on the angular distribution. The  $z$  displacement changes the angular distribution slightly, but the angular extent remains the same. For the same reason as for the irradiance, the overall change of intensity over one reflector has little impact on the performance. The local angular distribution across one channel of the microlens is important, as it impacts the final uniformity of the irradiance in the mask plane. Once again, the fact that the microlenses are very small ensures that a good homogeneity is preserved. Furthermore, the compound parabolic concentrator shows a good homogeneity of the local angular distribution across its output plane, as shown by Fournier and Rolland in [14].

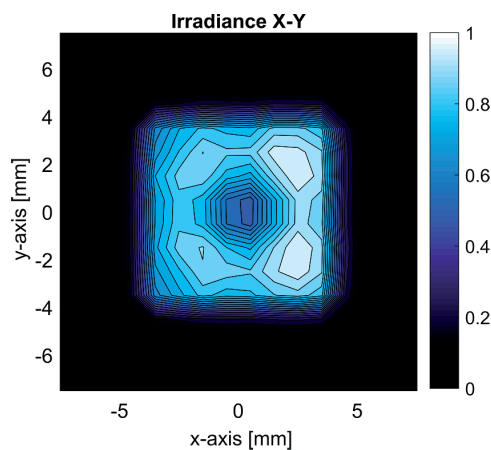
Regarding the collection efficiency, the entrance dimensions of the reflector are 1.5 mm x 1.5 mm and the emitting die of the LED is about 1.2 mm x 1.2 mm. This means that there is room for a displacement of 0.15 mm on each side of the LED without losing any light. For larger displacements, the fraction of light emitted by the die, which is not in the reflector entrance anymore, is lost. In our case, the tolerances given by the company making the PCB is small enough to ensure that no light is lost due to the lateral displacements. The longitudinal displacement of the LED also have an impact on the collection efficiency. When the die is displaced behind the entrance of the reflectors, all the light which has an angle larger than the one formed between the border of the die and the edge of the entrance of the reflector is lost. A graph presenting the collection efficiency as a function of  $z$ -displacement is shown in Fig. 2.14. The effect is quite important as for 0.1 mm of displacement, about 5 % of light is not collected anymore. Overall, the most critical tolerance on the positioning of the LED is on its

position along the direction of propagation, as it affects greatly the collection efficiency of the reflectors. As long as the tolerances ensure a positioning of the LED of 0.1 mm and below in every direction, the impact on the irradiance, intensity and collection efficiency is acceptable. This is the case for the standard tolerances on the LED positioning given by the company. Requiring a non-standard positioning of the LED can quickly become much more expensive.



(a) The simulated irradiance for the LED at nominal position

(b) The simulated irradiance with the LED 0.1mm behind the nominal position



(c) The simulated irradiance with 0.1mm of lateral displacement of the LED.

**Figure 2.12** – The simulated irradiance for displacements of the LED with respect to its nominal position. The irradiance pattern changes only in a limited manner with displacements within the tolerances given by the company mounting them. The contour lines are set every 5 %.

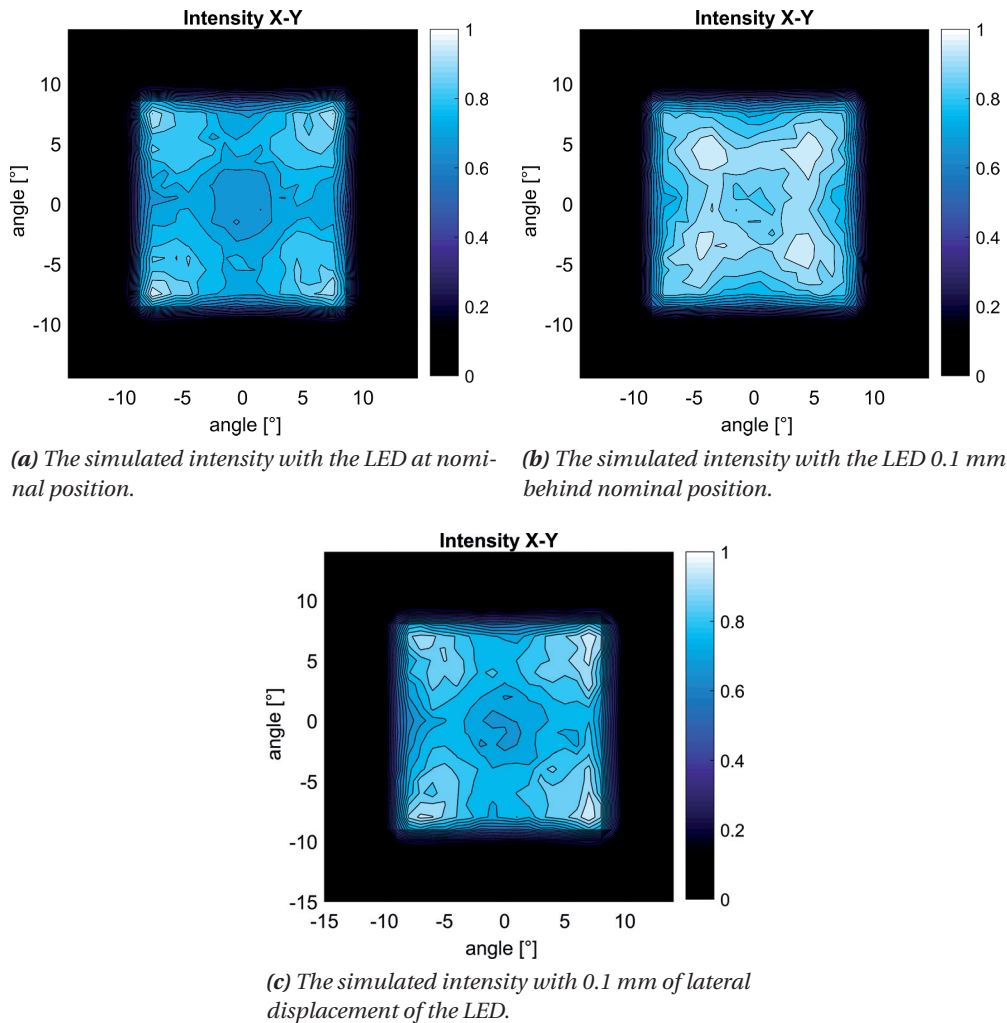


**Figure 2.13** – The simulated intensity for displacements of the LED with respect to its nominal position. The intensity pattern changes only in a limited manner with displacements within the tolerances given by the company mounting them. The contour lines are set every 5 %.

The mechanical pieces themselves present another kind of tolerances. In this case, the critical point is to make sure that the fans can be mounted together, with as little space as possible between the mechanical parts. Limiting the space between the mechanical parts ensures a maximum fill factor and avoids losses at the junctions between the pieces. The process which has the greatest tolerances is the polishing. It is done by hand, and is therefore more subject to fluctuations. The fans are machined with a CNC machine (computer numerical control machine) at the correct dimensions and a few tens of microns are taken off by the polishing, which ensures that the pieces can be mounted together. In the end, there is still some play in between parts. This is shown in Fig. 2.15, where a picture of the emitting 7x7 module is overexposed to make the leakage apparent. The design has some advantages in that regard. The corners are made in such a way that mainly one direction is leaking, as shown by the

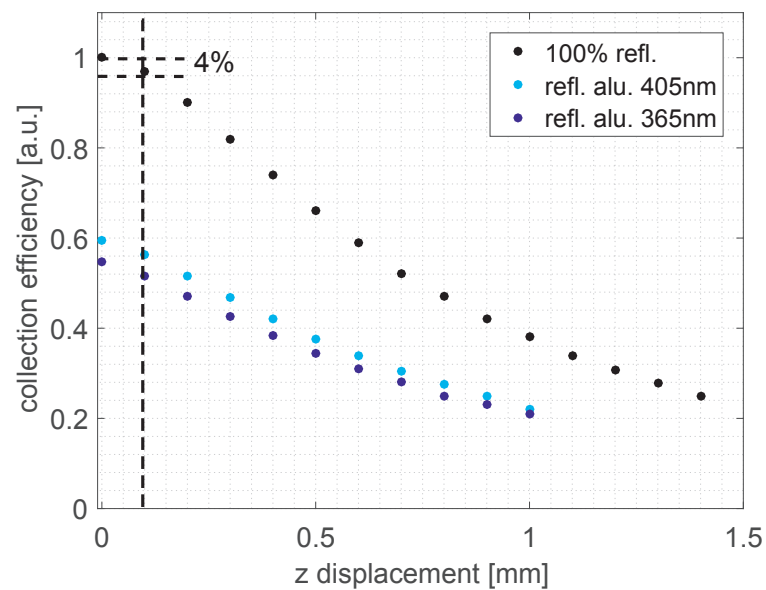


**Figure 2.14** – The evolution of the collection efficiency as a function of LED displacements in  $z$ . The efficiency drops quite quickly. The dashed line represents the actual tolerances on the positioning of the LEDs for the prototype. For 0.1 mm of misalignment, the maximum collection efficiency drops to 96 %.

red arrows on Fig. 2.16. If the pieces were mounted edge to edge, two directions would be leaking in case of play between the parts. This is confirmed by the picture, where only one direction is leaking. Another advantage is the fact that it is an array. It can be seen that the light that is leaking towards the other channels lights up the neighboring channel and thus is not necessarily completely lost.

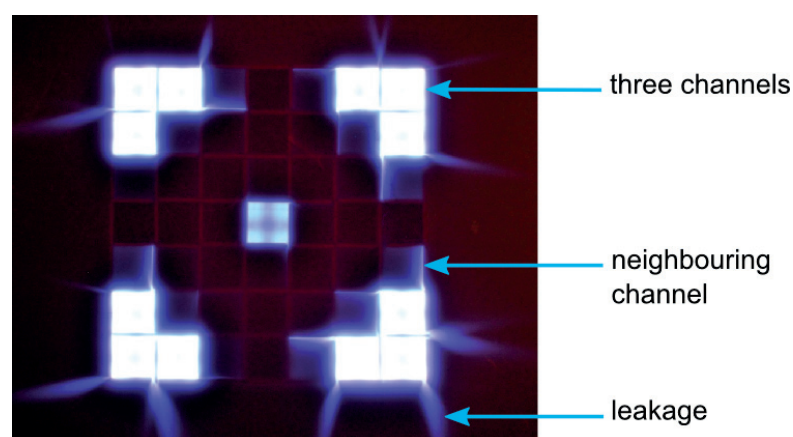


**Figure 2.15** – A picture of the irradiance distribution at the output of the reflectors. Notice the leaking pattern at the corners. The light goes only in one direction due to the mechanical design. Part of the light which leaks to a neighboring channel lits up this channel and thus is not lost.

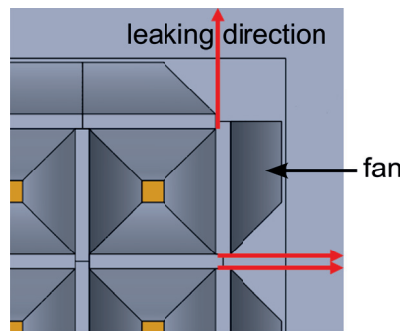


**Figure 2.16** – A detail view of the SOLIDWORKS model of the corners of the reflectors. The red arrows indicate where the light can leak. The light goes only in one direction due to the mechanical design.

From the power measurement and the tolerance analysis, the leakage and the positioning errors of the LEDs are estimated to contribute to about 20 % of the losses. The displacement in the z-direction being lower or equal to 0.1 mm, this means that both collection and leakage have losses of about 0.1 % each. The reflectors having a total efficiency of maximum 64 % with the best polishing, most of the losses therefore happen due to the absorption of the light into the aluminum of the reflector or as stray light. Those losses due to the reflectivity of the surfaces represent a drop of efficiency of about 36 %. This is much more than the 20 % of the losses due to the positioning errors. Therefore, in order to increase the total efficiency of the system, the reflective surfaces of the reflectors is the most critical aspect to work on. The state of surface can probably be improved, by using another tool for the machining. Some reflective coatings could also be applied, but due to the shape of the fans, it might be complicated to ensure a uniform layer. In order to reduce the leakage losses, the tolerances on the fabrication can be made tighter. Replacing the hand polishing step by an automatized polishing step could ensure a better control over the final dimensions of the fans. In the end, it is also a matter of costs, as implementing the suggested ameliorations increases the manufacturing complexity and time and therefore the costs.

### 2.1.5 Electrical and thermal management design

The 7x7 prototype requires a rather complex electrical design, with the building of a complete controller. This part was done by a Marcel Groccia, a colleague, and is only described shortly in order to give an idea to the reader of the main parts and components.

The main challenges faced are the implementation of the cooling system and the wiring and the driving of the LEDs. The goal is to be able to have a variable illumination, with different patterns. Ideally, to have the highest level of versatility, each LED should be driven independently. This is not put into practice for the first prototype, as the wiring is too complicated due to the fact that the space available on the PCB is limited. Instead, four groups of LEDs wired in series were designed. The different layouts of the groups are shown in Fig. 2.17, each group

being represented by one color. The groups can also be switched on together, meaning that there are 15 of possible illumination patterns.

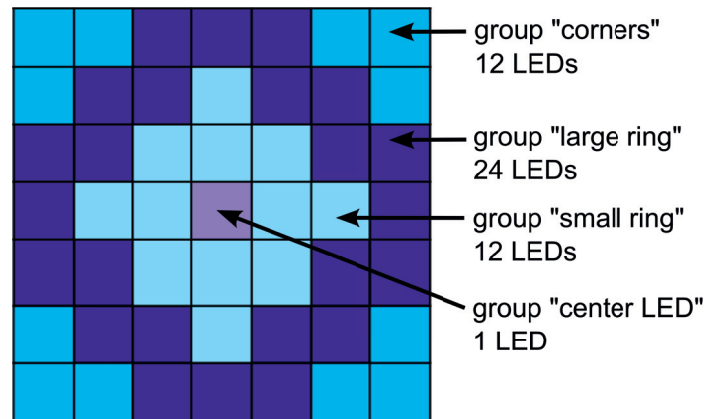


**Figure 2.17** – The different groups of LEDs. Each color is a group of LED wired in series. They can be switched on independently or together, meaning that 15 different illumination patterns can be created.

The entire driving system is shown in Fig. 2.18, where the blue boxes are the hardware parts and the black arrows give the relations and the functions between them. The main control of the system is done using an Arduino microprocessor. It controls three mother boards with the LED drivers. The signal emitted by the Arduino is a pulse width modulation (PWM) at 1kHz. This makes it possible to change the average output intensity of the LEDs by changing the duty cycle of the PWM. This is done by the user with the help of a varistor. An external trigger is also set, to be able to give impulsions from a signal generator of the required exposure time. Concerning the cooling system, a commercial water cooling system for computers is used, as already explained in the mechanical design in section 2.1.2. The LEDs are driven at their maximum current, according to the datasheet, which is 1400 mA. This corresponds to a forward voltage of about 3.8 V and an optical power of about 1.4 W. The cooling system should therefore be dimensioned to dissipate about 4 W per LED. For the 7x7 system this means about 200 W to dissipate for the whole system. The cooling blocks mounted on the PCB ensure the energy flow between the PCB and the water pipes; they are shown in Fig. 2.19. The water is then cooled by fans. The Arduino controls three different parameters: the water flow to make sure it is sufficient; the temperature on the PCB to make sure it is low enough; the current in the fan cooling the driver to make sure the fan is functioning properly.

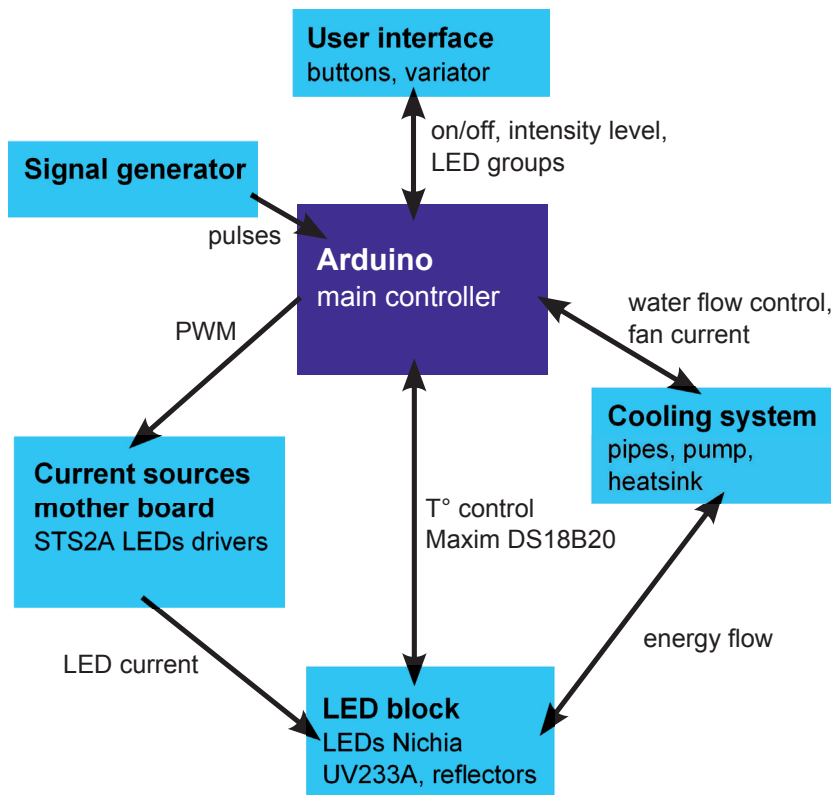


**Figure 2.18** – A schematic of the driving electronics used for the 7x7 LED system with the electronics. The blue boxes represent the hardware parts and the black arrow the functions between them.

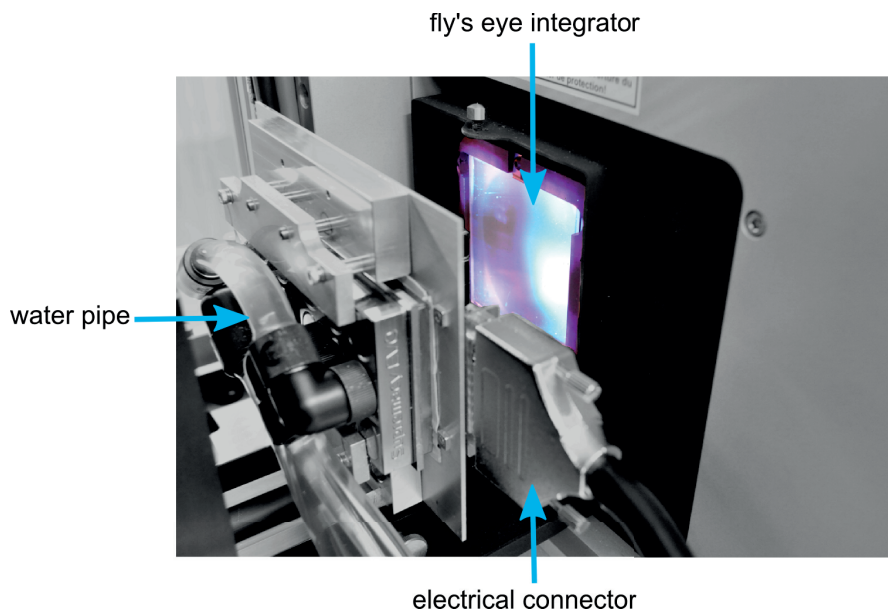


**Figure 2.19** – A photograph of the 7x7 LEDs and reflector system. The cooling blocks are visible with the water pipes. The large connector is linked to the main controller unit.



## 2.2 Characterization of the performance of the prototype

The characterization process consists of four main steps which are presented in the corresponding sections. The characterization of the irradiance and the angular distribution after the reflector and a fly's eye integrator are determined in the first section. This is done with the 2x2 LEDs system, because it is smaller and therefore more practical to measure. As the design is the same for the 7x7 LEDs system, the characterization done on the 2x2 system is also valid. In the second section, the power efficiency and stability are evaluated. The performance of the reflector illumination system is then validated with the rest of the optical system of a mask-aligner in the third section. This is done for both the 2x2 and the 7x7 LEDs systems. In the fourth section, the results of irradiance homogeneity measurements and print tests are presented to compare the performance of the prototype in the machine with those of a mercury arc lamp. For all the homogeneity measurements, the uniformity is defined as the contrast of the resulting light field, and is calculated using the following equation:

$$U = \frac{I_{max} - I_{min}}{I_{max} + I_{min}} \quad (2.4)$$

### 2.2.1 Optical characterization

The optical characterization consists in measuring the irradiance and intensity distributions after the reflectors and the fly's eye integrator. In order to do so, two types of scanning setups are used. They are shown schematically in Fig. 2.20. The scanners are controlled using Labview. An aperture is placed in front of the photodiode to increase the resolution of the scans. The linear motors have a resolution of 1  $\mu\text{m}$  in full step and the angular motors have a resolution of 0.1  $^\circ$ . It is the aperture size in front of the photodiode which determines the resolution of the measurement. Depending of the sensitivity of the photodiode used, a pinhole down to the size of 200  $\mu\text{m}$  can be used for very finely sampled measurements. For most of the characterization, though, a large surface has to be scanned and therefore an aperture with a size of 1 mm is chosen to reduce the scanning time.

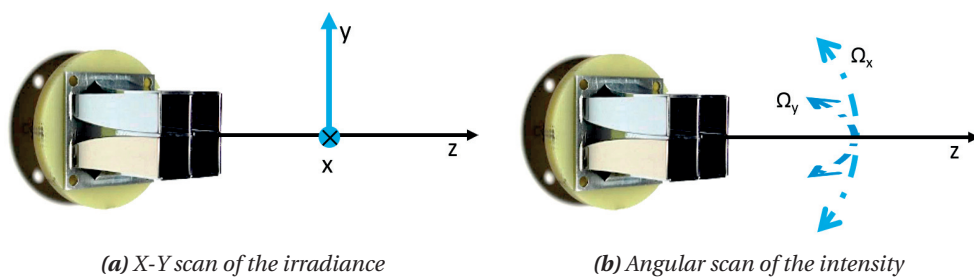


**Figure 2.20** – Schematics of the measurement of the irradiance and intensity at the output of the reflectors.

## Chapter 2. High power UV LED illumination system

The response of the photodiode is first characterized, to check its linearity and to make sure that is enough to measure variations of irradiance of a few percents. A light source is placed far away from the detector. A measurement is made with the photodiode, which gives a voltage. The measurement at the same place is repeated with a Thorlabs power meter, which gives the corresponding power in Watt. The power is normalized to make the curve independent of the wavelength. The sensitivity of the photodiode varies with the wavelength, with the deeper UV range exhibiting a lower sensitivity. The results are shown in Fig. 2.21. It is evident, from the graph, that the linearity of the photodiode is very good and that it will be enough to measure variations of irradiance of a few percents.

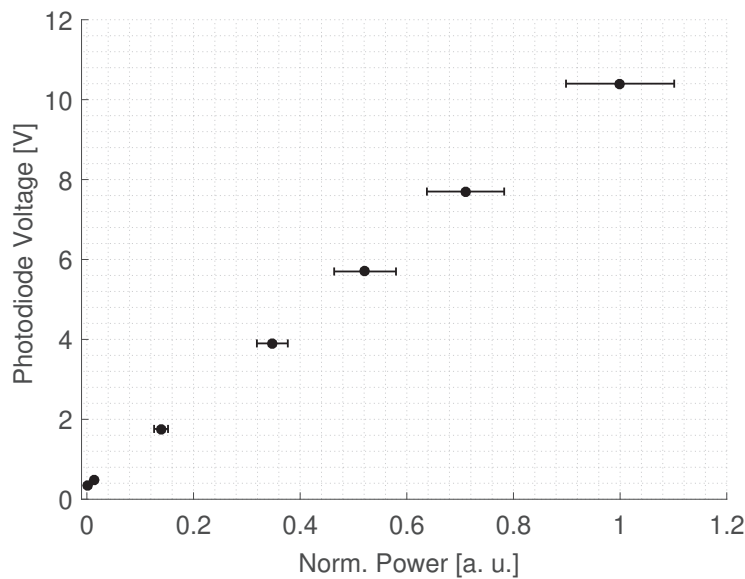


**Figure 2.21** – The measurement of the linearity of the photodiode. The power is normalized. For different wavelengths, the sensitivity of the photodiode varies.

For the irradiance measurement, a photodiode is mounted on two linear stages, as illustrated in the photograph of Fig. 2.22.

A similar setup is used for the angular characterization but the photodiode is mounted on two rotational scanners, as shown in Fig. 2.20(b). This forms a goniometer and the source is placed in the center of the rotation axes. Angular steps of 0.5 degree are made to acquire the whole angular distribution. Once again, the resolution of the measurement is determined by the aperture placed on the photodiode. This setup allows the measurement of the homogeneity level of the intensity distribution achieved by the different components.

The measured irradiance at the output of the reflectors is shown in Fig. 2.24(a). It corresponds to what is expected from the simulation presented in section 2.1.4. Based on the simulation and according to the evaluation of the tolerances made previously, the LED seems to be behind the nominal position, as the pattern looks similar to the one in Fig. 2.13(b). The displacement in  $z$  is probably slightly smaller than 0.1 mm. This means that the theoretical collection

## 2.2. Characterization of the performance of the prototype

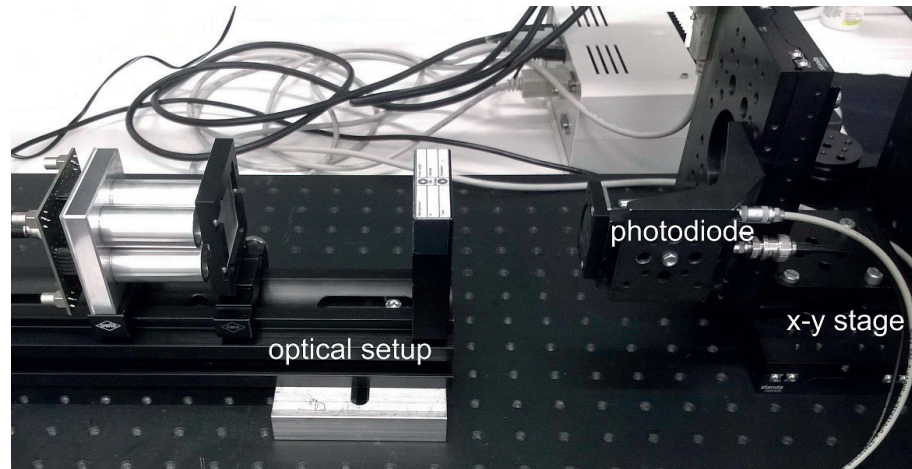


**Figure 2.22** – A picture of the setup used for the measurements of the irradiance at the output of the reflectors.

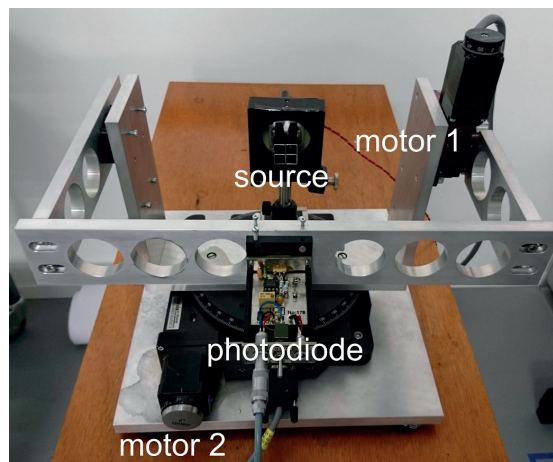


**Figure 2.23** – A picture of the setup used for the measurements of the intensity at the output of the reflectors.

efficiency for this LED, is about 96%. There is, probably, also a small lateral displacement in the y-direction, as there is more intensity in the upper part of the image. Figure 2.24(b) shows the angular distribution at the output of a single reflector. The levels on the image are set every 5%. The reflectors show an angular homogeneity within  $\pm 5\%$  for the part of the irradiance within  $\pm 7^\circ$ . This is because the edges of the pattern are not very sharp. The transition from no intensity to a homogeneous level is made over a few degrees. In the end, the most important part is that most of the light is collimated within  $\pm 10^\circ$ , which corresponds to the angular acceptance of the microlens array, which come after in the optical design of the mask-aligner.

A scan of the 2x2 system is also done and is shown in Fig. 2.25. It can be observed that not all the reflectors show the same irradiance distribution. This is due to the fact that the LEDs are always positioned slightly differently within the given tolerances. As the reflectors are

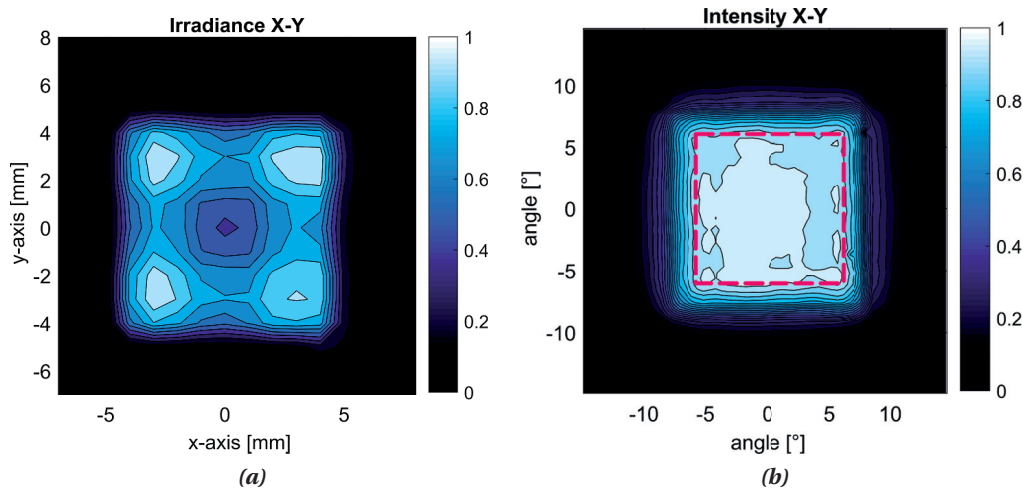


**Figure 2.24** – The measurement of the irradiance and intensity at in the output plane of one reflector. The contour lines are set every 5%. (a) the irradiance distribution, (b) the intensity. The angles are contained within  $\pm 10^\circ$ . The uniformity of the intensity is within  $\pm 5\%$  for angles within  $\pm 7^\circ$ .

followed by the microlens array, it doesn't impact the quality of the irradiance uniformity in the mask plane. The only impact is on the homogeneity of the intensity, as the irradiance on the microlens array are transformed into the intensity in the mask plane. Advanced simulations of the structure and its aerial images should be done with varying intensity distribution in order to determine precisely the effect of the difference of angular spectrum on the quality of the prints. The pattern on the microlens array also depends on its distance from the output of the reflectors. A better uniformity can be found when increasing the distance, but at the cost of more losses, if the resulting light field is larger than the following optics.

The intensity distribution after the four reflectors and the fly's eye integrator is shown in Fig. 2.26. The angles are within  $\pm 10^\circ$  at full width half maximum. The uniformity is within  $\pm 5\%$  for angles within  $\pm 9^\circ$ . It is the same intensity uniformity as with the reflector. The difference is that the angular extent over which it is achieved is much larger than with the reflector. This is because the edges of the pattern are much sharper, which means that there is a sharp transition between the part where there is no intensity and the part where the intensity is uniform. The uniformity is thus better than after the reflectors alone. This uniformity level corresponds to what is given in the datasheet of this element. This intensity distribution is then transformed into an irradiance distribution in the mask plane by the Fourier lens. We can see that there is more intensity in the small angles and it decreases towards larger angles. When installing such devices in a mask-aligner, these kind of non-uniformities are partially compensated by the field lens which follows, and allows to reach the specified  $\pm 2.5\%$  of homogeneity.

## 2.2. Characterization of the performance of the prototype

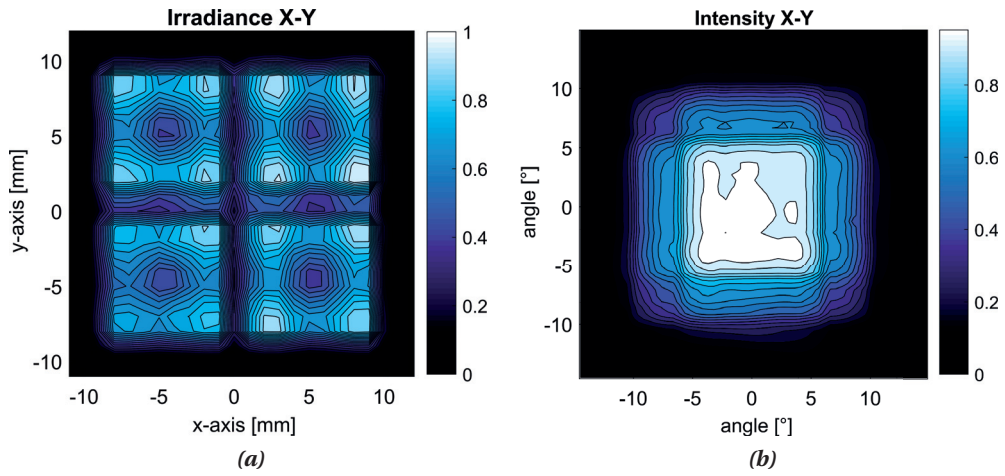


**Figure 2.25** – Measurements of the irradiance and intensity after four reflectors. (a) The irradiance distribution. The contour lines are set every 5%. (b) The intensity. The measurement system did not allow for a precise measurement of the intensity as the arm of the goniometer is too small for the source to be considered a point source. Notice that the angles do not superpose well on the edge.

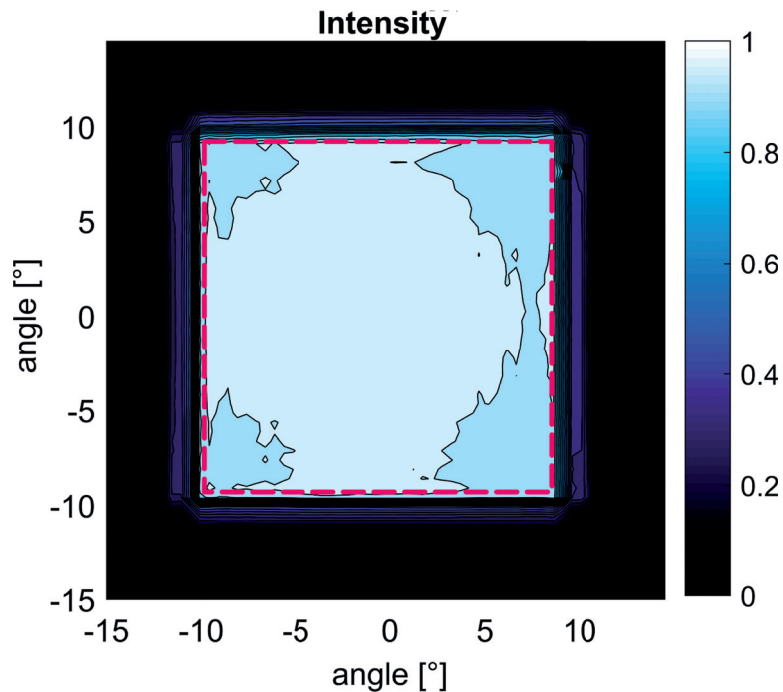


**Figure 2.26** – The measurement of the intensity distribution after the four reflectors and the fly's eye integrator. The contour lines are set every 5%. The angular extent is  $\pm 10^\circ$  and the uniformity is within  $\pm 5\%$  for angles within  $\pm 9^\circ$ .

### 2.2.2 Power efficiency and stability

In order to measure the performance under real conditions, the 7x7 LEDs prototype is mounted in a MA/BA8 Gen3 SUSS mask-aligner. The 2x2 prototype cannot be driven at the maximum power, because it does not include a heatsink. The measurement of the irradiance level in the mask plane is, in that case, not relevant.

The 7x7 LEDs system at 365 nm mounted in the machine and driven close to its maximum power shows an irradiance, in the mask plane, of 31 mW/cm<sup>2</sup> over an area of 20.3 x 20.3 cm<sup>2</sup>. This is more than four times the irradiance at 365 nm with the mercury arc lamp of 350 W. It is actually as much as the 350 W lamp in broadband. The results are summarized in Table 2.4. The result corresponds quite well to the provisions of the power budget, with an overall efficiency at 365 nm of 5 %, against the 7-8 % estimated. The mercury arc lamps typically have efficiencies at 365 nm of 0.5-1.25 %. The fact that the LEDs can be switched on and off easily increases even more the effective efficiency. Depending on the duty cycle of the exposure process, the LEDs can be switched off during a part of the process. This is a time during which the system does not consume energy. The mercury lamp, on the contrary, is always switched on and the energy spent during the handling time, when the shutter is closed, decreases the effective overall efficiency. For a typical exposition in proximity printing and without alignment, the exposure time represents 20% of the process time per wafer. This means that the effective efficiency of an LED based system compared to a mercury arc lamp system can be improved by a factor of 5, just with the duty cycle.

*Table 2.4 – Summary of the irradiance level measurements*

| Light source    | Wavelength      | Irradiance [mW/cm <sup>2</sup> ] |
|-----------------|-----------------|----------------------------------|
| 350W Lamp       | broadband       | 29                               |
| 350W Lamp       | i-line (365 nm) | 7                                |
| 7x7 LEDs module | 365 nm          | 31                               |

The stability of the power or irradiance in the mask plane is also measured. The impulses of a few seconds are generated with a signal generator. The power is measured with a Thorlabs power meter, at a frequency of 3 Hz. As explained in the section 2.1.5, the LEDs are actually pulsed at a high frequency by the PWM (pulse width modulation) of the main controller (Arduino). This means that the measured signal is an average of the emitted signal. The measured value is divided by the surface of the power meter to get the irradiance. There are different important aspects to this measurement. The irradiance level should be the same over different pulses and the form of the pulses should be repeatable. Another aspect is the switching time. When printing, dose tests are made to determine the dose needed for a certain type of patterns and a specific resist. Thanks to the measured irradiance, it is then possible to compute the exposure time needed to reach the determined dose. The switching time should therefore be low so that the measured intensity, when the light is stabilized, corresponds to reality.

## 2.2. Characterization of the performance of the prototype

The result is shown in Fig. 2.27. It can be seen that the pulses are all very similar, which indicates a good repeatability. The power meter head is not quite fast enough to sample completely the rising and falling time of the pulses, which means that they are below 0.3 s. The variation on the duration of the pulses is below 10 ms. There is a slight overshoot of about 1.5 % at the beginning of the pulses. The possible explanations for this overshoot are the following: all the LEDs do overshoot when the pulse start; the measurement head produces a fake overshooting; some of the LEDs are overshooting at the beginning of the pulses. The same measurement is repeated for the different patterns of the LEDs. A small overshoot is always measured. This indicates that it is probably indeed the LEDs which are overshooting. This overshoot effect is stronger when measuring the central LED alone, which presents an overshooting of 4.3 %. On this prototype, the central LED seems less efficiently cooled than the others. As the cooling elements are in two parts, there is a space between them right where the central LED is, which could explain this problem. However, this particular LED showed other weaknesses (less bright and sometimes blinking) which can be due to some problems in the PCB. Concerning the possibility of the power meter head producing the overshoot, it was unfortunately impossible to verify the measurement with another tool, even though this was attempted with a photodiode. The photodiodes available at our facilities do not have an adequate operating frequency.

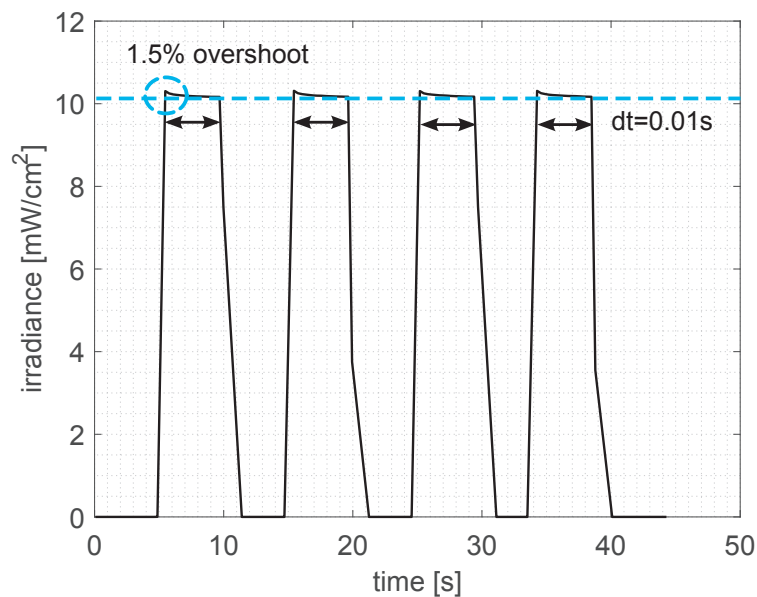


**Figure 2.27** – The measurement of the irradiance stability in the mask plane. The impulsions were generated with the signal generator. There is a slight overshoot at the beginning of the pulses.

Overall, the fact that the pulses are very well repeated is the most important aspect, as different exposures of the same set time will lead to the same amount of light reaching the substrate. One also has to keep in mind that the exposure in mask-aligners with mercury arc lamps is currently controlled with a mechanical shutter. With such a system, the switching time is not

very fast and the pulses width not perfect either. The advantage with the LEDs is that they are switched on simultaneously.

### 2.2.3 Angular spectrum and irradiance uniformity in the mask plane

For the angular spectrum characterization and the irradiance uniformity measurement, the different prototypes are mounted in a MA/BA8 Gen3 SUSS mask-aligner. The 2x2 system is placed such that the output of the reflectors is at a distance of 20 mm from the fly's eye integrator. In the case of the 7x7 system, for mechanical reasons, the output of the reflectors is at a distance of 41 mm. The setup is shown schematically in the Chap.1 , Fig. 1.7. The 7x7 LEDs system mounted in the machine is shown in Fig. 2.28. The system is easily mounted in the existing machine, thanks to the accurate design.

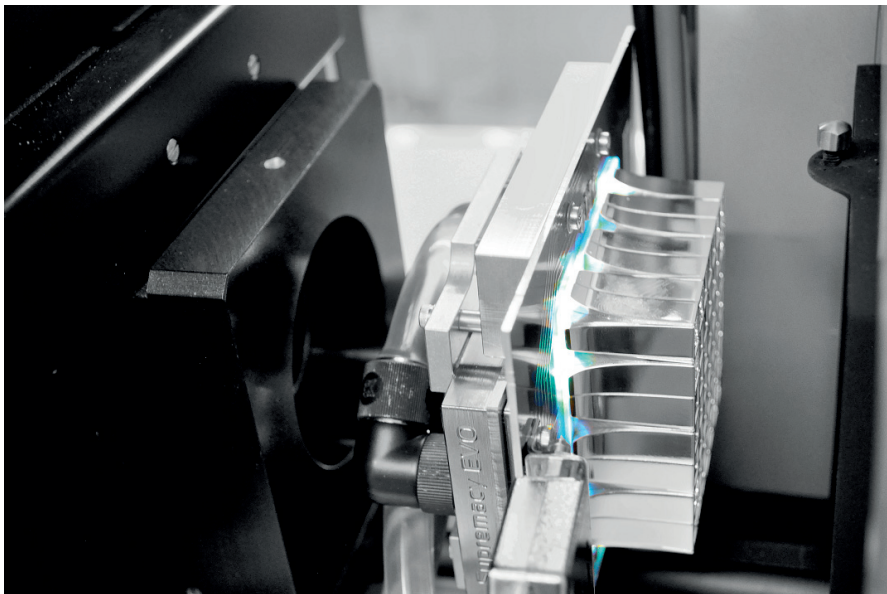


*Figure 2.28 – A photograph of the 7x7 LEDs and reflector system mounted in the machine.*

As the 7x7 LEDs system is mounted with the output of the reflectors 41 mm away from the microlens array, the patterns formed on the fly's eye integrator are different from the irradiance measurements shown with the 2x2 system. The light arriving on the microlens array from the four groups of LEDs are shown in Fig. 2.29. The dashed white line represent the edge of the microlens array, which has a size of 80 x 80 mm<sup>2</sup>. The measurement of such a large field is done by propagating the light from the reflectors to a screen and imaging the resulting light field with a camera mounted with a 18-55 mm objective. The results are subject to the influence of the screen and the aberrations of the camera, but scanning the area with the photodiode setup is not possible, as the range of the motors is not sufficient. The pattern is actually more uniform than directly at the output of the reflectors, which is a good thing, as it is transformed into the angular distribution in the mask-plane.



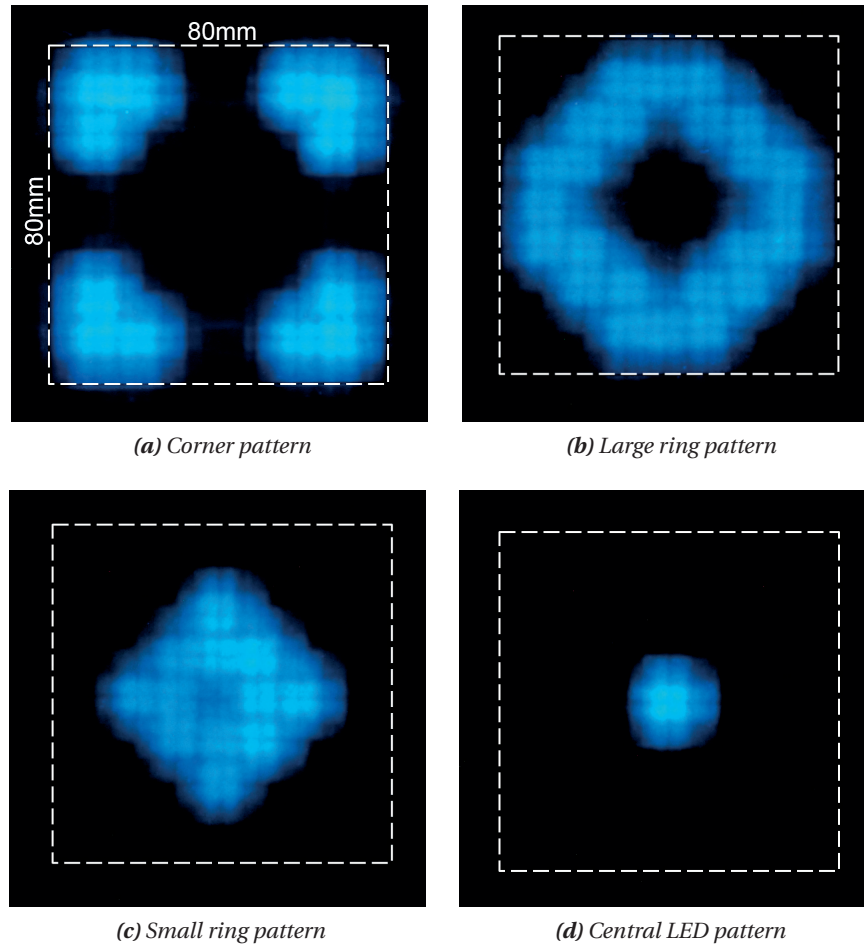


**Figure 2.29** – A picture of the patterns that can be created with the different groups of LEDs, as they are when reaching the fly's eye integrator. The patterns can be combined together. The dashed line indicates the size of the fly's eye integrator,  $80 \times 80 \text{ mm}^2$ .

### Angular spectrum in the mask-plane

The angular spectrum in the mask plane of the mask-aligner, obtained when using the 7x7 LEDs illumination system, is imaged with a pinhole and a camera. A full description of the measurement apparatus is done in Chap. 3. The angular spectrum of the mask-aligner is also measured, for comparison. The photographs are shown in Fig. 2.30. As expected, the angular distributions are very different for the two systems. The angular distribution with the mercury arc lamp is mostly very uniform, where as the one with the LED system is not. This is probably the major drawback of the current prototype. There are different aspects to notice. First, the current driver does not indicate the current level going through the groups of LED. It is therefore difficult to adjust the different group at the same intensity. This is visible in the photograph of Fig. 2.30(a), where the “small ring” pattern is clearly brighter than the others. It is also evident that this particular pattern has some LEDs shining brighter

than the others. These two problems can be solved by improving the driving system. Going to individually driven LED would also be beneficial as this would allow to adjust each LED independently. Concerning the remaining non-uniformities, they are due to the reflectors. It is maybe possible to improve the uniformity, for example with individual lenses as in the publication from Fournier and Rolland [14], but this would probably lead to changes in the output angles, which could end up not matching the acceptance angle of the microlens array. Another solution is to adapt the curve of the reflector to specifically match the emissivity distribution of the LED and homogenize better the irradiance. The fact that the reflectors are made of four fans has the advantage that the surface can be machined in various shapes, as long as the variations are within the capabilities of the radius of curvature of the tool. In any case, these kind of developments require simulations with optimization routines.

Of course, the angular spectrum in the mask plane can be made uniform by adding a lens after the reflectors. By putting the fly's eye integrator in its focal plane, the uniform intensity distribution of the reflectors can be changed into a uniform irradiance. This would result in a performance close to the current system, but the variable illumination pattern function would be lost.

In the end, if the LEDs emits the same intensity, but still produce some kind of non-uniformities in the angular spectrum in the mask plane, it is difficult to judge the impact of the remaining variations on the quality of the prints. Further simulations of the resulting aerial images and print tests need to be done, in order to determine to which point this is a limitation.

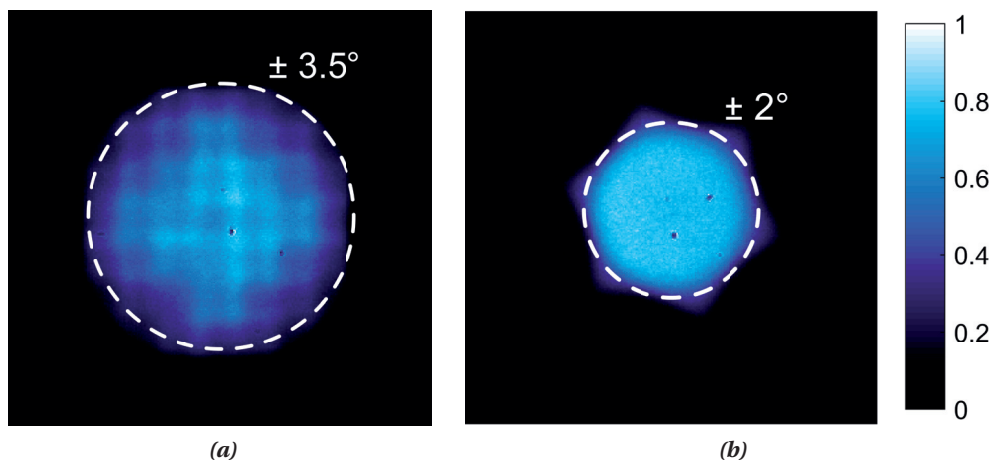


**Figure 2.30** – Pictures of the angular spectrum in the mask plane with (a) the 7x7 LEDs illumination system (b) the mercury arc lamp illumination system.

### Uniformity of the irradiance in the mask plane

A verification of the irradiance uniformity, respecting the standard procedure has to be done. To do so, a calibrated “intensity-meter” from SUSS MicroTec (which actually measures the

## 2.2. Characterization of the performance of the prototype

irradiance) is used in the mask plane to measure the irradiance at different points of the illuminated area. The measurement points are taken according to the positions indicated in the image of Fig. 2.31. The uniformity is then computed as a contrast, according to Eq. (2.4). A reference value is first measured with the mercury arc lamp over thirteen points over an 8 inches (20.3 cm) diameter surface. Different configurations are then measured and the results are presented in Table 2.5. For the mask-aligner in broadband mode, the uniformity is of  $\pm 2.5 \pm 0.5\%$ . This value corresponds to the specifications given by the company. When adding the i-line filter, the uniformity decreases to  $\pm 2.9 \pm 1\%$ . The same measurement is done with both the 2x2 and the 7x7 LED modules. The 2x2 LED module gives a uniformity of  $\pm 2.6 \pm 0.2\%$ . When going to the 7x7 LEDs system, the uniformity improves to below  $\pm 2\%$ . The measurement with all the LEDs turned on is illustrated in Fig. 2.31. The purple spot indicates the point with the highest irradiance, and the blue spots the ones with the lowest irradiance. This measurement gives the best uniformity. This can be explained by the fact that they are the most channels of the fly's eye integrator which are illuminated, meaning more superposition of the light. There are also more different light sources, which increase the mixing of light.

*Table 2.5 – Summary of the uniformity measurements*

| Light source           | Wavelength<br>[mW/cm <sup>2</sup> ] | Uniformity [%] |
|------------------------|-------------------------------------|----------------|
| <b>350W Lamp</b>       | broadband                           | $2.5 \pm 0.5$  |
| <b>350W Lamp</b>       | i-line (365 nm)                     | $2.9 \pm 1$    |
| <b>2x2 LEDs module</b> | 400 nm                              | $2.6 \pm 0.2$  |
| <b>7x7 LEDs module</b> | 365 nm                              | $1.2 \pm 0.2$  |
| <b>corners</b>         | 365 nm                              | $1.7 \pm 0.2$  |
| <b>large ring</b>      | 365 nm                              | $1.3 \pm 0.2$  |
| <b>small ring</b>      | 365 nm                              | $1.4 \pm 0.2$  |
| <b>center LED</b>      | 365 nm                              | $2 \pm 0.7$    |

The distribution of the spots with the highest and the lowest levels of irradiance are given for the different patterns in Fig. 2.32. It can be noticed that a hot spot repeatedly appears on the right. This hot spot is also observed when measuring the irradiance uniformity with the mercury arc lamp and is therefore not due to the change of illumination. This systematic variation is most probably due to the aberrations and misalignment of the optics. The overall performance of the system might therefore be improved by a better alignment of the optics.

### 2.2.4 Print tests

The most convincing test is to make prints with a test mask, with the LEDs system in the mask-aligner. The LEDs and reflectors systems are mounted, like previously, before the fly's eye integrator of a MA/BA8 Gen3 SUSS mask-aligner. Structures of different sizes ranging from

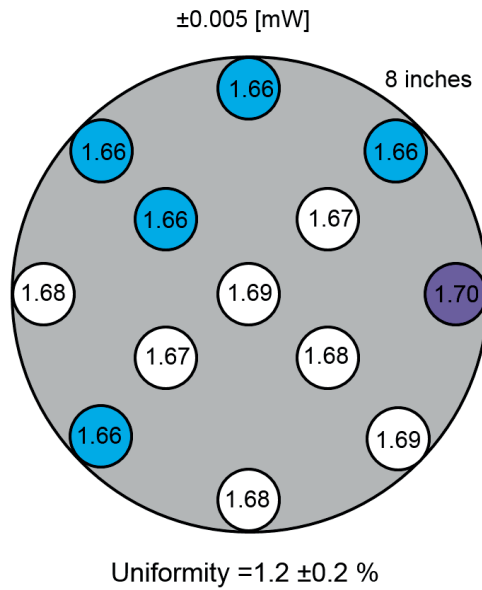


**Figure 2.31** – The irradiance uniformity measurement in the mask plane for the 7x7 LEDs illumination. The highest value of irradiance is in red, the lowest in blue. Notice the hot spot on the right.

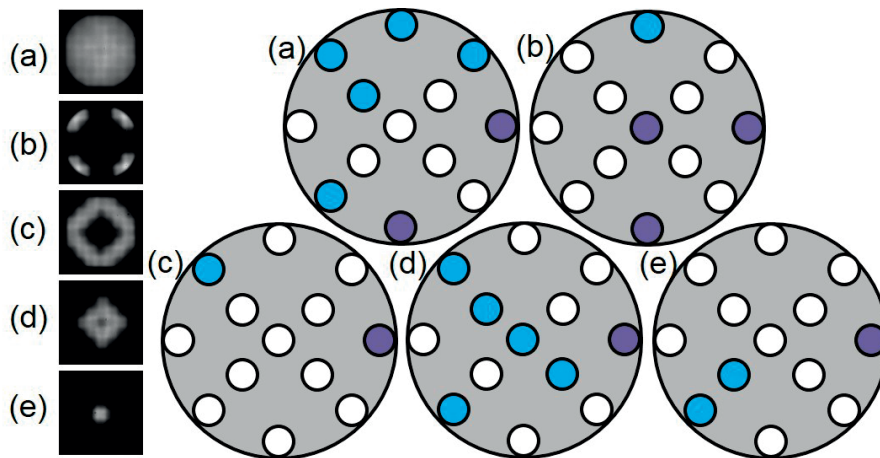


**Figure 2.32** – A schematic representation of the irradiance uniformity for the different patterns. The spots with the lowest intensity are in blue and the ones with the highest intensity are in red. There is repeatedly a hot spot on the right, probably indicating a non-uniformity due to the optics. (a) 7x7 LEDs, i.e. all LEDs are turned on, (b) corners, (c) large ring, (d) small ring, (e) center LED.

800 nm to tens of microns are present on the mask.

For the 2x2 system, both contact printing and proximity printing, with a proximity gap set to 30  $\mu\text{m}$  are carried out. A layer of 1  $\mu\text{m}$  of AZ1518 resist is deposited on 4 inches silicon wafers. The wafer is then exposed to a dose of 44  $\text{mJ}/\text{cm}^2$ , which is determined after performing a dose

## 2.2. Characterization of the performance of the prototype

test. The development is done for 1 minute in AZ351B 4/1 from AZ Electronic Materials. In Fig. 2.33, the results are shown for both contact printing (a) and (b) and proximity printing (c) and (d). We can see that in contact, a resolution of 1  $\mu\text{m}$  is achieved. This result is consistently repeated on different areas of the wafer with slight variations of the achieved resolution. For the case with 30  $\mu\text{m}$  proximity gap, a resolution of 3  $\mu\text{m}$  is achieved, but with strong diffraction effects. The diffraction effect are expected because of the small angles of incidence in the mask plane, which are below 1 degree. The 5  $\mu\text{m}$  structures, with a period of 10  $\mu\text{m}$  are well printed. Those results are in very good agreement with the expected resolutions. For a grating with a period twice the size of the structure, the resolution in proximity printing is given by [31]:

$$R \propto \sqrt{\lambda g} \quad (2.5)$$

where  $\lambda$  is the exposure wavelength and  $g$  is the proximity gap. With an exposure light at 365 nm and 30  $\mu\text{m}$  gap, it gives 3.3  $\mu\text{m}$  resolution.

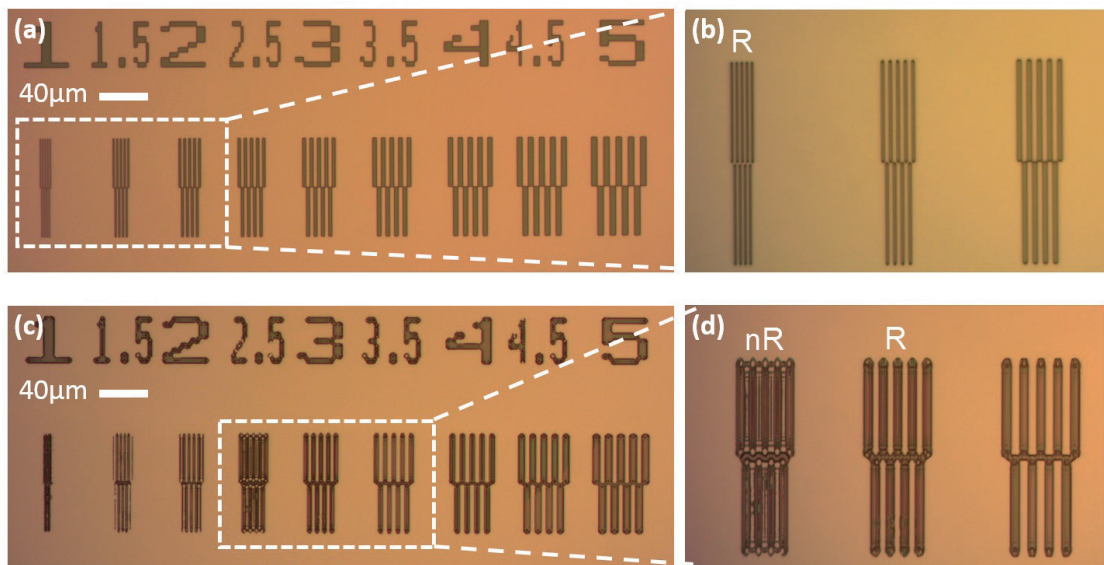







**Figure 2.33** – The print test results with the 2x2 LEDs illumination in (a) and (b) contact printing, the R indicates the last resolved structure. (c) and (d) in proximity printing with a proximity gap of 30  $\mu\text{m}$ , the R indicates the last resolved structure, the nR indicates a not resolved structure.

The same experiment is conducted with the 7x7 LEDs system. The system is mounted before the fly's eye integrator and the different patterns are tested for a proximity gap of 30  $\mu\text{m}$ . Once again, a layer of 1  $\mu\text{m}$  of AZ1518 resist is deposited on 4 inches silicon wafers. The process is similar but presents some differences. The wafer is exposed to a dose of 63  $\text{mJ}/\text{cm}^2$ , which is determined after performing a dose test. As the different illumination patterns have different numbers of LEDs, the exposure time needed to reach the required dose varies from one to the

## Chapter 2. High power UV LED illumination system

other. The irradiance in the mask plane and exposure time for each print are summarized in Table 2.6. The LEDs are not driven at their maximum power. The development is done for 45 seconds in AZ351B 4/1 from AZ Electronic Materials.

**Table 2.6** – Exposure time used for the prints with the different illumination patterns

| Pattern   | Pattern    | Irradiance [mW/cm <sup>2</sup> ] | Exposure time [s] |
|---|------------|----------------------------------|-------------------|
|  | center LED | 0.16                             | 393               |
|  | small ring | 5.2                              | 12.2              |
|  | large ring | 15.1                             | 4.23              |
|  | corners    | 5.1                              | 12.6              |
|  | 7x7 LEDs   | 13.4                             | 4.8               |

The results for the different patterns are shown in Fig 2.34 to Fig. 2.38. They all exhibit a resolution of at least 3.5  $\mu\text{m}$ , which, once again, corresponds to the expected resolution. As the dose test was only performed with the 7x7 pattern, the size of the line is therefore not optimized when printing with the other patterns. This is explained because the patterns on the fly's eye integrator determine the angular distribution in the mask plane. Having different angles change the slope of the irradiance level of the aerial image behind the mask. After development, those variations influence the width of the lines.

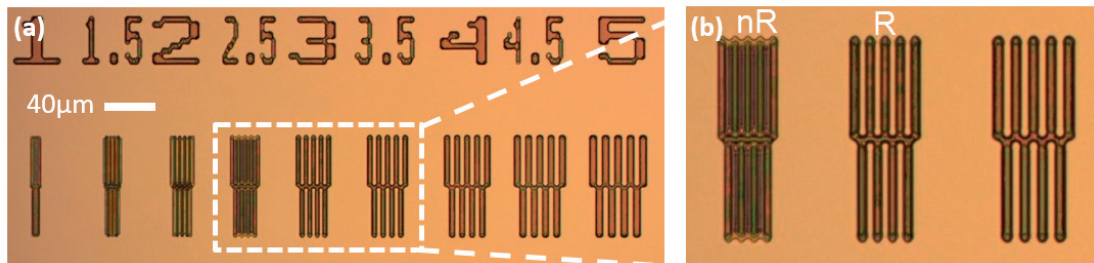


**Figure 2.34** – The print test results with the 7x7 LEDs illumination in proximity printing with a proximity gap of 30  $\mu\text{m}$ . R is for a resolved structure, nR for a not resolved one.

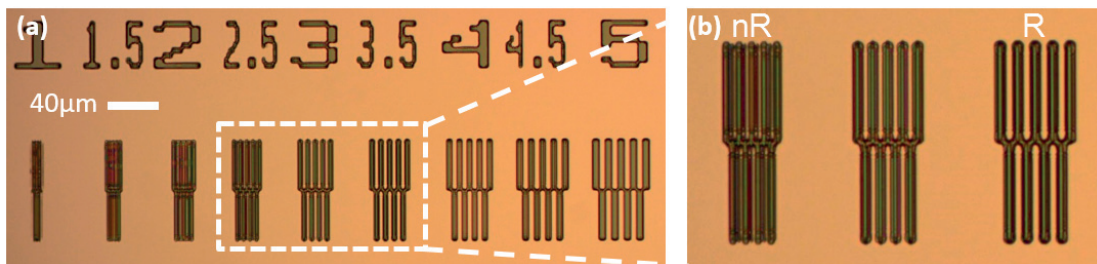


**Figure 2.35** – The print test results with the corners illumination in proximity printing with a proximity gap of 30  $\mu\text{m}$ . R is for a resolved structure, nR for a not resolved one.

The resolution is of 3  $\mu\text{m}$  for the prints with the 7x7 LEDs pattern and it could probably be

## 2.2. Characterization of the performance of the prototype

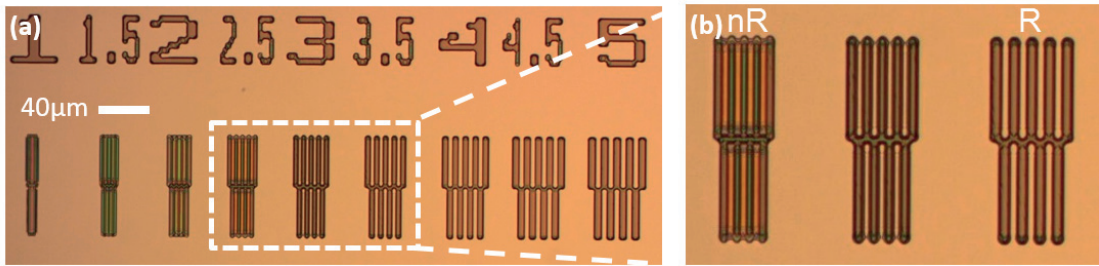


**Figure 2.36** – The print test results with the large ring illumination in proximity printing with a proximity gap of  $30\ \mu\text{m}$ . R is for a resolved structure, nR for a not resolved one.

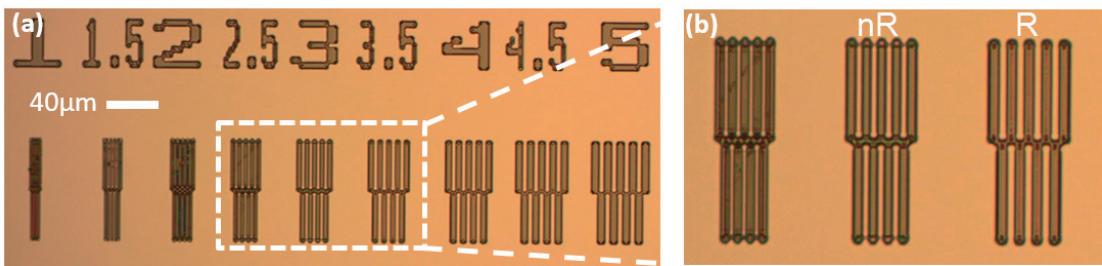


**Figure 2.37** – The print test results with the small ring illumination in proximity printing with a proximity gap of  $30\ \mu\text{m}$ . R is for a resolved structure, nR for a not resolved one.

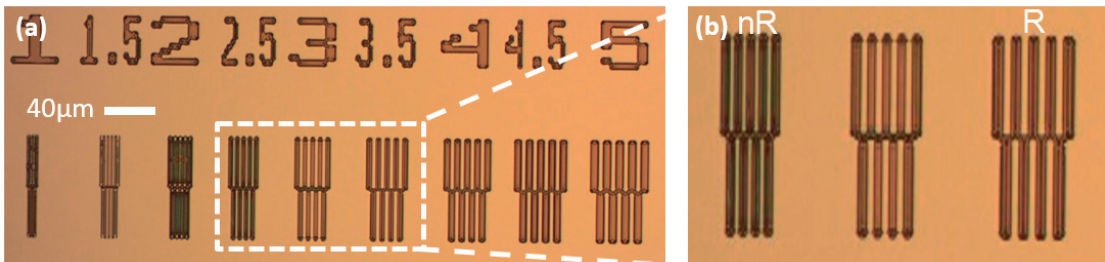


**Figure 2.38** – The print test results with the center LED illumination in proximity printing with a proximity gap of  $30\ \mu\text{m}$ .

reached with the other patterns as well, with an optimized process. For the sake of comparison, the same parameters were used for all the prints. We can observe differences in the diffraction and interference effects depending on the pattern chosen. Obviously, the print with the center LED in Fig. 2.38 exhibits more interference effects than the one in with the  $7 \times 7$  LEDs in Fig. 2.34. This is intuitively explained by the variation of the spatial coherence of the light in the mask plane. Indeed, the  $7 \times 7$  LEDs pattern results in angles within  $\pm 3.5^\circ$ , where the center LED gives angles within  $\pm 1^\circ$ . The larger source has a lower spatial coherence than the smaller source. The link between the angular distribution and the spatial coherence is further investigated in Chap. 3. The  $3.5\ \mu\text{m}$  structures with the central LED have corners that are more flat than with the other illumination patterns. These kinds of effect are to be taken into account when designing the mask for lithography. When trying to print different features, the pattern can be

chosen accordingly. This is what is done in source-mask illumination techniques, providing a better print quality and resolution than with standard illumination. The best solution for this kind of application would be to have the 7x7 LEDs all being driven independently, forming a programmable source. This can be developed for further prototypes.

### 2.3 Summary

A prototype of an LED-based system is demonstrated as a replacement for a mercury arc lamp in mask-aligners. A system of 2x2 LEDs was built to demonstrate the performance. This module consists in an assembly of individual fans mounted together. This allows to have a modular system which can easily be scaled. The prototype shows a very good performance. The angular distribution after the reflectors demonstrates an intensity uniformity of about  $\pm 5\%$  over an angular extent of  $\pm 7^\circ$ . The distribution also shows that most of the light is within an angular extend of  $\pm 10^\circ$ , which corresponds to the acceptance angle of the fly's eye integrator. The measurement after the fly's eye integrator shows that the uniformity is within  $\pm 5\%$  over an angular range of  $\pm 9^\circ$ , which corresponds to the datasheet of the element used for this characterization. The measured optical power efficiency of the reflectors for this 2x2 system is of  $36 \pm 3\%$ . This efficiency can be improved by improving the polishing, choosing a better suited aluminum or applying a coating on the reflective surface. A second prototype based on the same design but with a higher power was also built. It consists in an array of 7x7 LEDs at 365 nm. This prototype includes a cooling system and a complex electronics. It allows the determination of different patterns to shape the angular spectrum, defining the spatial coherence in the mask plane.

By mounting the prototypes in a MA/BA8 Gen3 mask-aligner, an uniformity of  $\pm 2.59 \pm 0.24\%$  is found with the 2x2 system and of  $\pm 1.2 \pm 0.2 - 2 \pm 0.7\%$  with the 7x7 LEDs system, depending on the pattern used. This is better than the performance achieved with the mercury arc lamp. Print tests in contact and proximity, realized with the 2x2 prototype, result in a resolution of respectively  $<1\ \mu\text{m}$  and  $3\ \mu\text{m}$ . This result, once again, matches the specifications of the machine. The prints with the 7x7 LEDs system in proximity also result in a resolution of  $3\text{-}3.5\ \mu\text{m}$ .

Overall, the novel LED-based illumination system shows a similar or improved performance compared to a mercury arc lamp illumination. The main difference between the two systems is the angular distribution in the mask-plane. This does not seem to impact the resolution, but would need further investigation to determine if this could limit the applications of the system, for different kind of prints. Overall, the characterization of the LED-based illumination confirms that the module is compatible with existing machines. It also provides a new flexibility for shaping the illumination and realizing multiple exposure prints.



### 2.4 Possible improvements and future developments

Different aspects of the current design of the prototype can be improved. Apart from the minor mechanical and electrical details that could be improved, there are also a number of interesting developments. As mentioned in the section about the tolerances of the system, the efficiency of the reflectors could be greatly improved by increasing the reflectivity of the light on the polished aluminum. Improving the specular reflectivity of a few percents results in an consequent improvement of the efficiency of the reflectors. Increasing the reflectivity from 66 % to 78 % improves the efficiency from 46 % to 64 %. Decreasing the losses due to positioning and due to leakage at the junctions between the reflectors is another strategy to improve the overall efficiency of the reflector. Different solutions can be tested, including better tools for the machining (like diamond tool), an automated polishing process, or coatings on the reflective surfaces. Looking at different types of aluminum might help to find one that is more reflective in the UV range and that can be polished more easily.

The efficiency of the reflectors could also be improved by optimizing their shape to the emission characteristics of the given LEDs. This was done by Van Giel et. al. in [15] which resulted in an improvement of a few percents of the overall theoretical efficiency of the reflector.

Concerning the architecture of the system, going to individually driven LEDs is, of course, of great interest. The angular distribution could be modified more precisely according to the structures to be printed. But to do so, more space would be needed on the PCB. For now, the screws and the pins used to fix the fans to the PCB are now traversing both the plastic spacer and the PCB itself in such a way that the heads of the screws are located in the PCB. An improvement would be to locate the heads of the screws inside of the spacer plate. This would increase drastically the wiring space available on the PCB. This has another advantage of making the assembly of the system easier. The fans could be mounted directly on the spacer and the PCB with the LEDs would be therefore separated from the reflectors. This would make it easier to replace an LED if needed or to change the PCB once the lifetime of the LEDs is reached.

Some variations in the optics could also be made. The system would be improved by making the irradiance on the fly's eye integrator more uniform, and thus improving the uniformity of the angular distribution in the mask plane. An improvement can probably be achieved by setting individual lenses in front of the output of the reflectors. Another solution would be to adapt the shape of the reflectors in order to make the output more uniform. The difficult part of this kind of optimization is to ensure that the angular extent on the fly's eye integrator stays the same, in order to match the acceptance angle.

It would also be interesting to combine modules of different wavelengths. For wavelengths with a spectral separation large enough, this can be done with a dichroic mirror. Otherwise, the different wavelengths can be distributed over the PCB, but in this case, the optics would have to be changed in order to make sure that all the angles have the same spectral distribution.

## **Chapter 2. High power UV LED illumination system**

---

Of course, due to the versatility of the system, new printing techniques should be tested. Due to the fact that the LEDs are electronically driven, it is possible to change the angular distribution in the mask-plane during the exposure. The angles could thus be modified depending on the depth of the light in the resist. Doing multiple exposures is also very easy with an electronically driven light source. Another interesting printing technique to test is to do greytone or greyscale lithography. The intensity of the different patterns can be set to different levels, making it possible to make a “one-shot” greytone print.

## 3 Spatial coherence in illumination systems

This chapter describes the basics of the coherence properties of light in illumination systems. Apparatus to measure the degree of spatial coherence are developed, based on a double slit approach. Simulations of the interference pattern of the light for these apparatus are developed based on two different models.

### 3.1 Motivation

The coherence properties of the exposure light is very important in proximity and projection lithography because it influences the resolution [32]. The small structures on the mask lead to diffraction and interference effects. The way the light propagates behind a given aperture is determined by the intrinsic properties of the light, mainly its wavelength and coherence. Lasers are very coherent sources and mercury arc lamps are very incoherent sources, while LED are somewhere in between the two. Being able to measure and ultimately control the coherence properties of a source is particularly useful when developing optical proximity correction structures or when doing source mask optimization. Off-axis illumination techniques for resolution improvement are based on spatial coherence management [32, 33]. With the new LED-based source with a very versatile angular spectrum, it is important to determine how the spatial coherence is affected in the mask plane when choosing different illumination patterns. The end goal of this work is to develop a measurement apparatus which allows an easy measurement of the spatial coherence length in a mask-aligner, or in other illumination systems. The second important part of this chapter is to establish experimentally the relation between the illumination angles created by the different illumination patterns and the spatial coherence length in the mask plane. The relation between the angular extent of a source and its spatial degree of coherence is theoretically established by Wolf and Carter in their work [45], which states that “the radiant intensity of a large two-dimensional statistically homogeneous source is related to the Fourier transform of the spatial degree of coherence of the source”.

### 3.2 Basics of light coherence

When two or more light waves interact with each others, they can produce an illumination pattern that is different from the sum of their individual illumination pattern. This kind of pattern is called an interference pattern. The coherence of a light wave determines the contrast of the interference pattern produced. Light that is very coherent produces interference patterns that have a high contrast.

To simplify the representation of the coherence of light, it is separated into to components: temporal and spatial. The temporal coherence is related to the spectral bandwidth of the source, where as the spatial coherence is determined by the physical extent of the light source or its emission angular distribution. They both can change upon propagation of light. Figure 3.1 illustrates the difference between a coherent light and an incoherent light. The upper part illustrates an example of a coherent monochromatic spherical wave. The succeeding wavefronts are identical to each other. Regarding the time dependence, if one point on the propagation axis is observed, the succession of wavefronts is regular and predictable. On the contrary, when looking at incoherent light, it can be observed that the wavefronts do not resemble each other and that is is impossible to predict how they change in time.

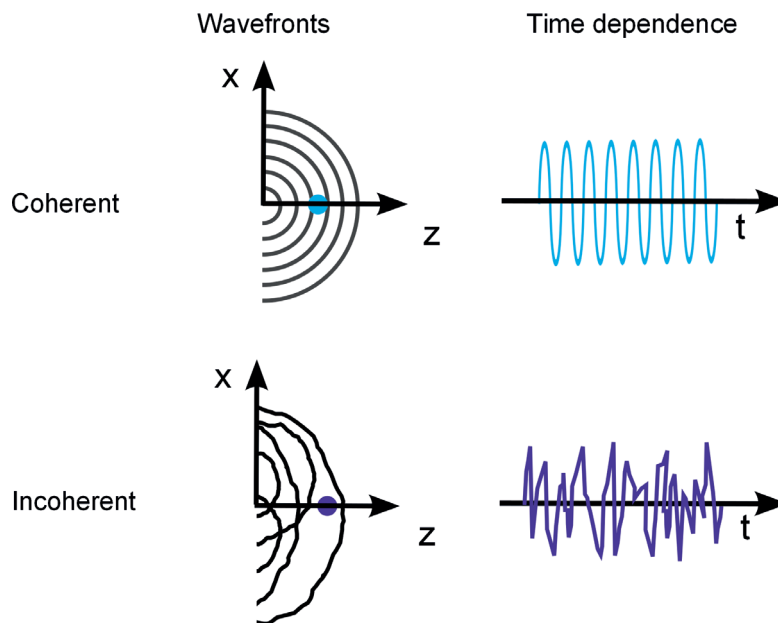


**Figure 3.1** – The time dependence and wavefront representation of (a) a spherical monochromatic source which is coherent and of (b) incoherent light

A common way to quantify the coherence is by using the complex degree of coherence. It determines the degree of correlation of a wave. A wave can be described by the complex wavefunction  $U(\mathbf{r}, t)$ , where  $\mathbf{r}$  is the position vector and  $t$  is the time. Its average intensity is given as  $I(\mathbf{r}, t) = \langle |U(\mathbf{r}, t)|^2 \rangle$  [34]. The complex degree of coherence is the normalized cross-correlation of the wave at a position 1 with the wave at a time  $\tau$  later and at a position 2. It is

expressed as follows:

$$\mu(\mathbf{r}_1, \mathbf{r}_2, \tau) = \frac{\langle U^*(\mathbf{r}_1, t)U(\mathbf{r}_2, t + \tau) \rangle}{[I(\mathbf{r}_1)I(\mathbf{r}_2)]^{1/2}} \quad (3.1)$$

If two points are coincident ( $r_1 = r_2$ ), then the expression gives the temporal coherence and is expressed as:

$$\mu(\mathbf{r}, \tau) = \frac{\langle U^*(\mathbf{r}, t)U(\mathbf{r}, t + \tau) \rangle}{[I(\mathbf{r})I(\mathbf{r})]^{1/2}} \quad (3.2)$$

When  $\tau = 0$ , Eq. (3.1) describes the spatial coherence. It reduces to:

$$\mu(\mathbf{r}_1, \mathbf{r}_2) = \frac{\langle U^*(\mathbf{r}_1)U(\mathbf{r}_2) \rangle}{[I(\mathbf{r}_1)I(\mathbf{r}_2)]^{1/2}} \quad (3.3)$$

The magnitude of  $\mu(\mathbf{r}_1, \mathbf{r}_2)$  is comprised between zero and one:

$$0 \leq |\mu(\mathbf{r}_1, \mathbf{r}_2)| \leq 1 \quad (3.4)$$

When the two waves are fully correlated, the value is 1, which means that the waves evolve in a synchronized manner. When the waves propagate and fluctuate independently from each other, the degree of coherence goes to zero. This work focus on the spatial changes. In case of quasi-monochromatic light (when the optical path differences in the system is much smaller than the temporal coherence length), the magnitude of the complex degree of coherence gives a measure of the degree of spatial coherence. This relation is used to display the spatial coherence of a one-dimensional beam in the work from Mendlovic et. al. [35]. The mutual intensity is done optically and can therefore be displayed.

### 3.3 Methods for measuring the spatial coherence

Different methods exist for measuring the spatial coherence of a light beam. The easiest way is to use a simple double pinholes approach to measure the degree of coherence, as presented by Zernike in 1938[36]. Practical measurements of two-beam interference of partially coherent light has also been discussed in 1956 in the paper by Thompson and Wolf [37]. A few methods

were derived from this approach, with a higher degree of complexity that results in measurements containing added information. For example, a multi pinholes approach is described by Mejía and González in [38] and Smith and Dainty in [39]. Pinholes are set side to side on a line, with different distance between them. The resulting interference pattern includes the two-by-two interference for each pinhole pair. The pairs which separation length is smaller than the coherence length of the light beam will interfere with a high contrast, where as the pairs with a separation close to or wider than the coherence length will have a lower contrast of the fringes to no contrast at all. This method has the advantage of giving directly the spatial coherence length along the direction of the pinholes array. In the cited contributions, the array of pinholes is used to measure the coherence length along the axis of a He-Ne laser. Another double pinholes based method is presented by Divitt et. al. in [40] and Divitt and Novotny [41]. They use an apparatus based on non-parallel double slits to get a continuous measurement of the interference pattern along a varying slits separation. They use it to characterize the light from a fiber bundle from a very far distance and to measure the coherence of the sun for applications in photovoltaic technologies. The non-parallel double slits allows a continuous measurement of the contrast as a function of the separation between the slits. This is an advantages compared to the multi pinholes approach, which gives a sampled measurement. The non-parallel slits approach therefore allows to determine more precisely the spatial coherence length. It is shown that the degree of coherence as a function of the separation of the slits follows a Bessel function. Using slits instead of pinholes also presents another advantage in the fact that more light reaches the detector.

In this work, it is important to be able to measure easily the spatial coherence in the mask plane. Therefore, slits are used in order to have a good signal-to-noise ratio. Both double slits and multi slits approaches are investigated. Having parallel slits also makes it possible to average over many lines of the camera, improving again the signal-to-noise ratio. A method to measure the spatial coherence in a bidirectional planar way is presented in the last part of this chapter. It allows to measure the spatial coherence in a two-dimensional plane. This is needed for measuring the degree of coherence in a mask-aligner. The angular distribution in the mask plane of a mask-aligner is determined by the illumination patter on the fly's eye integrator, and thus the illumination angles are two-dimensional.

### 3.4 Double and multi slits interference

The mathematical description of the interference of two partially coherent monochromatic waves can be expressed by the superposition of the complex amplitudes. Let's assume  $U_1(\mathbf{r})$  and  $U_2(\mathbf{r})$ , where  $\mathbf{r}$  is a position vector, arrive on the observation plane. The resulting field is the addition of both:

$$U(\mathbf{r}) = U_1(\mathbf{r}) + U_2(\mathbf{r}), \quad (3.5)$$

which results in an interference pattern that can be expressed as:

$$I(\mathbf{r}) = \langle |U(\mathbf{r})|^2 \rangle = \langle |U_1(\mathbf{r}) + U_2(\mathbf{r})|^2 \rangle = I_1 + I_2 + 2(I_1 I_2)^{1/2} |\mu(\mathbf{r}_1, \mathbf{r}_2)| \cos \phi, \quad (3.6)$$

where  $I_1 = |U_1(\mathbf{r})|^2$ ,  $I_2 = |U_2(\mathbf{r})|^2$ , the amplitude of the degree of coherence  $|\mu(\mathbf{r}_1, \mathbf{r}_2)| = |\mu_{12}|$  is given by the contrast of the fringes, and  $\phi$  is the phase difference between the two waves. In the case where the two waves have the same amplitude,  $I_1 = I_2 = I$  and if we only consider the problem in one dimension, the equation can be written as:

$$I(x) = 2I [1 + |\mu_{12}| \cos \phi_{12}]. \quad (3.7)$$

This equation is valid as long as the path difference between the two beams is much smaller than the temporal coherence length of the source, which is given by  $\lambda^2/\Delta\lambda$ . This condition ensures that the degree of coherence  $\mu_{12}$  depends solely on the spatial property of the source and not on the temporal coherence properties. In practice, for a laser at a wavelength of 405 nm with a bandwidth of 1 nm, the temporal coherence is 164  $\mu\text{m}$ . For LEDs at a wavelength of 405 nm and with a bandwidth of 10 nm, which is typical, temporal coherence is of 16  $\mu\text{m}$ . In the case of a double slits configuration, this limits the separation between the slits for which the condition on the path difference is respected. For a propagation length of 3.6 mm, which results in small angles, the maximum slits separation is 240  $\mu\text{m}$ . For slits separations greater than that, the degree of coherence does not solely depend on the spatial coherence anymore.

When doing experiments and analyzing the interference pattern of two beams, there exist different methods to retrieve the contrast of the fringes, and thus the modulus of the spatial degree of coherence. For the double pinholes configuration, an analytical solution of the interference can be found. The recorded pattern can then be fitted with the analytical curve and the degree of coherence can be retrieved in that way. Another technique, which is very widely used because of its rapidity and robustness, is to take the Fourier transform of the recorded intensity  $\tilde{I}$  (see Ref. [39]):

$$\tilde{I}(u) = 2I \left[ \delta(u) + \frac{|\mu_{12}|}{2} (\delta(u - u_1) + \delta(u + u_1)) \right], \quad (3.8)$$

where  $u$  is the spatial frequency of the interference pattern. The central delta function  $\delta(u)$  corresponds to the amount of light present in the observation plane. The shifted delta functions  $\delta(u \pm u_1)$ , which have a smaller magnitude, represent the magnitude of the interaction between the interfering beams. The contrast of the fringes of the interference pattern is there-

fore given by the magnitude of the second peak divided by the magnitude of the central peak and multiplied by two.

As mentioned in the introduction of this chapter, a multi pinholes or multi slits approach can be used in order to directly measure the spatial coherence length. The interference from multiple apertures is very similar to the interference with two pinholes. The light going through the different apertures will mutually interfere, as long as their separation is within the coherence length of the light source. Similarly to what is presented for two slits, for three apertures with equivalent intensities,  $I_1 = I_2 = I_3 = I$ , the interference pattern in the observation plane can be written as [39]:

$$I(x) = 3I \left[ 1 + \frac{2}{3} |\mu_{12}| \cos \phi_{12} + \frac{2}{3} |\mu_{13}| \cos \phi_{13} + \frac{2}{3} |\mu_{23}| \cos \phi_{23} \right]. \quad (3.9)$$

The contrast can again be retrieved from the Fourier transform of the interference pattern:

$$\begin{aligned} \tilde{I}(u) = 3I \left[ \delta(u) + \frac{|\mu_{12}|}{3} (\delta(u - u_1) + \delta(u + u_1)) + \right. \\ \left. \frac{|\mu_{23}|}{3} (\delta(u - u_2) + \delta(u + u_2)) + \right. \\ \left. \frac{|\mu_{13}|}{3} (\delta(u - u_3) + \delta(u + u_3)) \right], \end{aligned} \quad (3.10)$$

Here, the result consists in a distribution of delta functions at frequencies corresponding to the spatial frequencies in the interference plane. Those spatial frequencies in the observation plane are directly related to the separations of the slits. The amplitude of those delta functions are directly proportional to the amount of light present in each frequencies. Taking the ratio of one of the delta function to the main peak and multiplying it by the number of apertures, directly gives the value of the contrast for this specific pair of apertures. With well designed arrays, it is possible to get a direct representation of the contrast as a function of the distance between the apertures. This is the underlying principle of the method of coherence measurement that is developed in the coming section.

### 3.5 Design of a coherence measurement apparatus

In this section, the design of double slits and multi slits for the coherence measurement is described. The apparatus consists of a mask with the slits followed by a camera sensor onto which the pattern is recorded. Different constrains determine the slits width and separation. The design is then tested with simulations.



### 3.5.1 Double slits design

In order to validate the design of a double slits based system to measure spatial coherence, simulations are carried out in MATLAB. The advantage of having slits over pinholes is that their is more collected light and that multiple lines can be averaged along the lines in order to increase the signal-to-noise ratio. The constrains on the design are mainly the compactness. As the final goal is to measure the coherence in the mask-aligner, the design of the slits is done accordingly. As mentioned in the previous chapters, the angles in the mask-plane are determined by the size of the light field arriving on the fly's eye integrator as well as the focal length of the front lens (see Fig. 1.7). In this particular case, the front lens is given to have a focal length of 660 mm. The size of the optical element gives the size of the light beam and is of 80 mm. This results in a half angle of 3.5°. The smallest angle to measure is about 0.8°. The sensor used also has a finite size, and a certain pixel size. The design has to ensure that the interference pattern can be measured over a given number of fringes and with sufficient contrast and resolution. It is even more critical as the Fourier transform has to be performed on on the recorded pattern. The design should therefore make sure that the envelope of the signal is wide enough such that at least 5 fringes can be seen. The frequency of the fringes should not be too high so that one fringe is measured over enough pixels.

Another point is that the design should be compatible for wavelengths between 365 nm and 405 nm. Those are the two wavelengths which are most used and which will be used with the system. With these constrains, it is not evident to find a design of double slits that can be easily manufactured. Since the angles are rather small, the slits need to be close to each other, which means they also need to be thin. The replication of the slits limit their width to 800 nm. Another constrain is the compactness of the system. The space available to do the measurement in the mask-aligner is only of 20 mm, vertically. This means that the distance from the slits to the sensor should be short, as the sensor itself already takes 15 mm. The different constrains on the system are summarized in the table 3.1.

**Table 3.1** – Design constrains of the coherence measurement tool

| Constrain          | Value                    |
|--------------------|--------------------------|
| Angular range      | 0.8 - 3.5 [°]            |
| Sensor size        | 5 x 6 [mm <sup>2</sup> ] |
| Sensor pixel size  | 5.2 [µm]                 |
| System height      | 20 [mm]                  |
| Propagation length | 5 [mm]                   |
| Number of fringes  | 5                        |
| Wavelength         | 365 and 405 [nm]         |
| Slits width        | > 800 [nm]               |
| Slits separation   | > slits width            |

### Chapter 3. Spatial coherence in illumination systems

The interference pattern can be modeled by a sinus cardinal (sinc) function modulated by a cosine. This is shown schematically in Fig. 3.2, where the sinc function is in purple and the cosine function is in light blue. The camera sensor is placed at a distance  $d$  from the mask with the slits.

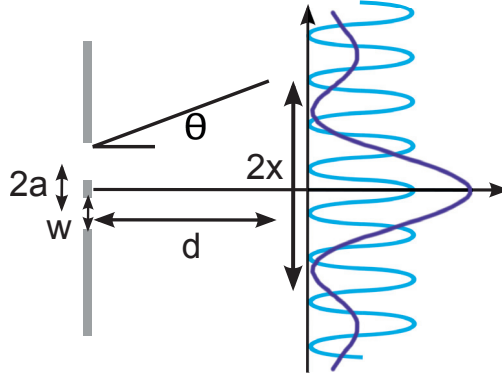


**Figure 3.2** – A schematic of the double slits configuration and parameters. The separation of the slits is given by  $2a$ , their width by  $w$ , the distance to the plane is  $d$  and the size of the camera sensor is  $2x$ . The interference pattern is a sinc function modulated by a cosine function.

#### Slits width

The width of the slits is responsible for the lateral size of the sinc function. As the lobes of the sinc function have a lower intensity than the main peak, the design was made in a way that the first minimum of the sinc function is close to the edge of the sensor of the camera. The angle of the first zeros of the diffraction from one slit is given by:

$$\sin \theta = \frac{\lambda}{w}, \quad (3.11)$$

where  $w$  is the width of the slit,  $\lambda$  is the wavelength of 365 nm or 405 nm,  $\theta$  is the diffraction angle. The angle  $\theta$  should therefore ensure that the first zero falls at the edge of the camera sensor at the given propagation distance. In this case, the sensor is  $2x= 5$  mm wide and with a propagation distance of  $d= 3.5$  mm this gives :

$$\theta = \sin^{-1} \left( \frac{\lambda}{w} \right) \leq \tan^{-1} \left( \frac{x}{d} \right) = 0.62[\text{rad}] \quad (3.12)$$

The minimal size for  $w$  for the diffraction angle to be small enough is therefore  $0.63 \mu\text{m}$ . Smaller slits would anyway be difficult to replicate. On the other hand, in order to make the evaluation and the simulation more convenient, the measurement should be made in the far

### 3.5. Design of a coherence measurement apparatus

---

field in order for the Fraunhofer approximation to be valid. This means that the propagation can be simulated by a Fourier transform, which presents the computational advantage of being fast. This condition can be verified by computing the Fresnel number,  $N_F$ , and ensuring that it is much smaller than 1:

$$N_F = \frac{w^2}{\lambda d} \ll 1, \quad (3.13)$$

where  $w$  is the size of the diffracting element,  $\lambda$  is the wavelength of the propagating light and  $d$  is the distance from the diffracting element to the observation plane. In this case,  $w \ll \sqrt{365 \text{ nm} \cdot 3.5 \text{ mm}} = 35.7 \mu\text{m}$ . The slits should therefore be much smaller than  $35 \mu\text{m}$  and larger than  $0.6 \mu\text{m}$ . The slits are chosen to be  $1 \mu\text{m}$ .

#### Slits separation

The separation between the slits determines the spatial frequency of the cosine modulation of the interference pattern. It is also what limits the measurable spatial coherence length and therefore the maximum extent of the source, which can still be measured.

A first condition to verify is that there are enough interference fringes on the camera. This is important for the Fourier transform to accurately represent the light into the different spatial frequencies. On the other hand, the fringes should not be too narrow either. It should still be possible to resolve them with the camera sensor, given that it has a limited number of pixels. For the interference of the two holes, the fringes are given to have maximums at:

$$\sin \theta_m = m \frac{\lambda}{2a}, \quad (3.14)$$

where  $\theta_m$  is the angle from the source to the maximum,  $m \in N$ ,  $\lambda$  is the wavelength of 365 nm or 405 nm and  $2a$  is the slits separation. The design is made in such a way that we have 5 fringes within the first zeros of the sinc envelope. This means that  $m=2$  since the pattern is symmetrical. The first zero of the sinc envelope is at the angle calculated above of 0.62 [rad]. It means that at 365 nm:

$$\sin \theta_2 = 2 \frac{\lambda}{2a} \leq \sin(0.62), \quad (3.15)$$

which means that  $2a \geq 1.39 \mu\text{m}$ . This last condition is therefore also fulfilled with a separation of  $3.2 \mu\text{m}$ .

### Chapter 3. Spatial coherence in illumination systems

---

The angle to be measured is between  $0.8^\circ$  and  $3.5^\circ$  of half angle. The theoretical extent of a source which still allows to have a contrast larger than zero is therefore:

$$\theta_{max} \ll \frac{\lambda}{2a} \quad (3.16)$$

where  $\theta_{max}$  is the maximum angle of the illumination and  $2a$  is the slits separation (as schematically shown in Fig. 3.5). This gives the condition for which the design is still able to measure the spatial coherence. The separation between the slits is chosen to be  $3.2 \mu\text{m}$ . With  $\lambda = 0.405 \mu\text{m}$ ,  $2a = 3.2 \mu\text{m}$ , it gives:

$$\theta = 0.127[\text{rad}] = 7.25^\circ,$$

which corresponds to an angular range of  $\pm 3.63^\circ$ .

A picture of the slits recorded with a microscope is shown in the Fig. 3.3. The slits constitute an amplitude mask on a glass substrate. The opaque regions are in aluminum. The aluminum layer is about  $160 \text{ nm}$  thick. The mask was written in e-beam lithography with a chromium layer. The chromium layer is not opaque enough and let light goes through, which produces unwanted interference effects. The slits are therefore replicated by lithography on a substrate with aluminum. Due to the replication step, the slits showed variations in width of about  $\pm 0.05 \mu\text{m}$ . This will result in small variations in the observed pattern, typically changing the contrast for a given angular extent.

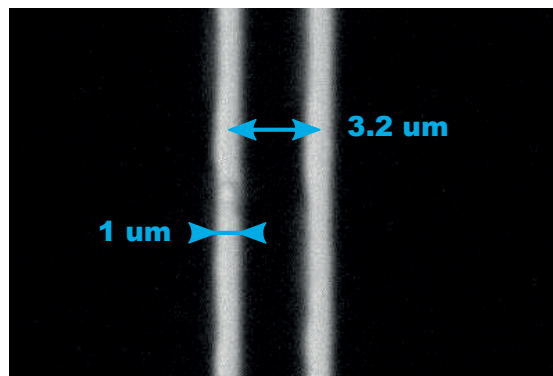


**Figure 3.3** – A photograph of the designed and fabricated slits with the dimensions of the design. In practice, the fabricated slits showed variations of about  $0.05 \mu\text{m}$  on the dimension of the width of the slits, leading to small variations in the resulting interference pattern.

3.5.2 Multi slits design

The design of the double slits makes it easy to go to a multi slits design. The slits are chosen to be  $1\ \mu\text{m}$  large, with different distances between them from  $2\ \mu\text{m}$  to  $31\ \mu\text{m}$ , as presented in the picture of Fig. 3.4. The range chosen ensure that the full angular extent can be measured. The pairs are summarized in the table 3.2. A method for generating non redundant and compact array of points is presented by Golay in [42]. For this work, we stick to slits for the mentioned advantage of having more light. The slits are fabricated in the same way as the double slits, as a structured layer of aluminum on a glass substrate.

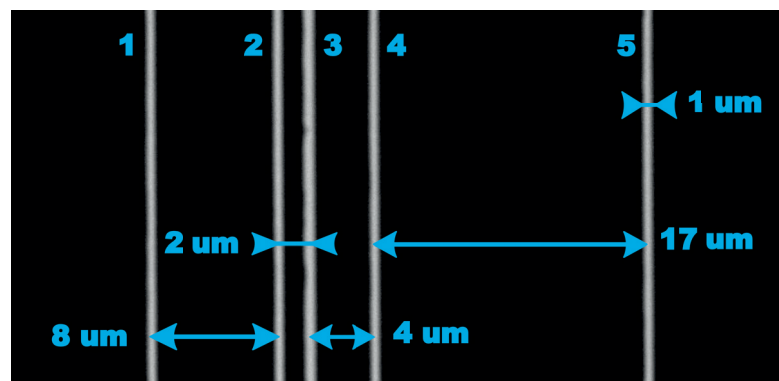


*Figure 3.4 – A photograph of the designed and fabricated multi slits with the dimensions of the design. In practice, the fabricated slits showed variations of about  $0.05\ \mu\text{m}$  on the dimension of the width of the slits, leading to small variations in the resulting interference pattern.*

*Table 3.2 – Pairs of slits*

| Pairs | Separation [ $\mu\text{m}$ ] |
|-------|------------------------------|
| 2, 3  | 2                            |
| 3, 4  | 4                            |
| 2, 4  | 6                            |
| 1, 2  | 8                            |
| 1, 3  | 10                           |
| 1, 4  | 14                           |
| 4, 5  | 17                           |
| 3, 5  | 21                           |
| 2, 5  | 23                           |
| 1, 5  | 31                           |

### 3.6 Simulating the spatial coherence

This section presents two simulation methods. They are used to validate the design of the double and multi slits. The first simulation, called the plane waves superposition method, allows to retrieve the contrast of the fringes in the interference pattern as a function of the angular extent of the illumination. The second simulation, called the random phase screens superposition, models the contrast of the fringes as a function of the spatial coherence length.

#### 3.6.1 Plane waves superposition method

##### Principle

This first simulation method is used to determine the contrast as a function of the angular extent of the source. A schematics of the simulation approach is shown in Fig. 3.5. The source field  $U_1$  is a mask with the arrangement of slits or holes. A set of tilted plane waves are built to model a source with a given angular extent. Each plane wave is propagated independently from the other. This is like considering an extended source at infinity which is composed of a superposition of independent point sources, following the Huygens principle. Each point of the source radiates incoherently from its neighboring point. The propagation is based on the Fraunhofer approximation [43], which allows to simulate the propagation by a Fourier transform. The superposition of the plane waves in the observation plane determines the interference pattern. The intensity is computed as the superposition of the independent interference patterns.

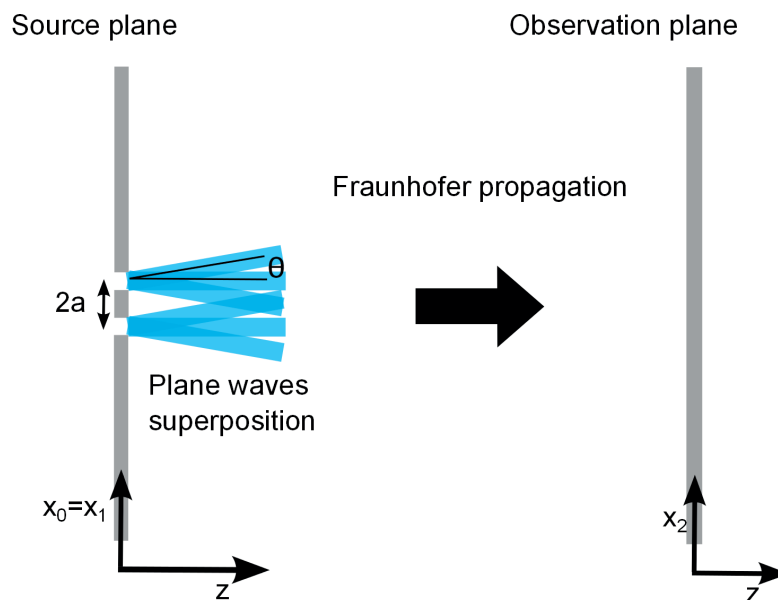


**Figure 3.5** – A schematic of the simulation principle of the plane waves superposition method. The source plane models the light distribution through a double slits mask. The plane waves with different incident angles are in blue.

#### Model

To simulate the oblique incidence of the individual plane wave, the amplitude of the source light field is multiplied by a phase term. The amplitude of the wave function is given by  $U_0(x_0, y_0)$ . The angles are taken within a range  $\theta$ , which corresponds to the angular extent of the source. The tilted field can then be written as:

$$U_1(x_1, y_1) = U_0(x_0, y_0) \exp [jk(x_0 \cos(\theta) + y_0 \sin(\theta)) \tan(\alpha)], \quad (3.17)$$

where  $U_0$  is the initial light field with coordinates  $x_0, y_0$  and  $\theta, \alpha$  are the angles. In this work, only one dimension along the x direction is considered as the slits are considered “infinite” in the other direction.  $\theta$  is therefore set to 0 and  $\alpha$  is the angle in the plane formed by the direction of propagation and the transversal direction of the slits,  $x_0 = x_1$ . This results in a 1 dimensional model.

The propagation of the light field from the source plane to the observation plane can be simulated by using the Fraunhofer approximation:

$$U_2(x_2, y_2) = \frac{\exp(jkz)}{j\lambda z} \exp \left[ j \frac{k}{2z} (x^2 + y^2) \right] \cdot \iint U_1(x_1, y_1) \exp \left[ j \frac{k}{2z} (x_2 x_1 + y_2 y_1) \right] dx_1 dy_1 \quad (3.18)$$

Where  $x_1, y_1$  are the position coordinates in the source plane and  $x_2, y_2$  are the position coordinates in the illumination plane.

The Fraunhofer approximation is used for each plane wave with a different angle. The different plane waves are taken to be incoherent with each other. This means that the interference term of Eq. (3.8) is zero and that the resulting intensity is the sum of the squared amplitudes of the light fields. This is done with Eq. (3.19):

$$I_{tot} = \sum_{\theta=0}^{\theta_{max}} |U(\theta)|^2. \quad (3.19)$$

What actually happens is that each plane wave produces an interference pattern of contrast 1. The tilted wavefronts produce a shifted interference pattern in the observation plane. By adding the interference patterns together, the contrast of the fringes decreases accordingly to the displacement between the individual patterns.

#### Results

The results of the simulation are presented in Fig. 3.6. The intensity in the output plane is an interference pattern, with an envelope determined by the parameter  $w$ , the size of the slits and with fringes frequency determined by  $2a$ , the separation between the slits. For a simple plane wave, the contrast of the fringes is equal to one, meaning that the coherence is maximal. It can be seen that, increasing the angular range of the incoming waves decreases the contrast. This is because the waves interfering have an additional phase difference due to the extent of the source. Some examples of different angular extent are shown in Fig. 3.6(a) to Fig. 3.6(e). With the increase of the angular extent, the contrast of the fringes decreases. This is also visible on the associated Fourier transforms also presented in Fig. 3.6. The secondary peaks are getting smaller. It directly represents the contrast and the fringes and is therefore a measurement of the level of coherence. If  $\pm\pi$  phase difference is reached, the contrast is reaches zero. If the angles are further increased, the pattern starts inverting, as there is more weight in the second peak of intensity.

The van Cittert-Zernike theorem states that, “for a large circular source far away from the apertures, the complex degree of coherence is equal to the absolute value of the normalized Fourier transform of the intensity distribution of the source” (see Ref. [44]). With a circular source, the degree of coherence is expressed analytically by a Bessel function:

$$|\mu| = 2 \cdot \frac{J_1(o)}{o}, \quad o = \frac{\pi\theta 2a}{\lambda}, \quad (3.20)$$

where  $\theta$  is the angular extent,  $\lambda$  is the wavelength,  $2a$  is the distance between the slits. The simulation is performed for different angular extents ranging from  $0^\circ$  to  $8^\circ$ . The width of the source plane is set to 0.1 mm with at least 800 samples. This proves to be a sufficient sampling for taking the Fourier transform of the obtained interference pattern. The simulation shows good performances when taking at least 100 plane waves for an angular extent of  $8^\circ$ . Angles within 0 to  $8^\circ$  are set in Eq. (3.20) and the corresponding contrast are computed.



### 3.6. Simulating the spatial coherence

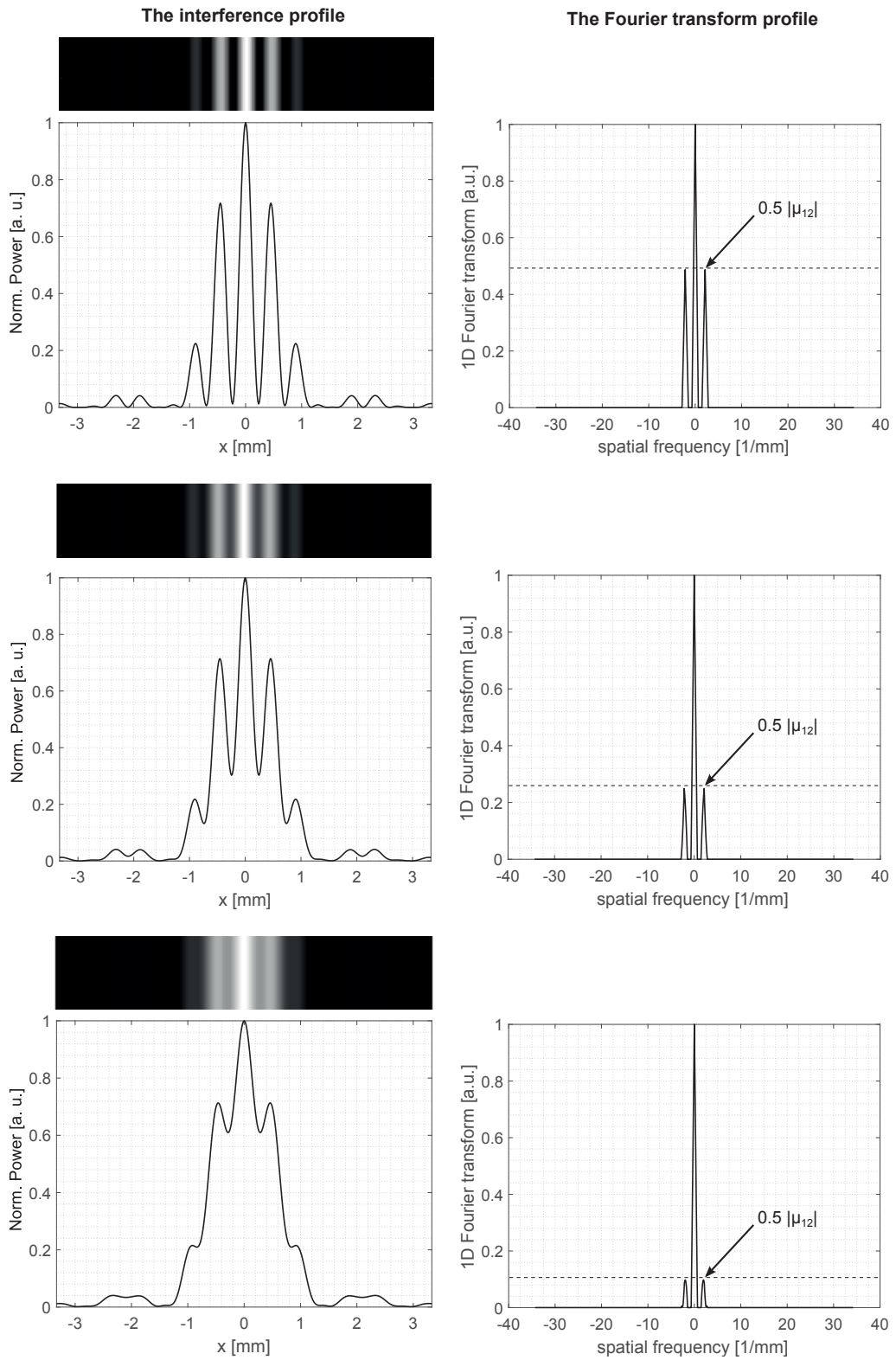


**Figure 3.6** – The simulation of the interference pattern for  $1\ \mu\text{m}$  slits with  $2a = 3.2\ \mu\text{m}$ , a propagation length of  $3.6\ \text{mm}$ , at a wavelength of  $405\ \text{nm}$ . The incoming angles and resulting contrasts are (top)  $\pm 0.46^\circ$ ,  $|\mu_{12}| = 0.98$ , (middle)  $\pm 2.2^\circ$ ,  $|\mu_{12}| = 0.56$ , (bottom)  $\pm 3.1^\circ$ ,  $|\mu_{12}| = 0.2$ .

### Chapter 3. Spatial coherence in illumination systems

The curves of the coherence as a function of the angular extent for the simulation and the theoretical expression are shown in Fig. 3.7. A small difference has to be accounted for when plotting the analytical curve. This is due to the fact that, the curve is valid for very small apertures since only the distance between them is taken into account in the equation. In the present case, the slits width is adjusted to a  $2a$  value of  $3.7 \mu\text{m}$  for the purple curve instead of  $3.2 \mu\text{m}$  for the blue curve, in order for the curves to match. There is a difference for large angles. The simulation does not goes to zero where as the analytical curve does. This can probably be improved by increasing the sampling and the number of waves superposed, but at the cost of computational time.

This evaluation shows that the results of the simulation corresponds to the analytical expression. It means that the simulation can be trusted to visualize the interference pattern produced by different kinds of apertures. The selected design of  $1 \mu\text{m}$  slits with a separation of  $3.2 \mu\text{m}$  should therefore ensure a good measurement of the contrast of the fringes with an incoming source with an angular extent from  $0^\circ$  to  $8^\circ$ .

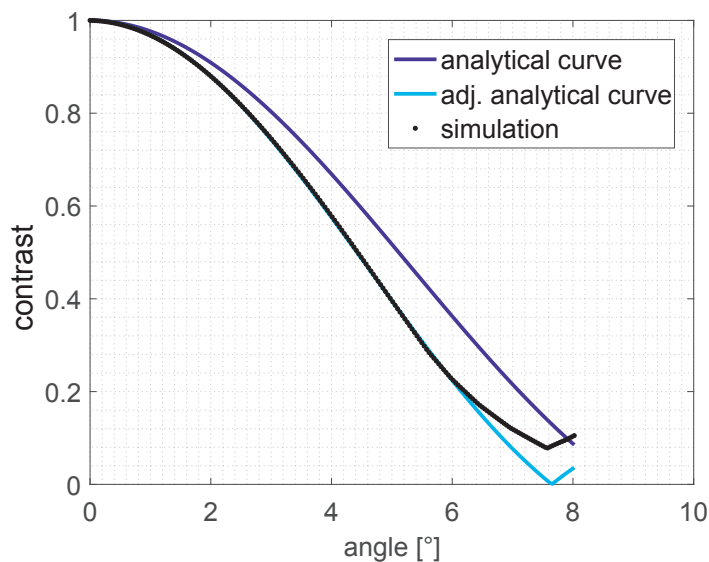


**Figure 3.7** – The contrast as a function of the angular extent of the incoming light at a wavelength of  $405 \text{ nm}$  and with slits of  $1 \mu\text{m}$ . The simulation is done with  $2a = 3.2 \mu\text{m}$  between the centers, the analytical curve in purple is with  $2a = 3.2 \mu\text{m}$  and the adjusted analytical curve in light blue is with  $2a = 3.7 \mu\text{m}$ , in order to compensate for size of the slits, which is large compared to the slits separation.

### 3.6.2 Random phase screens superposition method

#### Principle

In order to retrieve the contrast of the fringes as a function of the coherence length, a second simulation is used. This simulation method makes it possible to set the spatial coherence length as a parameter of the source, and to obtain the interference pattern. The method is freely inspired from and follows quite closely the work presented by Voelz in [43].

The idea is to create a source which contains both a deterministic field and a stochastic part. The spatial coherence is simulated by taking a random screen phase distribution and by smoothing it with a Gaussian distribution in order to create correlation. The size of the Gaussian distribution determines the coherence length of the light. The propagation is then also done by applying the Fraunhofer approximation. The process is repeated many times to create a multitude of sources and their corresponding pattern in the observation plane. Finally, the intensity patterns from the different waves are added together incoherently. The simulation is represented schematically in Fig. 3.8.

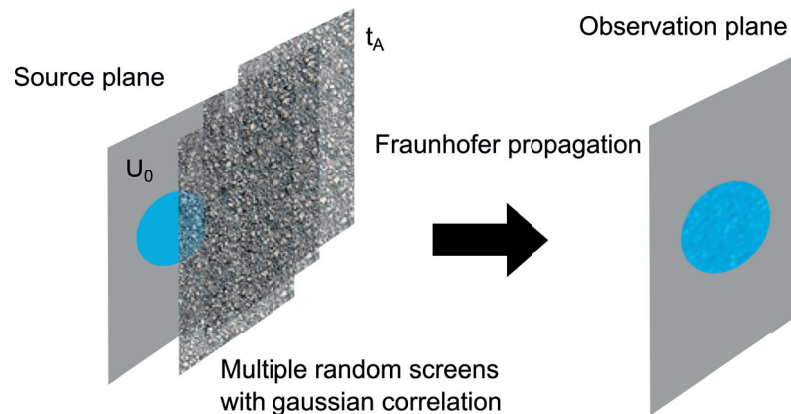


**Figure 3.8** – A schematic of the simulation principle of the multiple screens method. The blue spot of the left is the source. The screen with random phase are shown. The resulting field is shown on the right.

To have a more concrete representation of what is done, it can be compared to shining light through a phase plate. The random screen smoothed by the Gaussian distribution is equivalent to this phase plate. It creates a wavefunction composed of many subsequent waves with each a different phase. The Gaussian smoothing ensures that the different phases are linked to each other, within the coherence length.

**Model**

The separation of the source into two parts can be described as follow:

$$U(x, y; t) = U_0(x, y) t_A(x, y), \quad (3.21)$$

where  $U_0$  is the deterministic part of the field and  $t_A$  is the random transmittance screen. The random transmittance screen is described as:

$$t_A(x, y) = \exp[j\phi(x, y)], \quad (3.22)$$

where  $\phi$  is the spatially correlated random phase function, which is also called a “phase screen”. It is constructed by convoluting a random screen with a Gaussian distribution:

$$\phi(x, y) = r(x, y) \otimes f(x, y) = r(x, y) \otimes \frac{1}{\pi\sigma_f^2} \exp\left(-\frac{x^2 + y^2}{\sigma_f^2}\right), \quad (3.23)$$

where  $\sigma_f$  is the width parameter of the Gaussian correlation distribution. The degree of coherence given by the equation 3.1 can be expressed as:

$$\mu(\mathbf{r}_1, \mathbf{r}_2, \tau) = \frac{\langle U^*(\mathbf{r}_1, t) U(\mathbf{r}_2, t + \tau) \rangle}{[I(\mathbf{r}_1) I(\mathbf{r}_2)]^{1/2}} = \frac{\langle t_A^*(x_1 + x_2, y_1 + y_2), t_A(x_1, y_2) \rangle}{1}, \quad (3.24)$$

where  $l_{cr}^2 = 4\pi\sigma_f^4/\sigma_r^2$  with  $\sigma_r$ , the variance of the random signal. In the case when  $\sigma_r^2 \gg 2\pi\sigma_f^2$ , which means when the random signal varies a lot over the Gaussian distribution, this gives :

$$|\mu_{12}| = \exp\left(-\frac{x_2^2 + y_2^2}{l_{cr}^2}\right). \quad (3.25)$$

An easy way to construct the different parts of the field in MATLAB is to choose a normal distribution for the random signal, with a variance  $\sigma_r$  of 1. The parameter  $\sigma_f$  can then be determined accordingly for the inequality,  $\sigma_r^2 \gg 2\pi\sigma_f^2$ , to be true. The coherence length can be chosen according to the source that needs to be simulated. In order to make the computations faster, the construction of the phase screen with the random signal and its

convolution with a Gaussian function is done in the Fourier domain. This has the advantage of replacing the convolution with a simple multiplication.

In our particular case, the double slits are unidimensional and the equation 3.25 can be rewritten as:

$$|\mu_{12}| = \exp\left(-\frac{(2a)^2}{l_{cr}^2}\right), \quad (3.26)$$

where  $2a$  is the distance between the slits. This equation applies for a source which degree of coherence follows a Gaussian distribution.

#### Results

The contrast can be plotted as a function of the separation between the slits. The curves for both simulation and analytical results for the double slits design of section 3.5.1 are shown in Fig. 3.9. The slits are  $1 \mu\text{m}$  wide and have  $3.2 \mu\text{m}$  of separation. The simulation of the interference resulting from the double slits is done with the random phase screen method. The results are very similar to those presented with the multiple screen superposition method in Fig. 3.6. The evaluation of the contrast is as well made by taking the Fourier transform, as presented in section 3.4. The difference is that, in the model with the phase screens, the parameter given is the coherence length, where as in the model with the superposition of plane waves, it is the angular extent of the light source that is given as parameter.

In Fig. 3.9, both curves show a very good agreement. Obviously, the larger the coherence length, the higher is the contrast. It is interesting to note that, for this particular design, the zone with the best sensitivity is below  $30 \mu\text{m}$  of coherence length. In this region, the slope is the highest, meaning that variations of spatial coherence results in large difference in contrast. For values larger than  $30 \mu\text{m}$ , the difference of contrast is small for a large difference in the coherence length.

What is interesting to simulate with this method is a multi slits approach. Indeed, as the coherence length is determined as a parameter it is interesting to be able to observe the changes in the contrast of the fringe for different coherence lengths. This simulation requires a size of the source plane of  $0.2 \text{ mm}$  with 3000 samples. This determines the size of the random screens as well. The number of screens needs to be at least 100 to ensure a correct result. Some of the results are shown in Fig. 3.10. The interference patterns resulting from the simulation are shown in the left column. The profile of the interference pattern is then used to compute the Fourier transform profile. The spatial frequency on the axis of the Fourier transform profile corresponds to the spatial frequency of the interference pattern in the observation plane. As seen in the results of the section 3.5.1, a pair of slit with a given separation results in an interference pattern that has a given frequency in the observation plane. A pair of slits that has

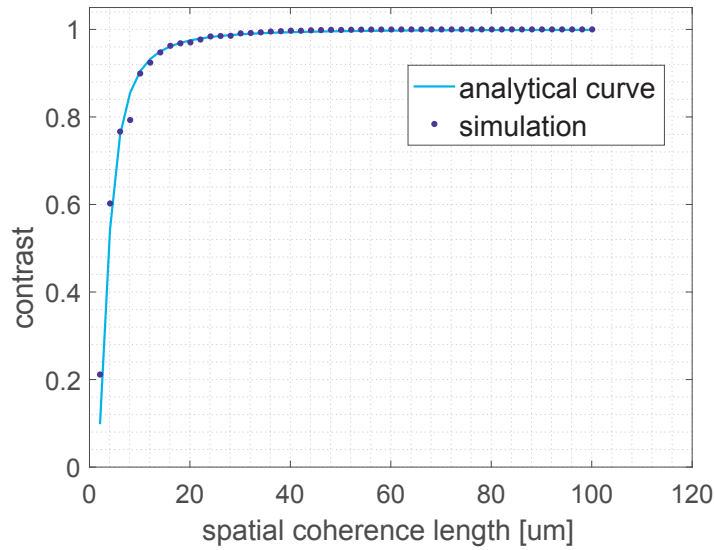


**Figure 3.9** – The contrast as a function of the spatial coherence length at a wavelength of 405 nm and with slits of 1 μm with  $2a = 3.2 \mu\text{m}$ . The analytical curve is computed using Eq. (3.26) and the simulation using the random phase screens method.

a large separation (i.e a low frequency in the source plane) results in an interference pattern with a high frequency and vice versa. The last visible peak has the written slits separation indicated on top. For the top images, the slits separated by 31 μm are still interfering. This means that the coherence length in this case is much larger than 31 μm. For the case in the middle, the coherence length is set to 8 μm, and the last peak with a contrast at 0.2 represents the frequencies generated by the slits separated by 8 μm. For the bottom case, the last peak with a contrast above 0.2 is at a frequency corresponding to a separation of the slits of 2 μm. by making a linear approximation, it corresponds quite well to the 3.5 μm set as coherence length in the simulation.

### 3.6. Simulating the spatial coherence

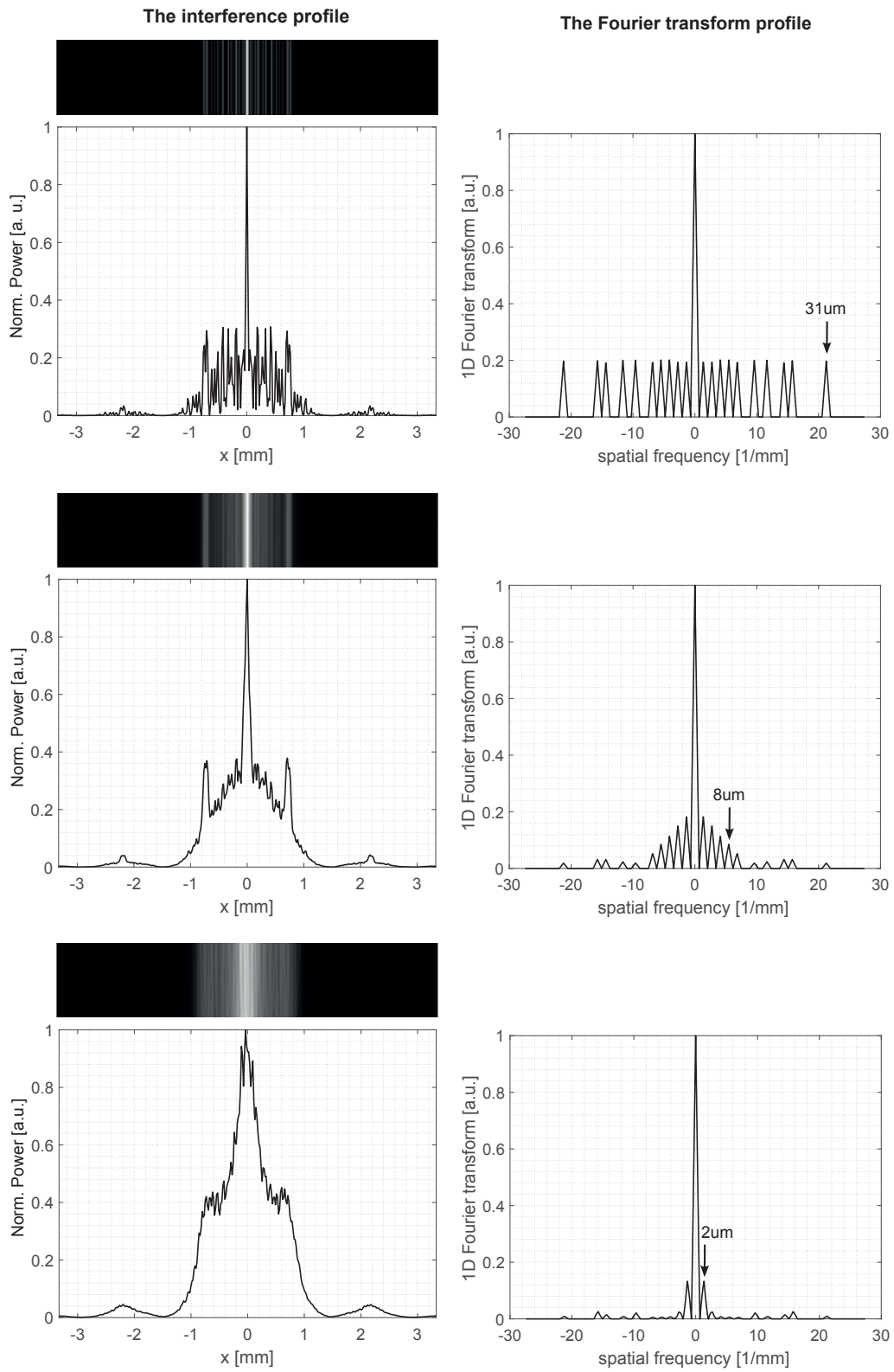


**Figure 3.10** – The simulation of the interference pattern for  $1 \mu\text{m}$  multi slits with different separations. The spatial frequencies are those found in the interference pattern in the observation plane. The coherence length of the source is set to: top)  $\gg 31 \mu\text{m}$ , middle)  $8 \mu\text{m}$ , bottom)  $3.5 \mu\text{m}$ .

### 3.6.3 Comparison of the two models

In the case of the first model, the “plane waves superposition method” is a superposition of the interference patterns produced by plane waves with a different incidence direction, i.e. a different phase. In the second model, the “random phase screens method”, the source is a superposition of waves with different randomly attributed phases, which are correlated by a Gaussian distribution. A given number of waves are computed and their resulting interference patterns are superposed. In the end, the two models are quite similar. They admit different input parameters, with the plane waves superposition method requiring an angular distribution and the random phase screens method requiring a coherence length.

By making use of the two simulation methods and the analytical results expressed, the angle of the source can be put in relation with its coherence length. This is done by combining Eq. (3.20) and Eq. (3.26):

$$2 \cdot J_1 \left( \frac{\pi \theta 2a}{\lambda} \right) / \frac{\pi \theta 2a}{\lambda} = \exp \left( - \frac{(2a)^2}{l_{cr}^2} \right). \quad (3.27)$$

This means that the spatial coherence length  $l_{cr}$  can be expressed as a function of the angular extent  $\theta$ :

$$l_{cr} = \sqrt{-(2a)^2 \cdot \ln \left( 2 \cdot J_1 \left( \frac{\pi \theta 2a}{\lambda} \right) / \frac{\pi \theta 2a}{\lambda} \right)^{-1}}. \quad (3.28)$$

This relation is shown in Fig. 3.11, where both of the scales are in log. The dark dashed lines mark the limit of the angular extent range in the mask aligner. For small angles, the relation is independent of the separation between the slits. The separation between the slits is set to 2  $\mu\text{m}$ , as it corresponds to the smallest  $2a$  of the apparatus used for the measurements presented in the Chap. 4. It is this distance which limits the measurement of the spatial degree of coherence of sources with a large angular extent. The wavelength is set to 405 nm, because it is the wavelength that is used for the measurement. Examples of angular extent to coherence length relation are shown with the blue dashed lines. An angle of 0.1° corresponds to a coherence length of 200  $\mu\text{m}$ , an angle of 0.7° to a coherence length of 30  $\mu\text{m}$  and an angle of 5° to a coherence length of 4  $\mu\text{m}$ .

This relation is presented in a slightly different manner from the one theoretically established by Wolf and Carter in their work [45], where they present a far more general approach. It should be possible to directly deduce Eq. (3.28) from the relation established in the paper.

Concerning the limits of validity, in the random phase screen superposition method, which



gives the coherence length as a function of the separation of the slits, the coherence is modeled by a Gaussian distribution, meaning that the resulting degree of coherence follow a Gaussian distribution. This means that, the validity of the relation of Eq. (3.28) is ensured for light sources which present a spatial degree of coherence close to a Gaussian distribution. Another limit of validity is that, for Eq. (3.20) to be valid, the source should be circular and in the far-field and the width of the apertures very small compared to their separation. As mentioned above, the slits are large compared to their separation, which means that some variations can be observed.

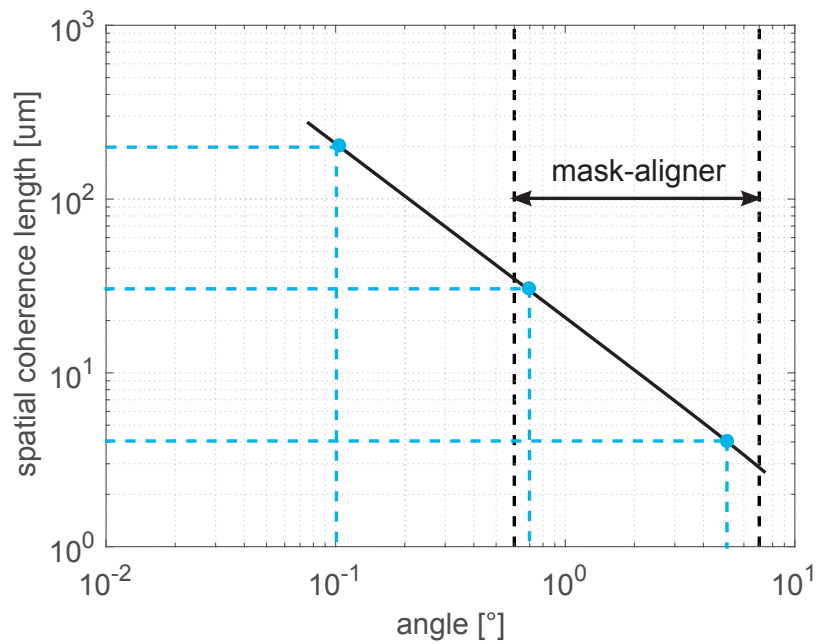


**Figure 3.11** – The spatial coherence length as a function of the angular extent of the light source for a wavelength of 405 nm and  $2a = 2 \mu\text{m}$ . The dashed lines delimit the angular range in the mask-aligner. The blue lines indicate examples of values.



## 4 Measurement of the degree of spatial coherence

This chapter focuses on the experimental measurement of the spatial degree of coherence. First, a test setup, which allows to adjust the angular extent of a source is used. This allows to confirm the relation between the spatial degree of coherence and the angular extent, by measuring the contrast of the interference pattern produced by double and mutli slits. Then, measurements are made in the mask plane of a MA/BA 8 Gen3 SUSS mask-aligner. The spatial degree of coherence for different illumination patterns is measured with the double slits. For a well-chosen pattern, the variation of the degree of coherence across the mask plane is investigated. The degree of coherence is then measured for bi-dimensional directions with a circular double slits design. Finally, test prints with different illumination patterns which illustrate the importance of the angular distribution are shown.

### 4.1 The degree of spatial coherence of different light sources

The relation between the angular extent and the spatial coherence length found in the previous part needs to be confirmed experimentally. To do so, a test setup is mounted to make measurements with the double slits and the multiple slits configurations. The test setups allows to adjust the illumination angle at will, while measuring the resulting interference patterns. The angular extent can also be measured with a pinhole apparatus.

#### 4.1.1 Setup

In order to validate the concept, the double slits interference pattern is recorded for light sources of different degrees of spatial coherence. A diode laser at 405 nm with a high coherence and the 2x2 LED system at 405 nm with a variable coherence are tested. The light emanating from the laser is simply collimated with a collimation angle of about  $0.8^\circ$ . The LEDs are placed as depicted on the schematic of Fig. 4.2. The intensity coming out of the reflector is quite homogeneous, therefore a lens is used as a Fourier lens, to transform the intensity into a homogeneous irradiance on a diffuser plate. The diffuser creates a source which emits quite

## Chapter 4. Measurement of the degree of spatial coherence

uniformly in a large angular range of  $\pm 15^\circ$ . It is followed by an aperture, which allows to select the size of the source and therefore its angular extent, depending on the distance between the aperture and the measurement plane. The spatial coherence of the LED illumination system can be modified by changing the size of the aperture.

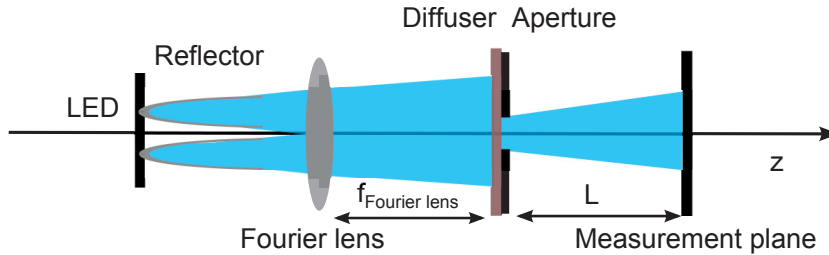


**Figure 4.1** – A schematic of the setup used to measure the interference pattern for  $1\ \mu\text{m}$  double and multi slits and the angular extent.

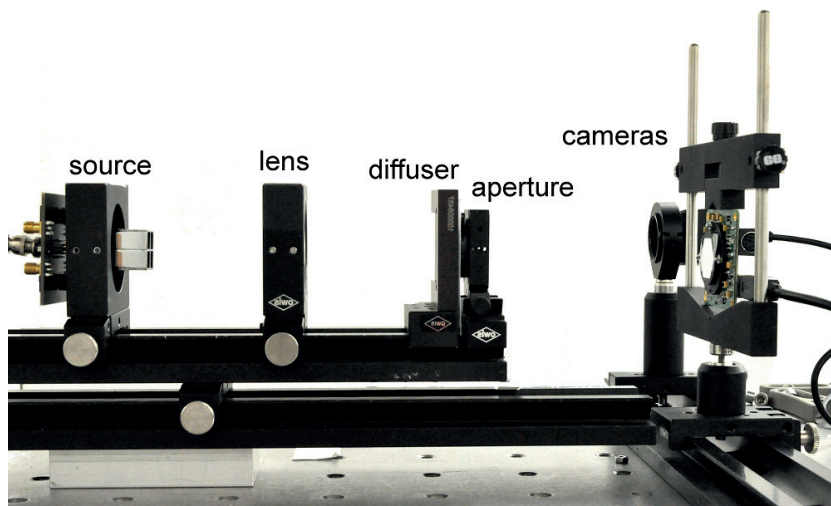


**Figure 4.2** – A photograph of the setup used to measure the interference pattern for  $1\ \mu\text{m}$  double and multi slits and the angular extent.

Three measurements are made in the indicated measurement plane, divided into two sets. Two cameras are mounted on a rail to pass easily from one to the other. They are shown in Fig. 4.3 and 4.4. The first camera is used to measure the interference pattern. The measurement is first done with the double slits design and is then repeated with the multi slits design. In both cases, the slits consist in an amplitude mask on a glass substrate with the opaque regions in aluminum. It was replicated using contact lithography from a chromium mask and diced to have polygons of 2.5 cm. The measurements were, at first, tried out directly with a chromium mask, but the layer was letting 0.01% of the light through. The consequence was the apparition of extra fringes due to the interference of the light going through the slits and of the light going through the chromium part.

#### 4.1. The degree of spatial coherence of different light sources

The system is very compact and is adapted to fit in the limited space of the mask-aligner. The slits on the piece of mask are mounted at a distance of 3.6 mm from the sensor. In order to do so, the camera needs to be removed from its housing and a special 3D printed adapter is set into place. The adapter allows for a proper positioning of the hexagon with a corresponding groove. The mask piece is taped to avoid any movement. The assembly is shown in the picture of Fig. 4.3.

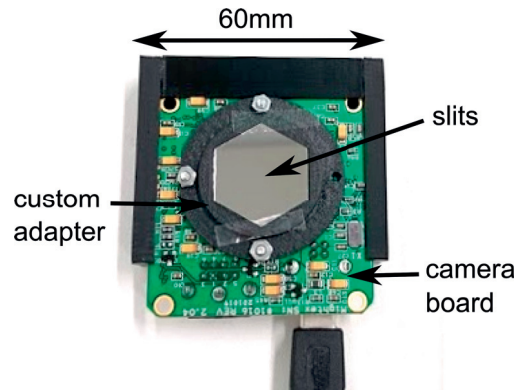


**Figure 4.3** – The camera and the slits for the measurement of the coherence in the mask-aligner. The double-slits are mounted 3.6 mm away from the sensor, using a custom piece.

The second camera is used to double check the angular distribution for both sets of measurement. This measurement is done with a pinhole. The assembly is presented in Fig. 4.4.

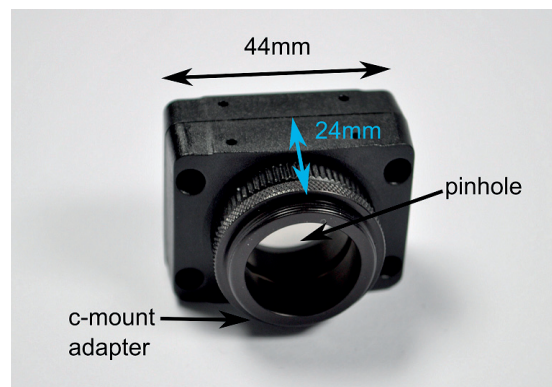


**Figure 4.4** – The camera used for the angular extent measurement. The pinhole is mounted 24 mm from the sensor, using a c-mount adapter.

For the measurement of the angle with a pinhole, the size of the pinhole should be small enough to give a good precision of measurement, but large enough to avoid diffraction effects. In the end, a pinhole of 100  $\mu\text{m}$  is put in front of the camera with a distance to the sensor of  $24 \pm 1$  mm. The angular extent is also given by the size of the aperture in front of the diffuser and its distance to the measurement plane. When the light coming out of the aperture is considered as a point source, the angle of the light reaching the measurement plane is

geometrically given by:

$$\theta = \arctan\left(\frac{a}{2L}\right), \quad (4.1)$$

where  $a$  is the aperture size and  $L$  its distance to the measurement plane. As the uncertainty over the pinhole size is very small compared to the uncertainty over the distance between the pinhole and the sensor of the camera, the error on this measurement is given by:

$$\begin{aligned} \Delta\theta &= \left| \frac{\delta\theta(a,L)}{\delta a} \right| \Delta a + \left| \frac{\delta\theta(a,L)}{\delta L} \right| \Delta L = \left| \frac{2L}{a^2 + 4L^2} \right| \Delta a + \left| -\frac{2a}{4L^2 + a^2} \right| \Delta L \\ &\approx \left| \frac{1}{2L} \right| \Delta a + \left| \frac{a}{2L^2} \right| \Delta L \approx \left| \frac{a}{2L^2} \right| \Delta L \end{aligned} \quad (4.2)$$

#### 4.1.2 Results

The system is first used to measure the interference patterns with the double slits apparatus. Some of the results are shown in Fig. 4.5. Both the interference profile and its Fourier transform are shown. The spatial frequencies in the Fourier transform graphs are the spatial frequencies of the interference pattern in the observation plane, i.e. the sensor of the camera. With the increase of the size of the aperture and thus of angular extent, the contrast diminishes. The pictures with the lowest contrast represent the limit of what can be measured with the slits used. The measurements are repeated for different angles and the interference pattern and the angle are measured each time.

The measured values of contrast as a function of the angular extent of the source are plotted as a curve. The results can be compared with the simulation and the analytical results in Fig. 4.6. It can be seen that the measurements fit quite well the theory. The measurements do not reach a contrast as high as what is theoretically expected. There are different possible explanations for this. In the case of the laser, a diode laser is not a monomode laser source, which means that it is not fully spatially coherent. In the case of the LED, with smaller apertures, the intensity level of the light reaching the detector was weaker, thus the signal over noise ratio was not as good, decreasing the measured contrast. Another explanation could be the fact that the LEDs has a FWHM (full width at half maximum) bandwidth of 10 nm. This will result in a decrease of the contrast as the different wavelengths are diffracted with a different angle [46]. A last thing to observe is that it looks like the LED measurement are “saturating” to a contrast lower than 0.8. From the curve of Fig. 3.9, this correspond to a coherence length of about 25  $\mu\text{m}$ . This could be limited by the diffuser used to produce the light field.

#### 4.1. The degree of spatial coherence of different light sources

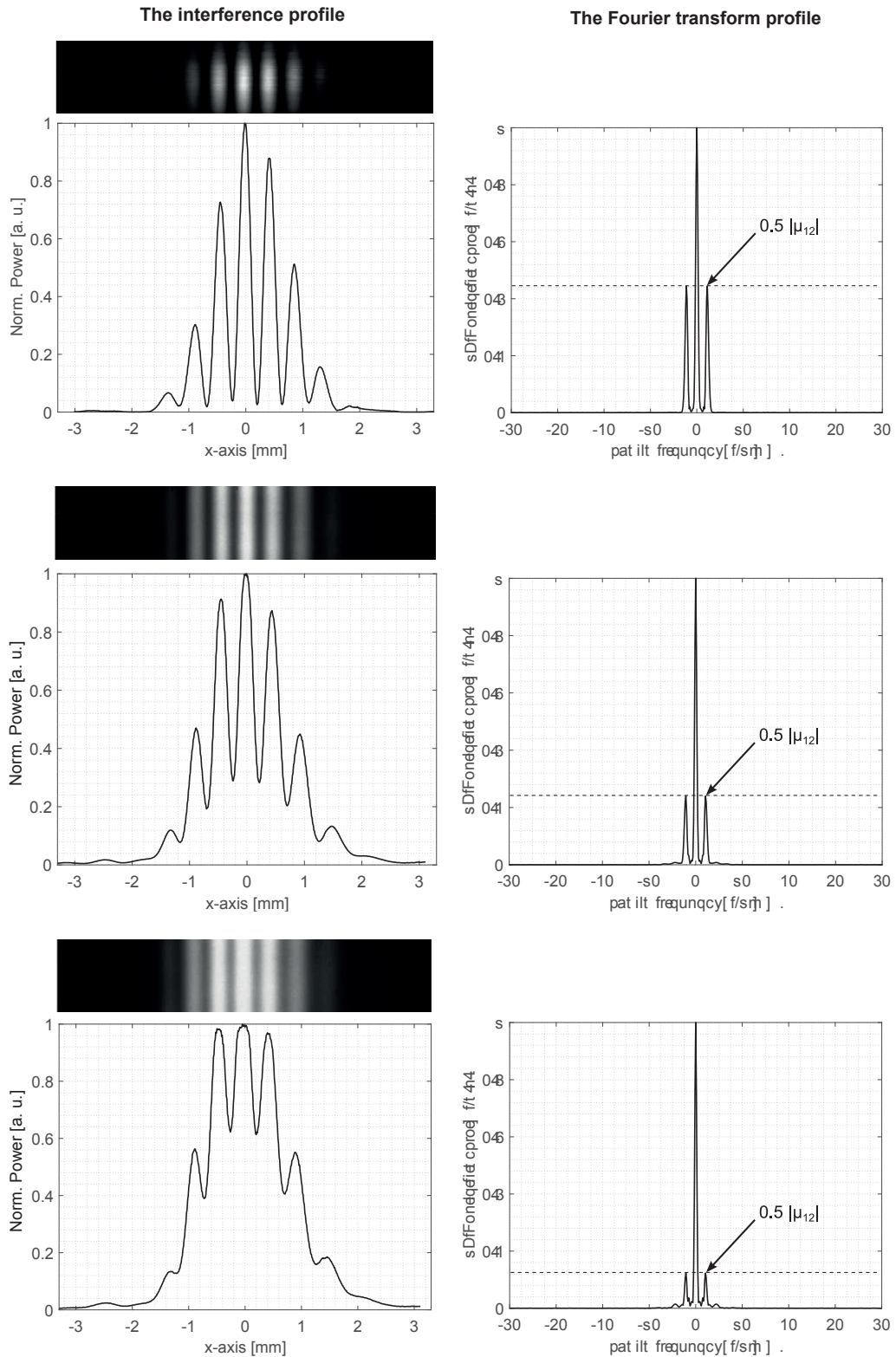


**Figure 4.5** – The measurement of the interference pattern for  $1 \mu\text{m}$  slits with  $3.2 \mu\text{m}$  separation and a propagation length of  $3.6 \text{ mm}$ , at  $405 \text{ nm}$ . The incoming angles and resulting contrast are (top)  $\pm 0.3^\circ$ ,  $\mu_{12} = 0.9$ , (middle)  $\pm 2.2^\circ$ ,  $\mu_{12} = 0.49$ , (bottom)  $\pm 3.1^\circ$ ,  $\mu_{12} = 0.24$ .

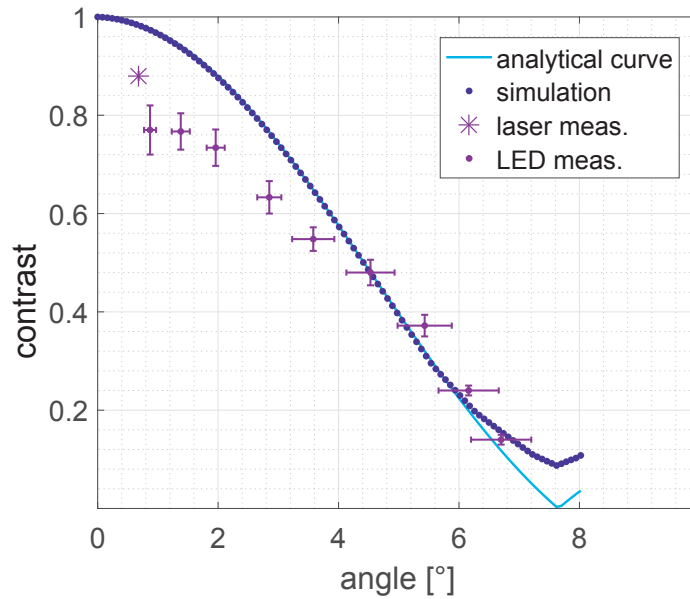


**Figure 4.6** – The contrast as a function of the spatial coherence length

The same measurement procedure is applied to acquire the measurements with the multi slits apparatus. Some of the results of the measurements are shown in Fig. 4.7. The same decrease in contrast can be observed with the increase of angular extent. Some of the frequencies even disappear, meaning that the coherence length is shorter than the slits separation corresponding to those frequencies. In order to determine the degree of coherence, the last peak with a contrast of 0.2 is considered. The position of the peaks corresponds to a given pair of slits with a given separation. It is this separation between the slits which gives the spatial coherence length of the light. Most of the times it corresponds to the last noticeable frequency. When the last visible peak has a contrast superior to 0.2, a linear interpolation is made between this peak and the next one to find for which slit separation the contrast is 0.2. This gives an error on the measurement, but the slits separation are short enough for it to be acceptable.



#### 4.1. The degree of spatial coherence of different light sources

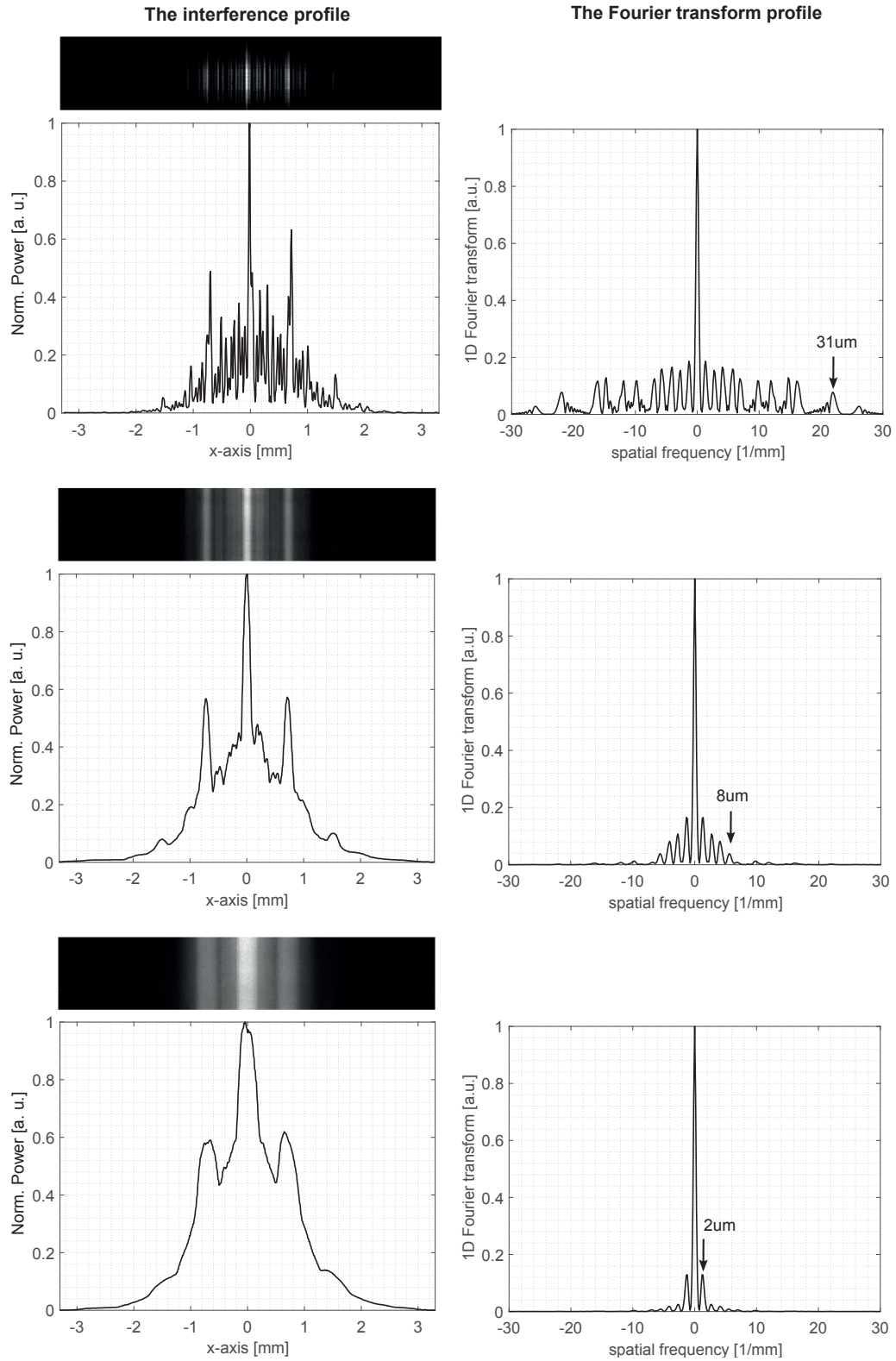


**Figure 4.7** – Measurements of the interference pattern for  $1 \mu\text{m}$  multi slits. The incoming angles and resulting coherence length are (a), (b)  $\pm 0.3^\circ$  and  $l_{CR} > 31 \mu\text{m}$ , (c), (d)  $\pm 1.3^\circ$  and  $l_{CR} = 8 \mu\text{m}$ , (e), (f)  $\pm 3.1^\circ$  and  $l_{CR} = 3.5 \mu\text{m}$ .

## Chapter 4. Measurement of the degree of spatial coherence

The measurements of the spatial coherence as a function of the angle are plotted in Fig. 4.8. They correspond to the analytical curve given by Eq. (3.28). The scale are both in a logarithmic scale. The agreement between the measurement and the analytical curve is very good. This demonstrate that the setup used for the measurement ensure that the limits of validity of the equation are respected.

This curve is very useful to pass from the angular distribution of a light source to its coherence length. Depending on the case considered, it might be easier to measure interference fringes than to measure an angular distribution. This can be the case when the angular distribution is very small. It can be difficult to measure it properly by using a lens or a pinhole. In this case, measuring the contrast of the interference fringes can be a more precise and compact solution. The contrary can also be true, especially for large angles, which result in small spatial coherence length. In this case it is easier to measure the angular extent of the source, as the coherence length is very small, and the slits needed to measure it would need to be very close to each other. This relation could be used to improve lithography with mask-aligner. This gives valuable information for the optimization of masks. It is interesting to know if two apertures are within the coherence length of the illumination light or not. In proximity printing, this determines if the light going through two apertures will interfere or not and with what level of contrast. This is of particular interest in the case of OPC (optical proximity correction) masks. Of course, for such an application, the source is not always circular, and the curves would need to be adjusted accordingly.

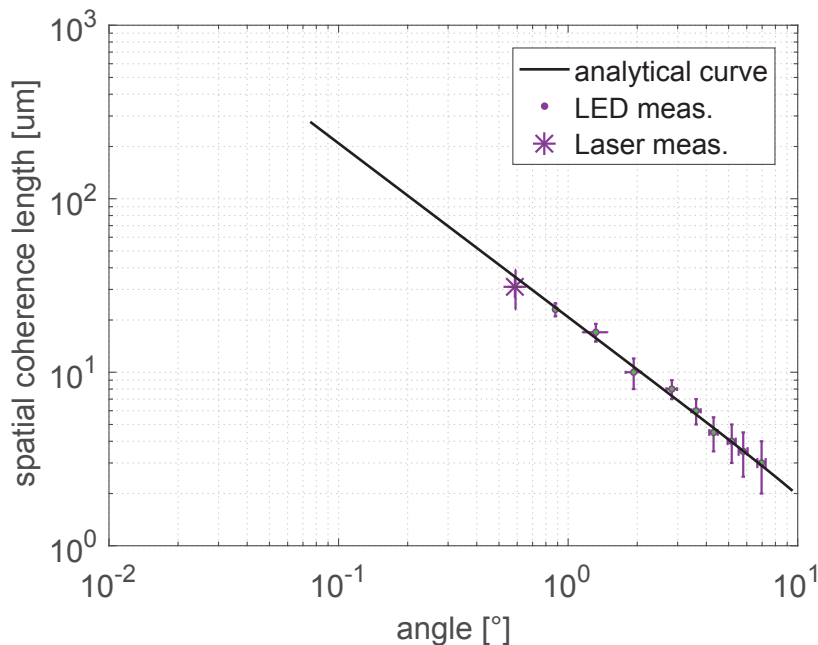


**Figure 4.8**– The spatial coherence length as a function of the angle at 405 nm and slits separated by 2 μm.

## 4.2 The degree of spatial coherence in a mask-aligner

The final goal is to measure the angular distribution and coherence properties in the mask-aligner with the 7 x 7 LEDs illumination system described in Chap. 2. Different measurements are made to determine the degree of spatial coherence for different patterns, for different position in the mask plane and for different orientation of the slits.

### 4.2.1 The degree of spatial coherence for different illumination patterns

As explained in the description of the system, the angular distribution is determined by the pattern on the Fly's eye integrator. In Fig. 4.9, the left picture shows the irradiance on the fly's eye integrator. It is the pattern created by the LEDs. Each color represent a group of LEDs, which can be switched on independently. The second part of the figure shows the angles in the mask plane. The irradiance distribution on the fly's eye integrator is transformed by the optical system into a local angular pattern. The optics of this mask-aligner is the same as presented in Fig. 1.7 of section 1.4.2. The only difference is that the beam is folded by two mirrors. The measurements with the double slits design of  $1\ \mu\text{m}$  slits and  $3.2\ \mu\text{m}$  of separation are done in the mask-aligner for the different illumination patterns. The measurements are also made with different orientations of the slits. For the measurements at  $0^\circ$  the slits are oriented along the direction indicated by the  $0^\circ$  arrow. The measurements at  $45^\circ$  are done with the slits oriented along the arrow at  $45^\circ$ . This changes the orientation of the slits with regard to the orientation of the angular distribution.

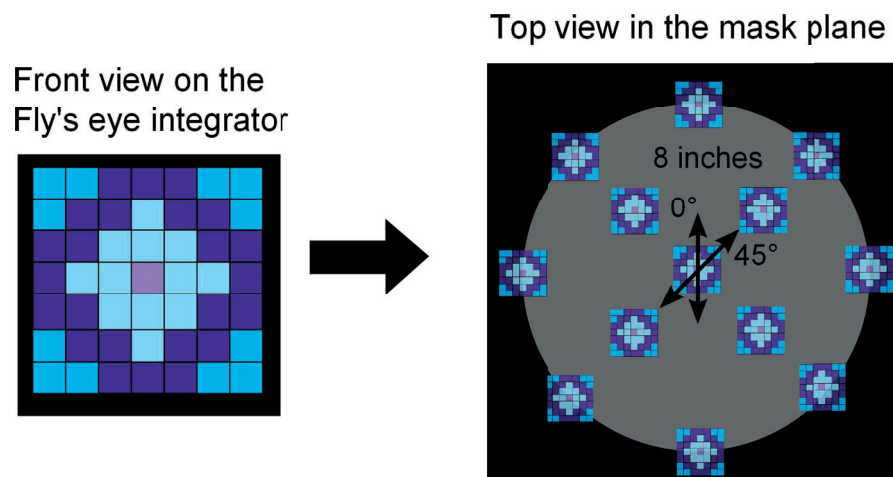


**Figure 4.9** – The left part shows the irradiance on the fly's eye integrator. This irradiance is transformed into a local angular distribution in the mask plane.

The results are summarized in the table 4.1. The column on the left indicates which pattern is measured. Some of them have the corners cropped. This vignetting is due to the optics following the fly's eye integrator. The second column gives the name of the pattern. The next column gives the corresponding angular extent. The angular extent is found by calculation





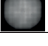
## Chapter 4. Measurement of the degree of spatial coherence

from the size of the pattern on the fly's eye integrator and the optics leading to the mask plane. It is also measured with a pinhole camera in the mask plane, for confirmation. The last two columns show the contrast of the fringes measured with different slits orientation. For some of the patterns, both 0° and 45° configurations are measured.

It can be observed that, overall, the illumination pattern with the single center LED results in the highest degree of spatial coherence. This is consistent with the fact that the resulting angular extent is very small, about 1.6° of full angle. The small ring presents the second highest degree of coherence, once again without surprise. The facts that the large ring has the lowest degree of coherence and that the 7x7 LEDs pattern has a higher degree of coherence are more difficult to explained. This shows the limit of the measurement with double slits, as the angular distribution is in 2D. With the double slits, only the direction transversal to the slits is being measured.

As presented in the previous section, the angular extent directly corresponds to a coherence length. The center LED, for example, has the longest spatial coherence which can be deduced from the graph to be of 25 μm. This is an interesting information which is useful when printing structures. For structures on the mask which are separated by more than 25 μm, the light going through the aperture will not interfere in the far field. The spatial coherence length of the other patterns are smaller than that. The relation between the angular extent and the coherence length is unfortunately less obvious for more complicated patterns.

**Table 4.1** – Contrast measurement in the mask-aligner

| Pattern   | Pattern    | angular extent ± 0.1 [°] | contrast at 0° | contrast at 45° |
|---|------------|--------------------------|----------------|-----------------|
|  | center LED | 0 - 0.8                  | 0.739          | N.A.            |
|  | small ring | 0.2 - 4.4                | 0.475          | 0.466           |
|  | large ring | 3.5 - 7                  | 0.129          | N.A.            |
|  | corners    | 5.8 - 7                  | 0.225          | 0.045           |
|  | 7x7 LEDs   | 0 - 7                    | 0.181          | 0.195           |

### 4.2.2 Uniformity of the degree of spatial coherence across the mask plane

In order to check the uniformity of the coherence over the mask plane, the measurement for the small ring pattern is repeated in thirteen points across the mask plane. The chosen positions are the same as previously for the irradiance uniformity measurement. The small ring pattern is chosen because it has a contrast close to 0.5. This means that, the sensitivity around this measurement is the highest because the curves of Fig. 4.6 show that it is the point with the highest slope. Therefore, small variations of coherence can be measured. The results are summarized in Fig. 4.10. The variations of the coherence measurements across the plane are within 1.2±0.2%. The positions where the lowest degree of coherence measurements are recorded are indicated in purple, those with the highest are in blue. The region on the right

## 4.2. The degree of spatial coherence in a mask-aligner

side of the mask plane shows less coherence than the region on the left side. The same kind of distribution is found for the irradiance uniformity in Chap. 2. This likely indicates that the optics suffers from misalignments and aberrations which are also affecting the local angular distribution of the light. This affects the aerial image produced and thus the structures printed in the resist. Such information is useful to adjust the optics of the mask-aligner. It can also be used to have an adequate repartition of the structures over the mask. The structures which give a better print quality with a higher level of coherence can be placed where the measured degree of coherence is the highest.

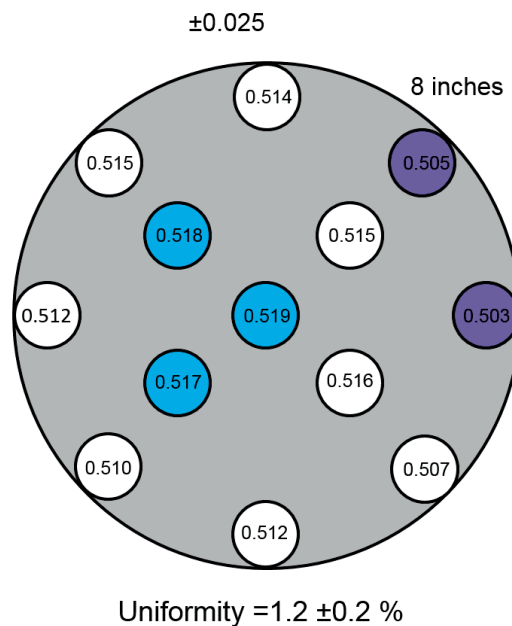


**Figure 4.10** – The uniformity of the spatial degree of coherence. The measured uniformity of the measurements across the plane is  $1.2 \pm 0.2\%$ . The spots with the lowest degree of coherence are indicated in purple, whereas those with the highest are in blue. The region on the right of the mask plane shows less coherence than the region on the left, which probably indicates a misalignment of the optics. The pattern is consistent with the uniformity measurement of Chap.2.

### 4.2.3 Variation of the degree of coherence with the orientation of the slits

In the table 4.1, the results obtained for the measurements done with a rotation of  $45^\circ$  of the double slits can be compared to those done with the slits at  $0^\circ$ . For this investigation, two patterns which are close to rotational symmetric and one which is not are chosen. The two patterns which are rather symmetrical are chosen because they have a contrast for which the sensitivity of the measurement is good, as their contrast is close to 0.5. It can be seen, that not all the patterns are affected in the same way. The patterns which are rather symmetrical, like the small ring and the 7x7 LEDs, show little difference between the two measurements. On the other hand, the measurements done with the corner pattern show an important

## Chapter 4. Measurement of the degree of spatial coherence

difference between the two measurements. Figure 4.11 shows the coherence measurement for two different slits orientation. It is clear from the measurements that the contrast is much higher for the  $0^\circ$  measurement. This is an important point, as it shows that, for mask-aligner illumination the coherence is not always consistent in 2D. This is a key element when printing structures which have spatial frequencies that vary in the plane. Therefore, a simple measurement with a double slit, or an array of pinholes, like presented in most papers is not enough. A bi-dimensional method is described in the following sections.

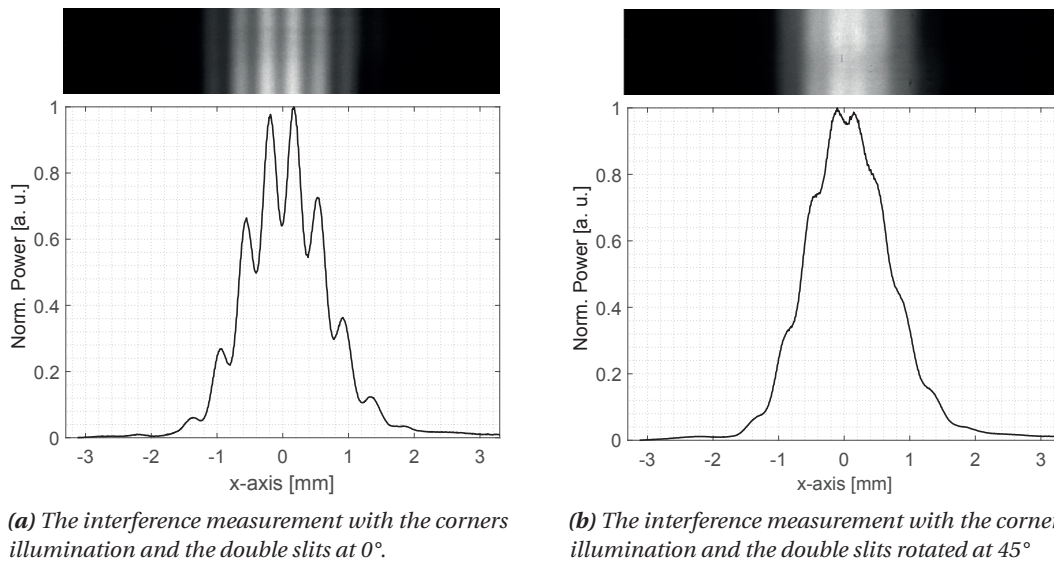


**Figure 4.11** – The interference fringes measurement for the corners illumination with double slits of  $1\ \mu\text{m}$  with  $3.2\ \mu\text{m}$  between the centers. In (a), the slits are at  $0^\circ$  and in (b) the slits are rotated by  $45^\circ$ . The contrast is greater for the measurement with the slits at  $0^\circ$ , indicating a higher degree of coherence.

### 4.3 2D spatial coherence measurement with circular double slits

In order to properly measure the spatial coherence in the mask plane for different illumination patterns, a method has to be developed for a bidimensional measurement. A method to measure the spatial coherence of superluminescent diodes in two dimensions is presented by Hitzenberger et. al. in their work [47]. The method is very accurate and allows the mapping of the spatial coherence of a source. The only drawback is that it is based on a rather complex and bulky system which is also sensitive to vibrations. This method would therefore be difficult to implement for the measurement of the spatial coherence in the mask plane of a mask-aligner.

The proposed solution is still based on the double slit approach. In order to be able to measure the degree of coherence in 2D, a rotationally symmetrical adaptation of the double slits is developed. By shaping the double slits into circles, as presented in the schematic of Fig. 4.12, the degree of coherence along the different directions can be seen visually. The same design of slits is chosen, with  $1\ \mu\text{m}$  slits and  $3.2\ \mu\text{m}$  between the centers, which allows to measure the different angles in the mask-aligner. The slits are arranged on both sides of a circle with a diameter of 1 mm. The circular slits are set 3.5 mm from the sensor of the camera.

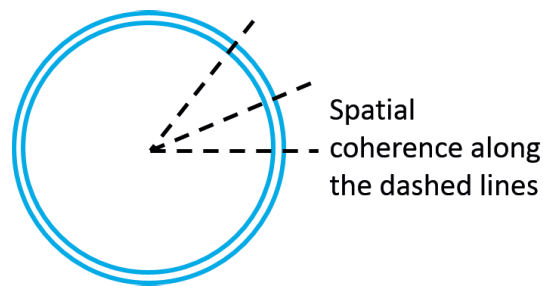


**Figure 4.12** – A schematic of the 2D spatial coherence measurement principle. The contrast can be measured along all directions.

The measurements are done in the mask plane with the different illumination patterns. The images taken with the camera are shown in Fig. 4.13. The different patterns give different degree of coherence according to their angular extent. The rotational symmetric angular distribution patterns exhibit a quite rotationally symmetrical interference fringes pattern. This is the case for the small ring in Fig. 4.13 (c) and the large ring illumination in Fig. 4.13 (d). Those patterns also have part of the angular spectrum that are not rotational symmetric, which result in darker lines along the  $0^\circ$ ,  $45^\circ$  and  $90^\circ$  directions. The  $7\times 7$  LEDs illumination in Fig. 4.13 (a) also shows a rather symmetrical and homogeneous pattern. It is worth noticing that the corners of the illumination are cropped by the lens following the fly's eye integrator, thus making the pattern rotational symmetric. The non-symmetric angular spectrum have a different degree of coherence depending on the direction. This is especially visible with the corners illumination pattern in Fig. 4.13 (e). One can see that there are directions along which the contrast of the fringes is much smaller than along others. There are also high frequency fringes along the circles. Those frequencies are most probably artifacts due to the fact that the circles are not perfect circles. They are made on the mask with e-beam lithography and thus

## Chapter 4. Measurement of the degree of spatial coherence

---

made of segments, which intersections introduce the additional frequencies.

Something else to notice is the angular distribution is imaged in the center of the pattern. The design is thought in such a way that the light coming from two opposite sides of the circle should not meet in the middle. A fabrication error in the 3D printing of the adapter for the camera increases slightly the propagation distance, thus leading to the light reaching the middle of the camera. The slits then act as a imaging system like a pinhole camera, but with selective part of the light reaching the sensor. The result is a blurred image of the angular distribution. One can still identify that the center LED is much smaller than the others, that the large ring presents a hole in the center, that the small ring is actually more of a small circle and that the corners are imaged as four spots. This feature of the system actually gives an additional information, as the angular extent can be measured on the same image as the bidirectional interference pattern.



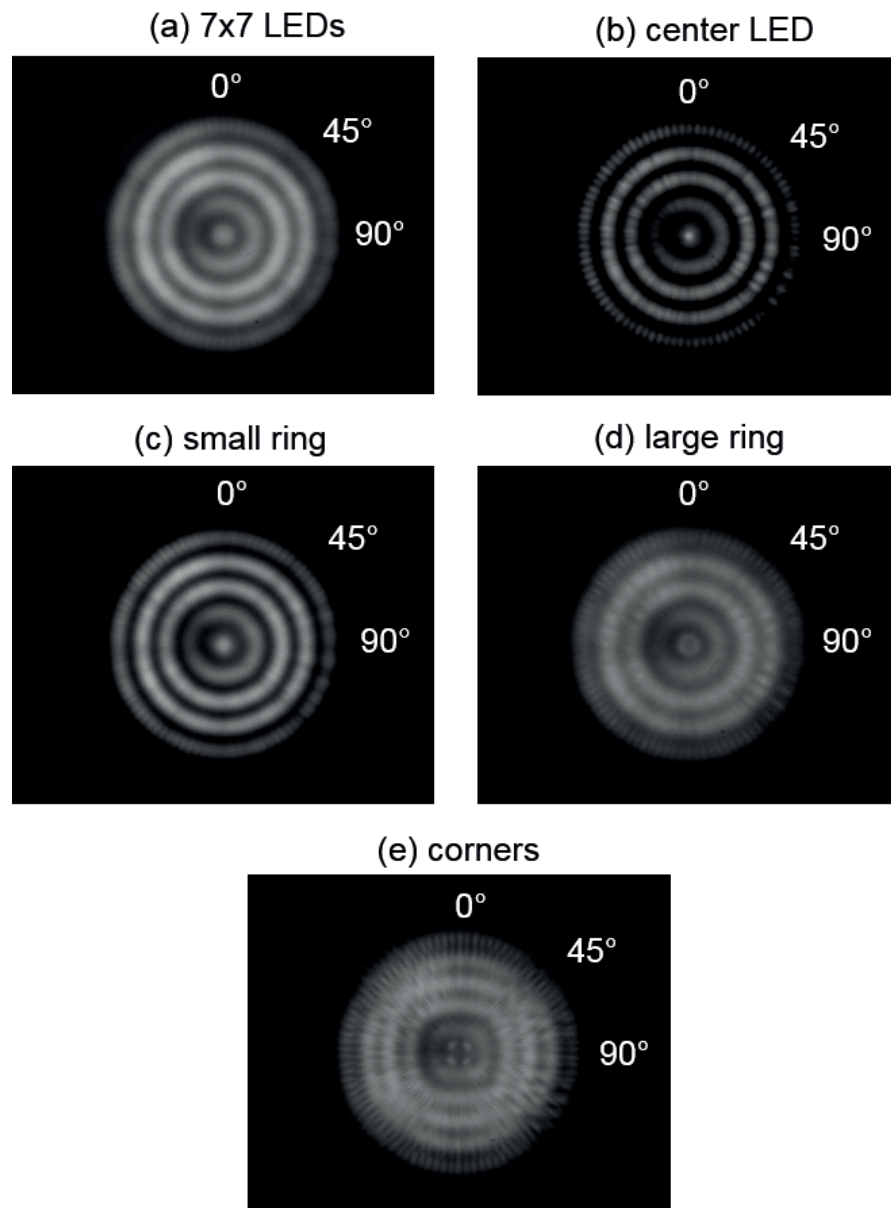


**Figure 4.13** – The measurement of the circular double slits for different illumination patterns. The differences in the degree of coherence are clearly visible, both in terms of contrast and orientation.

#### 4.4 Print tests with different spatial coherence lengths

The impact of the angular distribution and the spatial degree of coherence on real prints is investigated. An amplitude mask consisting in a grating of squares of  $4\ \mu\text{m}$  of width with a pitch of  $8\ \mu\text{m}$  along both directions is replicated in a layer of photoresist. The design is shown in the schematic of Fig. 4.14. The prints are made in a layer of  $1\ \mu\text{m}$  of AZ1518 resist, deposited on 4 inches silicon wafers. The wafers are exposed to a dose of  $63\ \text{mJ}/\text{cm}^2$  at  $30\ \mu\text{m}$  of proximity gap. The development is done for 45 seconds in AZ351B 4/1 from AZ Electronic Materials.

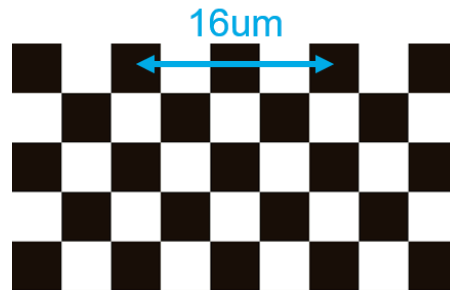


**Figure 4.14** – The design of the grating with the square lattice. It is an amplitude mask. The width of the square is  $4\ \mu\text{m}$  and the pitch is  $8\ \mu\text{m}$ .

The structures in the photoresist are shown in Fig. 4.15. They all exhibit the same period, but there are noticeable differences between the printed structures. This is explained because the light field behind the mask changes according to the angular distribution of the light reaching the mask. For example, with the  $7\times 7$  LEDs illumination in Fig. 4.15(a), the printed patterns are rather round where as with the center LED illumination in Fig. 4.15(b), the printed patterns are rather squared. In Fig. 4.15(e), four spots are printed, which resemble the corners illumination pattern. The printed spots are smaller than the  $4\ \mu\text{m}$  structures on the mask.

This property is exploited in resolution enhancement techniques and is, for example, applied by Stuerzebecher et. al. in [48] and by Harzendorf et. al. [49]. The illumination system is described as a set of mutually incoherent plane waves which are tilted, similarly to what is presented above for the simulation. Arriving on the mask, the distribution pattern on the fly's eye integrator is transformed into the angular distribution, which can be modeled as the optical Fourier transform of the light emission. The light then reaches the mask, which is actually an array of holes. The light is then diffracted over the proximity gap distance. It is shown, in the paper, that the resulting diffraction pattern is close to a convolution of the angular distribution in the mask plane with a periodical point spread function.

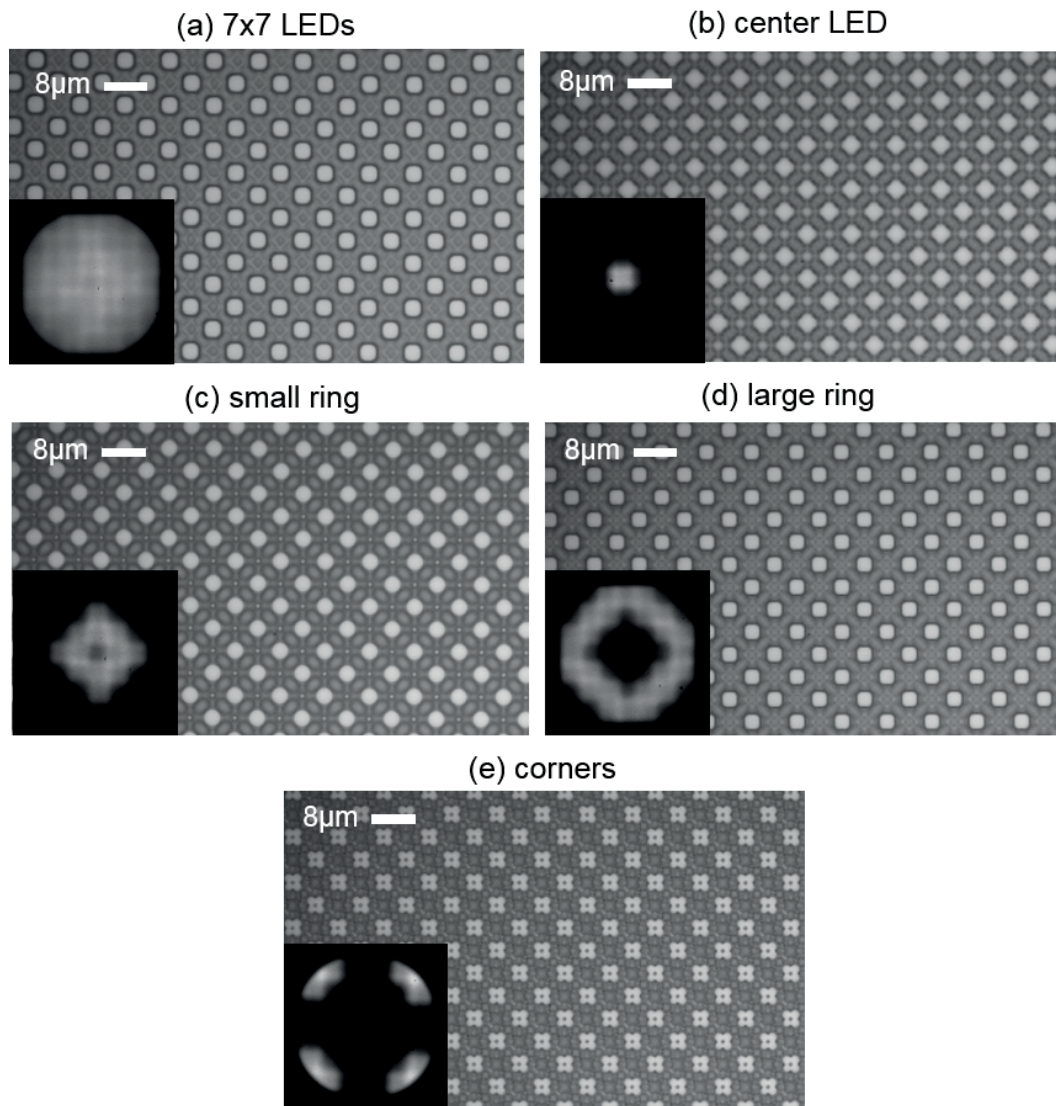


**Figure 4.15** – Microscopic measurements of a printed grating of  $4\ \mu\text{m}$  with a pitch of  $8\ \mu\text{m}$ . The prints are done at a proximity gap of  $30\ \mu\text{m}$ . The different illumination patterns result in very different printed structures, illustrating the importance of the angular distribution of the exposure light.

This kind of phenomenon leads to the so-called “Talbot effect”. The distance of the fractional Talbot planes from the mask is given by:

$$g_{TB} = 2 \frac{p^2}{\lambda} \frac{N}{n} \quad N, n \in N \quad \frac{N}{n} \notin \text{for } N, n > 1 \quad (4.3)$$

where  $p$  is the pitch of the array, in this case,  $8 \mu\text{m}$ ,  $\lambda$  is the wavelength of the illumination light which is  $365 \text{ nm}$  and  $N/n$  is a fraction. In this case,  $g_{TB} = 350 \mu\text{m}N/n$ . This means that the main Talbot plain is at  $350 \mu\text{m}$ . A proximity gap of  $30 \mu\text{m}$ , is too far from the first Talbot plain to have an exact reproduction of the patterns. The light field changes very rapidly with distance and the uncertainty on the position of the stage is of a few microns and therefore too high to make accurate predictions. The general effect can still be observed on the results of Fig. 4.15. The angular distributions are recognizable, specially in the case of the corner illumination, where four corners can be observed. This means that the printed structures, here the four spots, are smaller than the mask features of  $4 \mu\text{m}$ . With a stage that has a very accurate positioning, this technique can be used to achieve higher resolution than with conventional proximity printing, thanks to the modifiable illumination pattern of the light source.

### 4.5 Summary

Different designs of double slits and multi slits to measure the spatial coherence are demonstrated. The design are supported by two different simulation methods. One uses the superposition of plane waves, and the other the superposition of random screens. They allow to anticipate the results of the interference of spatially partially coherent light. The double slits are allow the measurement of a light beam with an angular extend ranging from  $0.8^\circ$  to  $7^\circ$  of full angle. This corresponds to the angles in a mask-aligner. The measurements are made on a test bench. The results obtained confirm a theoretical relation between the angular distribution and the spatial coherence length. The agreement of the measurement with the analytical data is very good. This first step validates the concept. The same measurements of spatial coherence are made in the mask plane of a mask-aligner equipped with a novel LED -based illumination. The angular distribution of the illumination can be changed and the degree of spatial coherence is measured for five different angular distribution patterns. With this technique, the uniformity of the spatial coherence across the mask-plane is determined by measuring the degree of coherence at thirteen points over the mask plane. The uniformity of the degree of spatial coherence is within  $\pm 1.2 \%$ .

A novel technique of circular double slits is proposed to measure the spatial coherence in two dimensions. These measurements give a clear picture of the coherence along different axis of the angular distribution.

Print test are realized with different illumination patterns. They illustrate well the effect of the

different illumination patterns on the printed structures. They also demonstrate the possibility of realizing prints with enhanced resolution, by printing a grating with a chosen illumination pattern.

### 4.6 Possible improvements and future developments

A possible step in the coherence measurement in the mask-aligner would be to measure directly the coherence length in a bidirectional way, as with the circular double slits. That can be done with an optimized array of points, as such presented by Golay in [42] or with circular multi slits, similarly to the circular double slits. In this way, the coherence property at a certain point can be known in different directions. Such a design seems feasible, the main challenge being the analysis of the obtained data. As the results are circular, it is more difficult to average over different lines, as it is done with the straight slits. This means that there will be more noise and therefore the resulting Fourier transform will also be more noisy, making it more difficult to determine the frequencies.

The measurements of the coherence properties, can be very helpful in the design of masks. The current measurements allow to have a very good idea of the coherence property across the whole mask plane. The structures could therefore be optimized locally according to the measured coherence. Knowing the 2D coherence properties is also very helpful, as the 2D structures could be better optimized, as well as the repartition of the structures across the mask, in order to account for the differences in spatial coherence. An important step would be to design such an optimized mask, which takes into account the specificities of the mask-aligner.

Concerning the LED system, it enables fine spatial coherence management. As mentioned already, the versatility of the illumination pattern can therefore be applied to non-conventional printing techniques. The angles can be changed during an exposure, which would lead to completely new possibilities for the realization of prints. This should be first simulated, in order to understand the effect of such changes in the resist. The realization of prints with multiple exposures which have a different illumination pattern is one of the many possibilities offered by the system. Another example is to make “greystone” or “greylevel” lithography. Grey levels can be made by setting different intensity values at different part of the illumination pattern and using a grating mask as done in for the print tests. This is done by Weichelt et al. in the work [11], to fabricate blazed grating, where they scan the illumination pattern and have a very fine resolution of the illumination pattern. Of course, to make these kind of printing even more interesting, the next step would be to have all of the LEDs driven individually.



## Conclusion

The design and fabrication of a prototype of an UV illumination for mask-aligner lithography has been presented. Such a prototype was designed to replace the mercury arc lamp traditionally used for micrometer range lithography. The wavelength required were 365 nm to 450 nm. The challenges faced for the realization of such a prototype were mainly the required power, the homogeneity of the irradiance of the illumination light and the control of the angular distribution of the illumination in the mask plane. The homogeneity of the irradiance in the mask plane needed to be within  $\pm 2.5\%$ , and the irradiance level needed to be of more than  $7 \text{ mW/cm}^2$  at 365 nm. The system required the possibility to modulate the angular distribution in the mask plane. It needed to be compatible with existing machines.

LEDs were chosen to form the source. The homogenization and beam shaping of the light was done with microlense arrays combined with lenses, as with existing mask-aligners. In the chosen solution, 1 W LEDs at 365 nm were placed in an array. The light was collected with parabolic compound concentrators used as reflectors. They were designed to have a square entrance aperture to match the emitting area of the LEDs. The resulting angular distribution after the reflector is also squared, which corresponds to the fly's eye integrator acceptance angle distribution. Those reflectors were challenging to manufacture, as they needed to be 28 mm long for an entrance aperture of  $1.5 \times 1.5 \text{ mm}^2$  and an exit aperture of  $9 \times 9 \text{ mm}^2$ . The solution found to build them was to manufacture them into smaller pieces. A reflector is formed by mounting four identical pieces together. Those parts were machined in aluminum and the reflective surfaces were polished. The maximum theoretical efficiency for the reflectors, with a reflectivity of 78 %, is 64 %.

Different prototypes were fabricated. First a 2x2 LEDs prototype was built, which was used to do the optical characterization. The intensity measurement showed that, after the reflectors, most of the light is within  $\pm 10^\circ$  which corresponds to the acceptance angle of the fly's eye integrator. After the fly's eye integrator, the intensity was measured to be within  $\pm 5\%$  over an angular extent of  $\pm 9^\circ$ . A larger prototype of 7x7 LEDs was then fabricated. This prototype includes a heatsink and an elaborate electronics. The LEDs were divided into four groups which could be driven independently. The achieved irradiance level in the mask plane is  $31 \text{ mW/cm}^2$  at 365 nm, which is much superior to a 350 W mercury lamp and corresponds to the level of irradiance achieved by a 1 kW lamp. The measured homogeneity of the irradiance in the mask plane is below  $\pm 2\%$  for all the different groups and goes as low as  $\pm 1.2\%$  when

## Conclusion

---

all the LEDs are switched on. These uniformity levels are superior to those achieved with the mercury arc lamp illumination system. The angular distribution in the mask plane was measured. It is quite different with the LED-base system than with the mercury arc lamp. This did not seem to impact the resolution of the prints, but would need more investigation. Prints were made which show a resolution of  $3.5\ \mu\text{m}$  at a proximity gap of  $30\ \mu\text{m}$ .

In the second part of the thesis, the measurement of the spatial coherence was investigated. The link between the spatial coherence length and the angular distribution was established by using the contrast measurement of interference patterns produced by double and multiple slits of  $1\ \mu\text{m}$ . A test setup was used, which allows to measure the spatial coherence length as a function of the angular distribution of the incident angle. The results show a very good agreement with the simulation and the analytical curve. Measurements of the spatial coherence were done in a mask-aligner. The degree of spatial coherence is homogeneous over the mask plane within  $\pm 1.2\ \%$ . A method for measuring the 2D spatial coherence was developed. It consists in measuring the interference pattern produced by circular slits. This allows to have a visual information about the local degree of spatial coherence in all the directions of a plane.

To conclude, the developed LED-base illumination system for mask-aligner is almost readily implementable in commercial mask-aligners. This system demonstrated very good performance and is a more compact, efficient and sustainable solution. The measurement of the degree of spatial coherence brings new information about the light in the mask plane. This can be used to develop in a more efficient way the advanced techniques in mask-aligner lithography.



# Bibliography

- [1] J. R. Sheats and B. W. Smith, eds., *Microolithography: science and technology*. New York: Marcel Dekker, 1998.
- [2] “SUSS MicroTec AG mask-aligner datasheet.” <https://www.suss.com/en/products-solutions/mask-aligner>. Accessed: 2017-12-15.
- [3] R. Winston, W. T. Welford, J. C. Miñano, and P. Benítez, *Nonimaging optics*. Amsterdam ; Boston, Mass: Elsevier Academic Press, 2005.
- [4] A. Arecchi, T. Messadi, and R. J. Koschel, *Field Guide to Illumination*. 1000 20th Street, Bellingham, WA 98227-0010 USA: SPIE, Aug. 2007.
- [5] M. Karlen and J. Benya, “Lighting Design Basics,” p. 203.
- [6] O. Dross, R. Mohedano, M. Hernández, A. Cvetkovic, J. C. Miñano, and P. Benítez, “Koehler integrators embedded into illumination optics add functionality,” pp. 71030G–71030G–12, Sept. 2008.
- [7] P. Schreiber, S. Kudaev, P. Dannberg, and U. D. Zeitner, “Homogeneous LED-illumination using microlens arrays,” in *Proc. SPIE*, vol. 5942, pp. 188–196, 2005.
- [8] R. Voelkel, U. Vogler, A. Bich, P. Pernet, K. J. Weible, M. Hornung, R. Zoberbier, E. Cullmann, L. Stuerzebecher, T. Harzendorf, and others, “Advanced mask aligner lithography: new illumination system,” *Optics express*, vol. 18, no. 20, pp. 20968–20978, 2010.
- [9] R. Voelkel and K. J. Weible, “Laser beam homogenizing: limitations and constraints,” in *Optical Systems Design*, pp. 71020J–71020J, International Society for Optics and Photonics, 2008.
- [10] L. Erdmann, M. Burkhardt, and R. Brunner, “Coherence management for microlens laser beam homogenizers,” in *International Symposium on Optical Science and Technology*, pp. 145–154, International Society for Optics and Photonics, 2002.
- [11] T. Weichelt, Y. Bourgin, and U. D. Zeitner, “Mask aligner lithography using laser illumination for versatile pattern generation,” *Optics Express*, vol. 25, p. 20983, Sept. 2017.

## Bibliography

---

- [12] R. Kirner, A. Vetter, D. Opalevs, C. Gilfert, M. Scholz, P. Leisching, T. Scharf, W. Noell, C. Rockstuhl, and R. Voelkel, "Mask-aligner lithography using a continuous-wave diode laser frequency-quadrupled to 193 nm," *Optics Express*, vol. 26, p. 730, Jan. 2018.
- [13] R. S. West, "Side-emitting high-power LEDs and their application in illumination," p. 171, Nov. 2002.
- [14] F. Fournier and J. Rolland, "Optimization of freeform lightpipes for light-emitting-diode projectors," *Applied optics*, vol. 47, no. 7, pp. 957–966, 2008.
- [15] B. Van Giel, "Using a fly's eye integrator in efficient illumination engines with multiple light-emitting diode light sources," *Optical Engineering*, vol. 46, p. 043001, Apr. 2007.
- [16] M. Erickstad, E. Gutierrez, and A. Groisman, "A low-cost low-maintenance ultraviolet lithography light source based on light-emitting diodes," *Lab Chip*, vol. 15, no. 1, pp. 57–61, 2015.
- [17] F. Y. Ciou, Y. C. Chen, C. T. Pan, P. H. Lin, P. H. Lin, and F. T. Hsu, "Investigation of uniformity field generated from freeform lens with UV LED exposure system," p. 93830S, Mar. 2015.
- [18] B. Van Giel, Y. Meuret, and H. Thienpont, "Design of axisymmetrical tailored concentrators for LED light source applications," in *Photonics Europe*, pp. 619603–619603, International Society for Optics and Photonics, 2006.
- [19] H. J. Cornelissen, H. Ma, C. Ho, M. Li, and C. Mu, "Compact collimators for high-brightness blue LEDs using dielectric multilayers," p. 81230J, Sept. 2011.
- [20] M. E. Testorf, B. M. Hennelly, and J. Ojeda-Castañeda, *Phase-space optics: fundamentals and applications*. New York: McGraw-Hill, 2010. OCLC: 471487453.
- [21] M. Zhong and H. Gross, "Phase space of partially coherent light with discontinuous surfaces," *Journal of the European Optical Society-Rapid Publications*, vol. 12, Dec. 2016.
- [22] L. Waller, G. Situ, and J. W. Fleischer, "Phase-space measurement and coherence synthesis of optical beams," *Nature Photonics*, vol. 6, pp. 474–479, July 2012.
- [23] D. Rausch and A. Herkommer, "Phase space imaging in optical design," p. 919305, Sept. 2014.
- [24] D. Rausch and A. M. Herkommer, "Phase space approach to the use of integrator rods and optical arrays in illumination systems," *Advanced Optical Technologies*, vol. 1, Jan. 2012.
- [25] D. K. Patel, P. K. Brahmabhatt, and H. Panchal, "A review on compound parabolic solar concentrator for sustainable development," *International Journal of Ambient Energy*, vol. 39, pp. 533–546, July 2018.

- 
- [26] J. M. Gordon, P. Kashin, and A. Rabl, "Nonimaging reflectors for efficient uniform illumination," *Applied optics*, vol. 31, no. 28, pp. 6027–6035, 1992.
- [27] P. G. Szabó, T. Csendes, L. G. Casado, and I. García, *Packing Equal Circles in a Square I. -Problem Setting and Bounds for Optimal Solutions*. Boston: Kluwer Academic Publishers, 2000.
- [28] Association suisse de normalisation and Société suisse des constructeurs de machines, *Extrait de normes pour écoles et professions de la mécanique*. Zurich: VSM, 2006. OCLC: 634854753.
- [29] P. Engineering, "FRED optical engineering software (version 15.90)." <https://photonengr.com/fred-software/>, 2017.
- [30] nichia corporation, "nichia corporation specifications for UV LED, NVSU233A(T)." <http://www.nichia.co.jp/fr/product/uvled.html>, 2016.
- [31] C. Mack, *Fundamental Principles of Optical Lithography*. Chichester, UK: John Wiley & Sons, Ltd, Nov. 2007.
- [32] A. K.-K. Wong, *Resolution enhancement techniques in optical lithography*. No. v. TT 47 in Tutorial texts in optical engineering, Bellingham, Wash: SPIE Press, 2001.
- [33] S. Asai, I. Hanyu, and K. Hikosaka, "Improving projection lithography image illumination by using sources far from the optical axis," *Journal of Vacuum Science & Technology B: Microelectronics and Nanometer Structures*, vol. 9, p. 2788, Nov. 1991.
- [34] B. E. A. Saleh and M. C. Teich, *Fundamentals of photonics*. New York: Wiley, 1991.
- [35] D. Mendlovic, G. Shabtay, A. W. Lohmann, and N. Konforti, "Display of spatial coherence," *Optics Letters*, vol. 23, p. 1084, July 1998.
- [36] F. Zernike, "The concept of degree of coherence and its application to optical problems," *Physica*, vol. 5, pp. 785–795, Aug. 1938.
- [37] B. J. Thompson and E. Wolf, "Two-beam interference with partially coherent light," *JOSA*, vol. 47, no. 10, p. 895, 1957.
- [38] Y. Mejía and A. I. González, "Measuring spatial coherence by using a mask with multiple apertures," *Optics Communications*, vol. 273, pp. 428–434, May 2007.
- [39] A. Smith and C. Dainty, "Numerical modeling of spatial coherence using the elementary function method," *Applied Optics*, vol. 52, p. 2815, Apr. 2013.
- [40] S. Divitt, Z. J. Lapin, and L. Novotny, "Measuring coherence functions using non-parallel double slits," *Optics Express*, vol. 22, p. 8277, Apr. 2014.
- [41] S. Divitt and L. Novotny, "Spatial coherence of sunlight and its implications for light management in photovoltaics," *Optica*, vol. 2, p. 95, Feb. 2015.

## Bibliography

---

- [42] M. J. E. Golay, "Point Arrays Having Compact, Nonredundant Autocorrelations," *Journal of the Optical Society of America*, vol. 61, p. 272, Feb. 1971.
- [43] D. G. Voelz, *Computational fourier optics: a MATLAB tutorial*. Bellingham, Wash: SPIE Press, 2011.
- [44] R. H. Brown, "Measurement of stellar diameters," *Annual Review of Astronomy and Astrophysics*, vol. 6, no. 1, pp. 13–38, 1968.
- [45] E. Wolf and W. H. Carter, "Angular distribution of radiant intensity from sources of different degrees of spatial coherence," *Optics Communications*, vol. 13, pp. 205–209, Mar. 1975.
- [46] K. Saastamoinen, J. Tervo, J. Turunen, P. Vahimaa, and A. T. Friberg, "Spatial coherence measurement of polychromatic light with modified Young's interferometer," *Optics Express*, vol. 21, p. 4061, Feb. 2013.
- [47] C. K. Hitzengerger, M. Danner, W. Drexler, and A. F. Fercher, "Measurement of the spatial coherence of superluminescent diodes," *Journal of Modern Optics*, vol. 46, pp. 1763–1774, Oct. 1999.
- [48] L. Stuerzebecher, T. Harzendorf, U. Vogler, U. D. Zeitner, and R. Voelkel, "Advanced mask aligner lithography: fabrication of periodic patterns using pinhole array mask and Talbot effect," *Optics express*, vol. 18, no. 19, pp. 19485–19494, 2010.
- [49] T. Harzendorf, L. Stuerzebecher, U. Vogler, U. D. Zeitner, and R. Voelkel, "Half-tone proximity lithography," p. 77160Y, Apr. 2010.

## Johana Bernasconi

### EPFL Master of Science MSc in Microengineering

Chemin de la Marnière 53  
2068 Hauterive  
+41 79 579 20 02  
[johana.bernasconi@epfl.ch](mailto:johana.bernasconi@epfl.ch)

08.02.1991  
Civil state: single  
Citizenship: Swiss



Engineer in microtechnology, specialized in optics, I am able to tackle complex problems of engineering which require skills from different domains. I can communicate professionally in French, English and German.

#### Professional experience

---

- 09.2014 – 09.2018 Phd at **EPFL** (Swiss Federal Institute of Technology) Neuchâtel and Lausanne, Switzerland, in collaboration with **Süss Microoptics SA**, Hauterive, Switzerland and laboratory course assistant teaching at **EPFL**.
- 05.2014 – 07.2014 Substitute teacher at secondary school **EOREN**, Peseux, Switzerland in French, English, German, Mathematics.
- 09.2013 – 08.2014 Internship and Master Project at **Carl Zeiss AG, Corporate Research and Technology**, Jena, Germany.
- 09.2012 – 01.2013 **EPFL**: Assistant teaching in Analysis III.

#### Education

---

- 09.2014 – 09.2018 **PhD in Optics and Photonics at EPFL** (Swiss Federal Institute of Technology) Neuchâtel and Lausanne, Switzerland.
- 09.2012 – 04.2014 **Master of Science in Microengineering**, majoring in optics at **EPFL** (Swiss Federal Institute of Technology), Lausanne, Switzerland.
- 09.2009 – 07.2012 **Bachelor of Science in Microengineering**, at **EPFL** (Swiss Federal Institute of Technology), Lausanne, Switzerland.
- 08.2011 **Training course in mechanical manufacturing at ETML** (École des Métiers de Lausanne), Lausanne, Switzerland.
- 08.2006 – 07.2009 **Maturité Fédérale** in Physics and Applied Mathematics, bilingual French-English at **Lycée Denis-de-Rougemont**, Neuchâtel, Switzerland.

#### Projects

---

- **PhD thesis:** *High power ultraviolet LED illumination systems: coherence properties and applications in photolithography*, Laboratory of Optics and Photonics Technology, EPFL, and SUSS MicroOptics, Switzerland. Design of a new LED-based illumination system for lithography machines. Research on multi-channel illuminations and their spatial coherence properties.
- **Master project:** *System Simulation and Adjustment concept of Confocal Imaging Systems*, Carl Zeiss AG, Corporate Research and Technology, Jena, Germany. Use of Matlab and of an optical design software to simulate confocal imaging systems; adjustment of such a system in the laboratory.

#### Skills

---

- **Practical experience:** Optical setups adjustment, clean room work, microscopy, mobile robot programming, teaching.
- **Computer science:** Matlab, Optical system design softwares (FRED), Labview, C language, Latex, Microsoft Office, Java (image processing), Assembler programming.
- **Languages:**
  - French (native)
  - German (B2 self-appreciation), 09.2013 – 08.2014: Master project in Jena, Germany.
  - English (C1 self-appreciation), 08.2007-10.2007: Language exchange in Ontario, Canada.

#### Interests

---

- Skiing including ski teacher in two student camps, running, climbing.
- Playing the flute including 7 years at the Music Academy of Neuchâtel.
- Reading (in French, English and German).

## **Papers**

---

J. Bernasconi; T. Scharf; U. Vogler; H. P. Herzig: **High-power modular LED-based illumination systems for mask-aligner lithography**; *Optics Express*. 2018-04-19. DOI: 10.1364/OE.26.011503.

J. Bernasconi; T. Scharf; H. P. Herzig: **Measurement of the spatial degree of coherence of extended light sources**; [to be submitted].

## **Conference proceedings**

---

J. Bernasconi; T. Scharf; M. Groccia; R. Kirner; W. Noell; H. P. Herzig; U. Vogler: **High power modular LED-based illumination system for lithography applications**. Nonimaging Optics: Efficient Design for Illumination and Solar Concentration XV, San Diego, CA, AUG 19-23, 2018.

J. Bernasconi; T. Scharf; H. P. Herzig; R. Voelkel; A. Bramati : **Coherence management in lithography printing systems**. 2016. Conference on Optical Microlithography XXIX, San Jose, CA, FEB 23-25, 2016. p. UNSP 978016. DOI: 10.1117/12.2219115

T. Scharf; M.-S. Kim; K. Puthankovilakam; J. Bernasconi; H. P. Herzig et al.: **Structured amplitude and phase fields behind microstructures: The quest for high contrast modulation at proximity**. 2016. 10th Conference on Complex Light and Optical Forces, San Francisco, CA, FEB 16-18, 2016. p. UNSP 97640B. DOI: 10.1117/12.2214341.

## **Conference talks**

---

J. Bernasconi; T. Scharf; H. P. Herzig; U. Vogler; R. Kirner: **High quality modular LEDs-based UV lithography illumination**. 2nd EOS Conference on Light Engineering, Munich, GE, JUNE 26-29, 2017.

J. Bernasconi; T. Scharf; M. Groccia; R. Kirner; W. Noell; H. P. Herzig; U. Vogler: **High power modular LED-based illumination system for lithography applications**. Nonimaging Optics: Efficient Design for Illumination and Solar Concentration XV, San Diego, CA, AUG 19-23, 2018.

## **Conference poster**

---

J. Bernasconi; T. Scharf; H. P. Herzig; R. Voelkel; A. Bramati : **Coherence management in lithography printing systems**. 2016. Conference on Optical Microlithography XXIX, San Jose, CA, FEB 23-25, 2016. p. UNSP 978016. DOI: 10.1117/12.2219115

